Titre: Title:	Beam Scanning Slot Array Antennas with Electromechanical Reconfigurability
Auteur: Author:	Amirhossein Ghasemi
Date:	2018
Type:	Mémoire ou thèse / Dissertation or Thesis
Référence: Citation:	Ghasemi, A. (2018). Beam Scanning Slot Array Antennas with Electromechanical Reconfigurability [Thèse de doctorat, École Polytechnique de Montréal]. PolyPublie. https://publications.polymtl.ca/3730/

URL de PolyPublie: PolyPublie URL:	https://publications.polymtl.ca/3730/
Directeurs de recherche: Advisors:	Jean-Jacques Laurin
Programme: Program:	génie électrique

UNIVERSITÉ DE MONTRÉAL

BEAM SCANNING SLOT ARRAY ANTENNAS WITH ELECTROMECHANICAL RECONFIGURABILITY

AMIRHOSSEIN GHASEMI
DÉPARTEMENT DE GÉNIE ÉLECTRIQUE
ÉCOLE POLYTECHNIQUE DE MONTRÉAL

THÈSE PRÉSENTÉE EN VUE DE L'OBTENTION
DU DIPLÔME DE PHILOSOPHIE DOCTOR
(GÉNIE ÉLECTRIQUE)
DÉCEMBRE 2018

UNIVERSITÉ DE MONTRÉAL

ÉCOLE POLYTECHNIQUE DE MONTRÉAL

Cette thèse intitulée :

BEAM SCANNING SLOT ARRAY ANTENNAS WITH ELECTROMECHANICAL RECONFIGURABILITY

présenté par : GHASEMI Amirhossein

en vue de l'obtention du diplôme de : Philosophiae Doctor

a été dûment acceptée par le jury d'examen constitué de :

M. NERGUIZIAN Chahé, Ph. D., président

M. LAURIN Jean-Jacques, Ph. D., membre et directeur de recherche

M. WU Ke, Doctorat, membre

Mme POPOVIC Milica, Ph. D., membre externe

DEDICATION

To my wife, Mehrnoush

To my son, Arsham

…To Freedom

ACKNOWLEDGEMENTS

Firstly, I would like to express my sincere gratitude to my advisor, Prof. Jean-Jacques Laurin for the continuous support of my Ph. D. study and related research, for his patience, motivation, and immense knowledge. His guidance helped me in all the time of research and writing of this thesis. I could not have imagined having a better advisor and mentor for my Ph.D. study. As my teacher and mentor, he has thought me more than I could ever give him credit for here. He has shown me, by his example, what a good scientist (and person) should be.

Besides my advisor, I would like to thank the rest of my thesis committee: Prof. Chahé Nerguizian, Prof. Ke Wu, and Dr. Milica Popovic, for their insightful comments and encouragement, but also for the hard questions which incented me to widen my research from various perspectives.

My sincere thanks also goes to Mr. Jules Gautier, Mr. Jean-Sebastien Décarire, Mr. Steve Dubé, Mr. Traian Antonescu and Mr. Maxime Thibaut who provided me an opportunity to access to the laboratory and research facilities of Poly-Grames. Without they precious support it would not be possible to conduct this research.

I thank my fellow labmates; Ahmad, Leandro, Marzieh, Mahbubeh, Lamine, Ramin, David, Sophie for the stimulating discussions, for never hesitating to have a coffee with me when I needed to be comforted, and for all the fun we have had in the last four years.

Nobody has been more important to me in the pursuit of this project than the members of my family. I would like to thank my mother, Maman Fakhri, my father, Baba Rahim, my sister, Elham, and my brother, Ehsan whose love and guidance are with me in whatever I pursue. They are the ultimate role models. Most importantly, I wish to thank my lovely wife and son, Mehrnoush and Arsham, who provide unending inspiration.

I will end up with a special thought towards the persons without whom all this would not have been possible. The person who taught me antennas for the first time and for enlightening me the first glance of research, Dr. Alireza Mallahzadeh in Iran at Shahed University and my cousin Dr. Rasta Ghasemi for the continuous support of my master study in France, University of Paris-XI and also for providing insightful help to immigrate to Canada in general.

RÉSUMÉ

La possibilité de reconfigurer facilement les petites pièces des antennes réseau pour balayer le faisceau principal joue un rôle essentiel dans plusieurs applications, notamment les communications par satellite et les radars. Ces antennes reconfigurables ont des exigences particulières en matière de capacité de balayage de faisceau, de faible poids/taille, de capacité de puissance élevée, de gain élevé, de niveau de lobes secondaires faibles, de vitesse de poursuite élevée, de coût faible et de profil bas. Trouver une solution capable d'intégrer toutes ces caractéristiques est un défi et nécessite l'introduction de solutions innovantes.

L'objectif principal de cette thèse est d'évaluer la capacité de balayage continu de faisceau de haute puissance dans deux polarisations linéaires différentes avec reconfigurabilité électromécanique. Pour réussir cela, nous prenons en compte la rotation électromécanique d'une ou deux tiges diélectriques à l'intérieur d'un guide d'onde à fentes.

La première approche est basée sur un guide d’onde rectangulaire à fentes à large paroi. Nous utilisons un guide d’onde rectangulaire WR-62 standard. Le réseau linéaire à 20 fentes proposé permet le balayage du faisceau en faisant tourner deux tiges diélectriques à l'intérieur du guide d'ondes. Des tiges faites de diélectrique ont été choisies pour éliminer le mode TEM. La longueur d’onde de l’onde progressive et par conséquent les phases des éléments sont modifiées en fonction de l’angle de rotation des tiges par rapport au champ de mode dominant.

Une étude détaillée du couplage mutuel entre les fentes et de la méthodologie de conception du réseau de fentes est menée. Les longueurs des fentes et leurs décalages par rapport au plan central du guide d'ondes doivent être évalués, de manière à obtenir un motif spécifié et un niveau d'impédance d'entrée spécifié. Pour réussir cela, nous devons prendre en compte le couplage mutuel entre les fentes. Une distribution d'amplitude triangulaire superposée à un niveau inférieur constant est utilisée afin de démontrer la capacité de contrôler le niveau des lobes secondaires (SLL).

Une nouvelle conception pour la transition avec un guide d'ondes à rainure utilisant des tiges diélectriques à l'intérieur est proposée. Cette transition se compose d’un guide d’onde coaxial à l’arête et d’un guide d’onde chargé de tiges diélectriques. Les pointes en forme de coin sur l'arête et les plaques diélectriques entraînaient une faible perte de retour (inférieure à 10 dB) pour tous les angles de rotation des tiges.

On observe un balayage du faisceau de 14 ° à la fréquence de référence de 9.35 GHz dans une largeur de bande de 10.5%. Le gain réalisé par l'antenne varie de 18.33 dB à 19.11 dB, ce qui correspond à des efficacités de rayonnement comprises entre 95% et 79%. Le niveau des lobes secondaires est de -14 dB à la fréquence de référence de 9.35 GHz.

Pour améliorer les performances de l'antenne basée sur le guide d'ondes à fentes à large paroi, c'est-à-dire qu'un balayage de faisceau, des résonateurs en forme de I (ISR) sont utilisés sur les tiges. Nous chargeons périodiquement le guide d'ondes avec des ISR afin d'augmenter le retard de phase variable dans le guide d'ondes. Le champ électrique au centre de la paroi la plus large du guide d'ondes devient plus fort lorsque les bandes métalliques des ISR lui sont parallèles. Le déphaseur à guide d'ondes chargé par l'ISR augmente le balayage du faisceau jusqu'à 28 °.

Dans les antennes à guides d'ondes où les fentes sont sur la paroi étroite, l'inclinaison est essentielle pour contrôler l'admittance de la fente. Le composant à polarisation croisée augmente considérablement lorsque le guide d'ondes à fente à paroi étroite balaye l'angle à l'opposé du côté large et produit des interférences. Nous présentons un filtre de polarisation afin de réduire le niveau de polarisation croisée (X-pol) sur une certaine bande de fréquence. Un réseau de 10 fentes inclinées coupée dans la paroi étroite d'un guide d'onde rectangulaire avec un espacement d'élément de $d = 0.64\lambda_0$ fonctionnant en bande Ku est utilisée. Le filtre de polarisation réduit le niveau maximal de polarisation croisée de 10 dB à la fréquence de référence de 14 GHz et de 5 dB sur la bande de fréquences de 12 GHz à 18 GHz.

La deuxième approche étudiée consiste en un guide d'ondes à fentes sur la paroi étroite utilisant une seule tige diélectrique rotative. Un réseau de 20 fentes inclinées fonctionnant en bande X, découpées dans une paroi étroite d'un guide d'onde rectangulaire à rainure est utilisé. La rainure est utilisée pour augmenter la plage de fonctionnement en mode unique à la fréquence de référence de 9.35 GHz. Le balayage du faisceau principal est obtenu en faisant tourner une tige diélectrique à l'intérieur du guide d'ondes à fente étroite. Le changement de longueur d'onde à différents angles de rotation de la tige est utilisé comme déphaseur. Afin d'approuver la commodité de cette méthode, une antenne réseau à guides d'ondes à 20 fentes non résonante avec un espacement des éléments de $d = 0{,}44\lambda0$ a été conçue, construite et mesurée. Il est montré qu'un balayage du faisceau principal de 36 ° peut être observé en faisant tourner la plaque diélectrique de 90 °. Le gain passe de 11.17 dB à 12.17 dB sur la plage de balayage. En raison de la longueur relativement courte du prototype,

les pertes dans la charge finale ont limité l'efficacité du rayonnement à des valeurs comprises entre 43% et 86%. Le niveau des lobes secondaires est d'environ −18 dB à la fréquence de conception. Les diagrammes de rayonnement simulés et mesurés dans le plan E sont en excellent accord à la fréquence de référence de 9.35 GHz.

ABSTRACT

The capability of easily reconfiguring the small parts of array antennas in order to scan the main beam plays a key role in several applications, including satellite communications and radars. These reconfigurable antennas have special demands regarding beam scanning capability, small size/weight, high power handling, high gain, low side lobe level, high tracking speed, low cost, and low profile. Finding a solution able to integrate all these characteristics is challenging, and needs the introduction of innovative solving.

The main goal of this thesis is to evaluate the capability of high power continuous beam scanning in two different linear polarizations with electromechanical reconfigurability. To do this successfully, we account for the electromechanically rotating one or two dielectric slabs inside a slotted waveguide.

The first approach is based on a broad wall slotted rectangular waveguide. We employ a standard WR-62 of rectangular waveguide. The proposed linear 20-slotted array allows beam scanning by rotating of two dielectric slabs inside the waveguide. The slab made of dielectric has been chosen in order to eliminate the TEM mode. The wavelength of the travelling wave and consequently the element's phases are changed depending on the angle of the slabs relative to the dominant mode field.

A detailed investigation of the coupling between the slots and the design methodology of the slot network is conducted. The lengths of the slots and their offsets from the waveguide center plane need to be evaluated, in such a way that a specified pattern and a specified input impedance level are achieved. To do this successfully, we must take into account the mutual coupling between slots. A triangular amplitude distribution superimposed on a constant lower level is used in order to demonstrate the capability to control the side lobe level (SLL).

A novel design for the transition with a ridge waveguide using slabs inside it is proposed. This transition consists of a coaxial to ridge waveguide and a dielectric slabs loaded waveguide. Wedge shaped tips on both the ridge and the dielectric slabs led to good return loss (below -10 dB) for all rotation angles of the slabs.

A 14° beam scanning from near broadside toward end-fire direction at the design frequency of 9.35 GHz in a 10.5% bandwidth is observed. The antenna realized gain varies from 18.33 dB to 19.11

dB which corresponds to the radiation efficiencies between 95% and 79%. The side-lobe level (SLL) is -14 dB at the design frequency of 9.35 GHz.

To improve the broad wall slotted waveguide antenna performance, i.e. beam scanning, I-shaped resonators (ISRs) are used on the slabs. We periodically load the waveguide with ISRs in order to increase the varying phase delay in the waveguide. The electric field in the center of the wider wall of the waveguide becomes stronger when the metallic strips of ISRs are parallel to it. The ISR-loaded waveguide phase shifter increases the beam scanning up to 28°.

In narrow wall slotted waveguides, inclined slot which is essential to control the slot admittance, is directly related to the radiated power. Cross-polarized component increases greatly as the narrow wall slotted waveguide scanned at an angle away from broadside and produces interference. We present a polarization filter in order to reduce cross polarization (X-pol) level over the frequency band. A 10 inclined slot array cut in the narrow wall of a rectangular waveguide with the element spacing of $d = 0.64\lambda_0$ operating in Ku-band is employed. The polarization filter reduces the maximum cross-polarization level by 10 dB at the design frequency of 14 GHz and 5 dB over the frequency band 12 GHz to 18 GHz.

The second approach is a narrow wall slotted waveguide using a dielectric rotating slab. An array of 20-inclined slots operating in X-band, cut in a narrow wall of a rectangular ridge waveguide is employed. The ridge is using to increase the range of single mode operation at the design frequency of 9.35 GHz. Beam steering is achieved by rotating a dielectric slab inside the slotted narrow wall waveguide. The change of wavelength at different rotation angles of the slab is used as the phase shifter. In order to approve the convenience of this method, a non-resonant 20-slot waveguide array antenna with an element spacing of $d = 0.44\lambda_0$ has been designed, built and measured. It is shown that a main beam scanning of 36° can be observed from near broadside toward end-fire by rotating the dielectric slab by 90^o. The gain changes from 11.17 dB to 12.17 dB over the scanning range. As a result of the relatively short length of the prototype, losses in the terminating load have limited the radiation efficiency to values between 43% and 86%. The side-lobe level (SLL) is -18 dB at the design frequency. The simulated and measured E-plane radiation patterns compared very well at the design frequency of 9.35 GHz.

TABLE OF CONTENTS

LIST OF TABLES

LIST OF FIGURES

LIST OF SYMBOLS AND ABBREVIATIONS

CRLH	Composite right/left handed
FSA	Frequency scanning array
GSO	Geostationary orbit
ISR	I-Shaped resonator
LEO	Low earth orbit
LWA	Leaky wave antenna
MEMS	Microelectromechanical system
MIMO	Multiple input multiple output
NGSO	Non-geostationary orbit
PPW	Parallel plate waveguide
RFIC	Radio frequency integrated circuit
RWG	Rectangular waveguide
SLL	Side lobe level
TEM	Transverse electromagnetic
X-pol	Cross polarization

LIST OF APPENDICES

CHAPTER 1 INTRODUCTION

1.1 Beam scanning antenna applications

Increased performance needs established on earth observation satellites in low earth orbit (LEO) require large data rates to be downloaded to the ground station [1]. The antennas currently used for this task have single fixed beams, which completely cover all of the visible surface of the earth. The gain of this fixed beam is formed to commit for the distance from the satellite to the ground station. The wide beamwidth needed by this approach can be achieved with a low-gain antenna and a high transmitter power would be required to support high data rates [1].

The reconfiguration feature referred to this thesis is to achieve a diversity of low cost and high power continuous beam scanning. Therefore, this approach would be an adequate candidate to be used in a ground station which can receive data from a passing LEO satellite. The antenna can track LEO satellites with a wide beamwidth (e.g. fan beam) using reconfigurable elements. High-rate data transfer from a LEO satellite to a ground station is achievable if fast steerable antennas are utilized [2].

"Differently from geostationary orbit (GSO) terminals, non-geostationary orbit (NGSO) users will need to track the satellites in their relative motion, and perform satellite handover with very high rates, possibly ones per minute, without interrupting the data flow. If this was not enough, there is the enormous challenge of accomplish this at a very low cost – some operator requiring it to be as low as 100 US dollars. Antennas are the key enablers to meet such requirements. [3]"

Another application of the concept described in this thesis is weather radar. Radar systems are used by meteorologists all over the world for collecting the information needed for making weather forecasts. The accuracy of weather forecasts thus depends strongly on the efficacy of the radar system that is used by these scientists. The radars that are currently used in Canada cover vast regions. Due to this large-area radar coverage, the precision of these forecasts diminishes because the latter reduces with the distance. Moreover, the mechanical scanning radar is not fast enough for assimilating the data and hence it does not provide any control over some specific regions to study.

The Canadian meteorological radar network consists of 31 weather radars stretching over Canada's most populated regions (see Figure1.1) [4]. Their primary purpose is the early detection of snow or rainfall, its action and the threat it poses to life and property. Weather radars allow to locate precipitation and measure the intensity in real time as shown in Figure 1.2. Each has a range of 256 km in radius around the site to observe reflectivity, and a range of 128 km to distinguish velocity patterns [4].

Currently, very large radars are used for the assimilation and study of meteorological data. These radars collect data over vast areas. However, radar accuracy decreases with distance; also large radars are complex to achieve and they are excessively expensive. Due to the fact that radar scanning is done mechanically, large radars are also slow in data assimilation. Furthermore, bearing in mind that the radar with mechanical scan captures regions information in a pre-defined order (following a circle or a sphere), it is not possible to randomly verify the processed regions information. Thus, if a given region has information of greater interest, it is necessary to wait for the scan to complete before being able to reprocess or verify the information of this region [5].

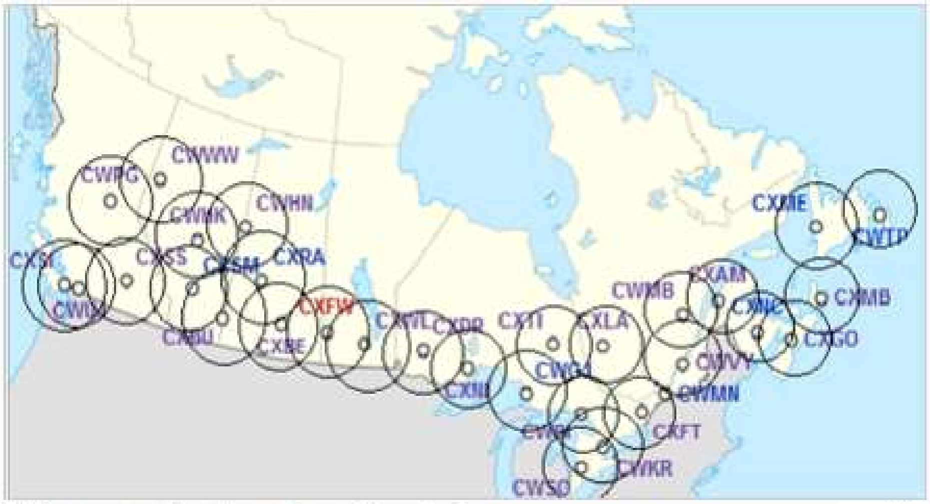

Canadian Meteorological Radar Network

Figure 1.1: Canadian meteorological radar network [4].

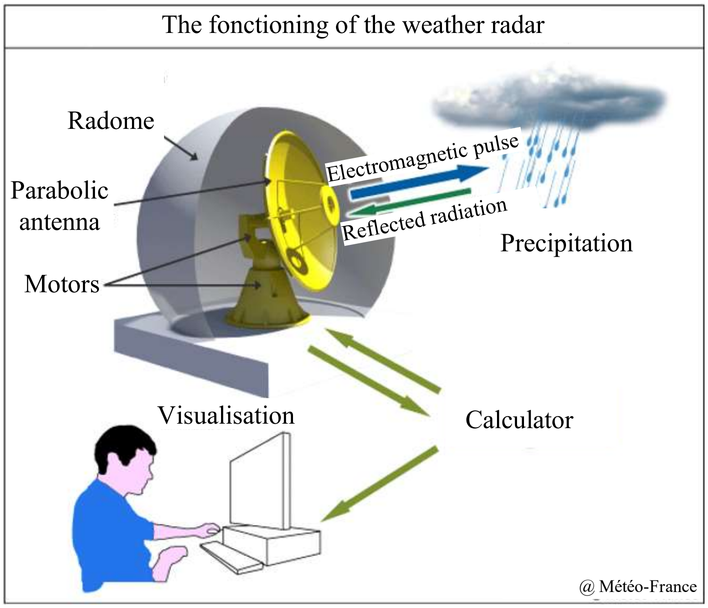

Figure 1.2: The functionning of the weather radar (Retrieved from http//www.meteofrance.fr).

1.2 Objectives

Beam scanning has emerged as one of the major challenges in antenna design for satellite communications and radars. While traditional phased arrays are able to produce the large reconfigurable apertures required for high power beam scanning, the cost and bulk associated with feed network of large phased arrays is an important disadvantage.

The aim of this research work is to investigate new possibilities on the design of a faster, more precise and less expensive high power continuous beam scanning antennas. Based on existing designs of beam steering, simpler and less expensive solutions are presented.

By replacing the large antenna with a smaller antenna network, it would be possible to reduce costs and also by distributing the coverage of these small antennas throughout a large area, it could be certainly possible to get better data accuracy.

3-D fields of precipitation can be obtained in the neighbouring of a weather radar by performing a complete azimuthal rotation of the antenna at successively higher elevation angles. This work deals with the elevation angles using electromechanically beam scanning small antennas. A network of these small antennas would be faster and less expensive than the current system.

As the first step, we need to study the different concepts of a beam-scanning antenna array. Next, starting from existing concepts and new technologies of reconfigurable antenna network, we explore the possibility of development of new solutions more optimal in terms of cost and difficulty of realization compared to the current systems.

Finally, we develop and build the prototypes in order to validate the results. However, we do not build full-scale radar for environmental testing due to limitations of the fabrication means available in the laboratory. Nevertheless, the results obtained from the developed prototypes, would be a good evidence of the functionality of the solution.

If the results of this research are satisfactory, this could not be the only significant improvement in the design of beam scanning antennas for the assimilation of meteorological and satellite data; it would result in a new type of antenna that could be used in several other applications such as communication systems, object detection radars, navy radars, etc.

1.3 Contributions

Beam scanning is a primary function of our antenna. We use existing beam-scanning concepts to develop new, simpler and less costly solutions capable of meeting the requirements of a low orbit satellite communication system and meteorological radar that have been listed in the previous section.

Small-scale prototypes of these new solutions can then be built to be tested in an anechoic chamber. Depending on the obtained results and the requirements of the system, the design will be modified and optimized for better results. This process will be repeated as needed as necessary.

Below are the contributions of this dissertation.

- **Developing a continuous beam scanning in broad wall slotted waveguide antenna using rotating dielectric slabs:**
  The design, simulation and measurement of a beam steerable slotted waveguide antenna operating in X band are developed. The proposed beam steerable antenna consists of a standard rectangular waveguide (RWG) section with longitudinal slots in the broad wall. The beam steering in this configuration is achieved by rotating two dielectric slabs inside the waveguide and consequently changing the phase of the slots excitations. We take into account the mutual coupling between the slots such that a specified pattern and a specified

input impedance level are achieved. Furthermore, a matched transition from a coaxial port to the waveguide filled by the rotating slabs and a matched load for the dielectric loaded waveguide used in the antenna are presented.

This design, along with its simulation and measurement results, are described in a manuscript submitted to the IEEE Transactions on Antennas and Propagation. This manuscript is currently under review after some demanded minor corrections.

- **Novel phase varying technique for main beam scanning improvement:**

  A novel waveguide phase shifter is proposed for the designed broad wall slotted array. This phase shifter consists of a standard RWG section loaded with I-shaped resonator (ISR) printed on dielectric slabs. The phase shifting in this configuration is achieved by rotating the dielectric slab with the presence of the ISRs.

- **Cross-polarization (X-pol) reduction of the narrow wall slotted waveguide array:**

  A simple polarization filter compared to existing concepts in order to reduce X-pol of the narrow wall slotted waveguide is presented. The proposed filter consists of a perforated-metallic plate and is significantly capable to reduce X-pol of the antenna. Although this filter is basically designed for a standard WR62 waveguide (without dielectric loading) which works in Ku band, it can be extended to apply in beam scanning narrow wall waveguide which follows in the next section. Bearing in mind that the beam scanning narrow wall waveguide is loaded with dielectric, the operational frequency band will be changed to X band. This filter has been presented in 2018 at IEEE AP-S/URSI 2018, conference in Boston, USA.

- **Beam steering in narrow wall slotted ridge waveguide antenna using a rotating dielectric slab:**

  A beam scanning technique in narrow wall slotted ridge waveguide at X-band is proposed. An array of inclined slots, cut in the narrow wall of a rectangular ridge waveguide is employed. The proposed antenna can provide flexible solution on this regard. This technique benefits only one rotational part (dielectric slab) as the phase shifter which presents less complexity in fabrication compared to broad wall slotted waveguide. A paper based on this technique has been published in 2018 in the IEEE Antennas and Wireless Propagation Letters.

1.4 Dissertation outline

This dissertation presents three iterations of a waveguide-based beam scanning waveguide-fed slot array. Scanning is realized with electromechanically reconfigurable structures inserted in the waveguide. This antenna actuation mechanism is slow compared to electronically reconfigurable devices, but it is less sensitive to temperature variations and can operate with high RF power levels. A comparison between different methods of beam scanning in rectangular waveguide designed for X-band radar frequencies is presented.

Chapter 3 presents the first method which consists of rotating two dielectric slabs inside a broad wall slotted waveguide in order to achieve the element phase shifting in the slots excitations and consequently controlling the main beam direction. In the second method proposed in Chapter IV, we load the same waveguide with two dielectric slabs which I-shaped resonators (ISR) are printed on them in order to improve the range of beam scanning.

A new concept to reduce cross-polarization (X-pol) of narrow wall slotted waveguide is proposed in Chapter 5. The third method of beam scanning is applying a rotating dielectric slab inside a narrow wall slotted waveguide and is presented in Chapter 6. The presented methods show the capability of electromechanical high power beam scanning in two different linear polarizations. General discussion on different methods of this work and the result comparison are presented in Chapter 7. Chapter 8 concludes this dissertation along with the possible future works.

CHAPTER 2 LITERATURE REVIEW

The main idea of this review is the discussion on different techniques of beam scanning. Conventional aperture antennas (reflectors and lenses) are generally used for satellite applications, due to their relative low cost, simplicity of configuration, high efficiency and high gain [6]. Mechanic beam scanning is carried out by reflector movement or deformation using actuators. A complicated feed network, reconfigurable in amplitude and phase has to be used for illuminating the reflector.

Phased arrays are another classic solution to control the main beam position. These arrays have electronic flexibility in feeding elements and allow excellent performance in terms of reconfiguration and high-speed beam scanning. The main disadvantage of electronic phased arrays is low power handling. In addition, in the context of satellite antennas, temperature control on the electronic components is necessary.

The ability of objects to scatter radiation is the basis for the radar applications. Radars act by transmitting high-frequency microwave (mm-cm scale) pulses to the air and measuring the "backscatter" or reflected pulses to the radar. The reflected signal is interpreted to determine where the target is. Typically the radar scans in azimuth as the antenna beam is raised to pre-set elevation angles to provide a three-dimensional look at the air. So the needs of beam scanning for the meteorology radar antenna is evident [7-8]. Beam scanning can be done electronically or electromechanically.

2.1 Mechanical Beam Scanning

Many types of antennas have been designed in the past confessing steering of a narrow beam. In particular, radar sensors for meteorology applications use antennas with agile beams, either by mechanically rotating the complete antenna or electronically steering beam with the fixed antenna [9]. Special attention was paid to concept allowing a fixed antenna and using the mechanical displacement of parts of the antenna. A number of such approaches have been presented in [10-11] as candidates for millimeter wave automotive sensors.

In mechanical antenna beam scanning, nothing changes on the antenna during the scan. The antenna has a fixed main beam position and the position of the antenna is moved mechanically using an automated drive system in order to move the main beam position.

The first example of a mechanically beam scanning antenna was possibly the so-called *Eagle Scanner* [12] of World War II. Phase shifting in a series fed linear array antenna was achieved by mechanical movements of the narrow wall of a rectangular waveguide (Figure 2.1). While it is well understood that by compressing the width of the waveguide the wavelength is changed and thus the phase of the excitation elements vary. The realization of accurate and rapid linear motion of the side wall over the total length of the antenna is not easy to accomplish [13].

2.2 Electronic Beam Scanning

The electronic beam scanning of an antenna consists of changing the direction of the main beam without changing the position of the whole antenna. There are several techniques for performing the electronic beam scanning and it would be quite difficult to present all these techniques here. However, we present phased arrays which are the most popular [14].

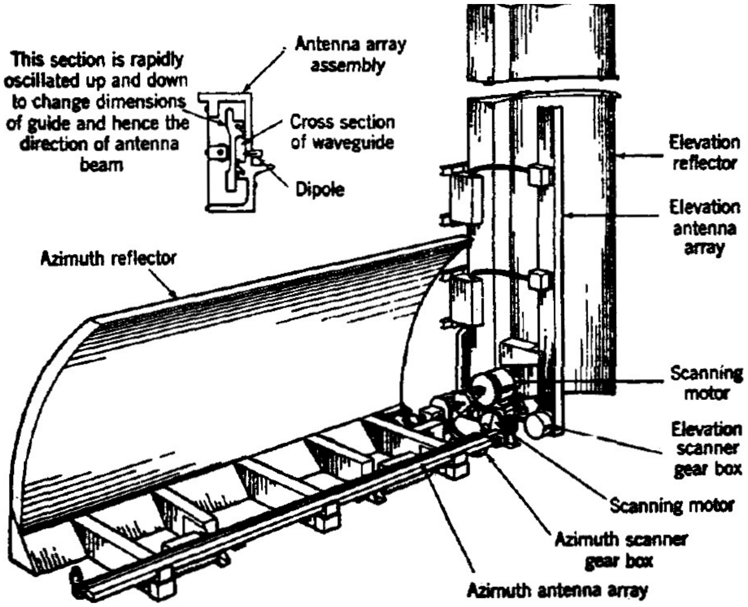

Figure 2.1: Details of Eagle Scanner azimuth and elevation assemblies [12].

2.2.1 Phased Array

Radiating elements each with a phase shifter produce a phased array antenna. Beams are formed by shifting the phase of the signal emitted from each radiating element, in order to provide constructive/destructive intervention as to scan the main beam in any desired direction.

Position of the main beam is possibly controllable in an antenna array. Indeed, the main beam position of the antenna array will change if the phase shift between the elements varies progressively from one element to another [15-17]. This type of network is called phased-array antenna in which the scanning speed of the main beam depends on the electronic speed of variation of the phase between the elements [18-20].

Active components such as PIN diodes [21], microelectromechanical systems (MEMS) [22], ferrites and radio frequency integrated circuit (RFIC) [23] are used in phase shifter arrays in order to perform the beam steering with less complexity. However, implementing the active components is difficult and challenging because of their nonlinear response specially as the power increases.

Phase-array antenna networks have been used for many years in a wide variety applications including wireless communication systems, measurement and biomedical imaging systems, military and meteorology. Analog phase shifter [24-26] with better precision, low cost and low loss, digital one [27] with better speed, ease of manufacture or mixed one [28] can be used in phased array antennas.

Phase shifters can be designed with beam scanning in any arbitrary direction and at a remarkable speed of some microseconds in modern antenna's technology. Researchers in National Severe Storm Laboratory (NSSL) in Oklahama, USA, have designed multi-function radar systems based on phase shifters for meteorological application [29]. The results show that it is possible to achieve complete area coverage of scanning with accurate data in less than 1 minute.

One of the new applications of phased shifter array is massive multiple-input multiple-output (MIMO) for 5G technology [30]. Usually, phased array antennas are expensive and complicated to fabricate in most cases. However, several works have been done recently to reduce these costs [31-32].

Figure 2.2: AN/FPS-117, 3-dimensional air research radar, Lockheed Martin.

Figure 2.2 shows the air-defense radar AN/FPS-117 of Lockheed Martin's family which consists of 1584 radiating elements arranged in an RFIC phase shifter architecture [33].

According to [33] the advantages of the phased array antennas are:

- *high gain with low side lobes*
- *Ability to permit the beam to jump from one target to the next in a few microseconds*
- *Ability to provide an agile beam under computer control*
- *arbitrarily modes of surveillance and tracking*
- *free eligible dwell Time*
- *multifunction operation by emitting several beams simultaneously*

- *Fault of single components reduces the capability and beam sharpness, but the system remains operational*

The disadvantages are:

- *The coverage is limited to a 120° sector in azimuth and elevation;*
- *Deformation of the beam while the deflection;*
- *Low frequency agility;*
- *Very complex structure (phase shifters, processor …);*

- *Still high costs.*

Frequency scanning array (FSA) is a particular type of the phased array where the beam scanning happens by the frequency sweeping of the radiating elements. This antenna is called a frequency scanning array because the beam scanning angle is a function of the transmitted frequency [33]. The typical setup is to feed the different excitation elements from one bend waveguide. By changing the frequency, the angle between the axis of the main beam and the perpendicular on the array antenna varies and as the frequency is changed, the beam axis will change, and therefore steering can be accomplished in elevation [33]. The radar set is designed in order to continue track of the frequencies as they are transmitted and then distinguishes and converts the reflected frequencies into 3D display data [33].

FSA is a more economical and proper solution for a number of applications [34], including radar [35], spectrogram analysis [36], and imaging [37-38]. However, when the antenna array is operated at a fixed frequency or in a narrow band, which is typical for radars, frequency beam scanning cannot be used and instead the whole antenna has to be pivoted mechanically to scan the main beam. This is limiting the maximum scanning speed due to mechanical reasons, as for instance the inertia of the antenna platform itself. In addition, the frequency band needed to steer the main beam over a wide angle can be superior to the narrow bandwidths generally allocated to certain applications such as X-band weather radars [39].

2.2.2 Leaky Wave Antenna (LWA)

Another way to change the phase between the elements in an antenna array without using phase shifters is to mount the antenna on a propagation medium with radiation leakage [40]. This leakage can happen, for example, when there are some discontinuities in the guiding structure, or perhaps when the guide is excited in an unsuitable mode (e.g. TEM) [41]. In terms of LWA design, this energy leakage could be advantageous and used [41]. Slotted waveguides [42-43], higher order mode microstrip [44-47], and Composite Right/Left-Handed structures (CRLH) [48] belong to this family [49].

The following equation [50] gives the position of the beam angle as a function of frequency:

$$\sin\theta = \frac{\beta}{k_0} \tag{2.1}$$

where k_0 and β are respectively the free-space wave number in air and in the LWA. We note that for a real value of θ it is necessary to have $|\beta| < k_0$ [50]. Thus, the propagation mode contributing to the radiation must have a phase velocity greater than c, the speed of light in vacuum. Moreover, to have the greatest variation of θ over a given frequency range, $\frac{d\beta}{d\omega}$ must be maximized [40]. This clarifies to have a mode with the small group speed.

LWA apply to the more common class of traveling wave antenna, which use a traveling wave on a guiding structure as the main radiating device [51]. Traveling-wave antennas have two general classifications, slow-wave antennas and fast-wave antennas, which are usually specified to as leaky-wave antennas [52].

A uniform structure LWA (Figure 2.3) has a cross section that is uniform (constant) along the length of the structure, usually in the form of a waveguide which has been partially opened to permit radiation to happen [40]. The guided wave on the uniform structure is a fast wave ($\beta < k_0$), and thus radiates as it propagates. Furthermore, the uniform LWA could have a suitable taper along its length in order to improve and enhance the sidelobe levels [40].

A periodic LWA structure (Figure 2.4) consists of a uniform structure which supports a slow (non-radiating) wave that has been periodically modulated in some forms [40]. The periodic modulation itself is uniform along the structure's length, again except for the small taper of the periodic properties along the length to control the side-lobes [41]. For the reason that a slow wave ($\beta > k_0$) radiates at discontinuities, the periodic modulations (discontinuities) make the wave to radiate frequently along the length of the structure [41]. From a more complicated viewpoint, the periodic

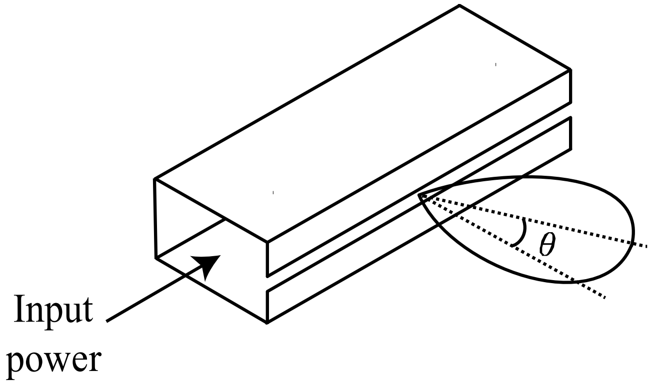

Figure 2.3: Waveguide with a full-depth slot representing a continuous LWA [40].

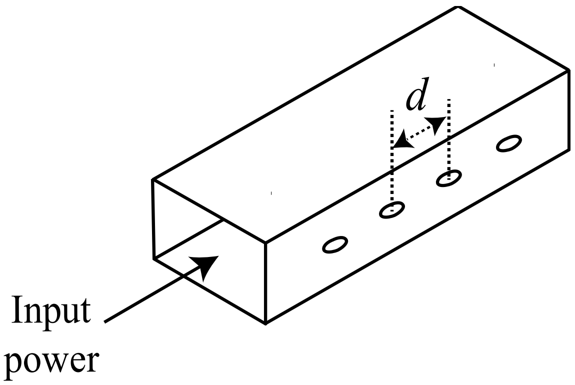

Figure 2.4: Slotted rectangular waveguide representing a periodic LWA [40].

modulation forms a guided wave that is composed of an infinite number of space harmonics (Floquet modes) [20]. Although the main ($n = 0$) space harmonic is a slow wave, one of the space harmonics (usually the $n = -1$) is planned to be a fast wave, and this harmonic wave is the radiating wave [40].

The wave number of n$^{\text{th}}$ Floquet mode is given by

$$\beta_n = k_0 + \frac{2n\pi}{d}, \qquad -\infty < \text{n} < \infty \tag{2.2}$$

where d is the periodicity [50]. The phase constant β_n can clearly consider a notable number of values, but if at least one of the space harmonics becomes fast, the whole mode will become leaky [41].

Since $k_0 = 2\pi/\lambda_0$, it is clear that $|\beta_n| < k_0$, provided that λ_0/d is appropriately selected and the harmonic number n is negative [41]. For an antenna which is designed to have only one radiated beam, we can choose $n = -1$ [41]. The antenna will not radiate any beams at low frequencies because of fast harmonics. A beam arises from backward end-fire by increasing the frequency at $n = -1$(fast harmonics). As the frequency increases more, the beam will steer from backward up to forward end-fire through broadside [41].

Figure 2.5 shows the dispersion diagram of LWAs including the radiation zone. In most cases the harmonic of $n = -1$ is used for radiation because this harmonic is often located in the radiation zone of the network ($-k_0 < \beta_{-1} < k_0$) [40].

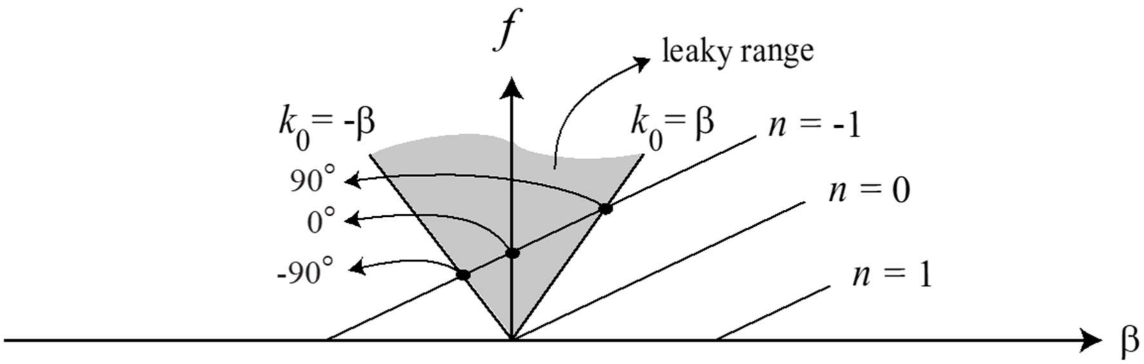

Figure 2.5: Dispersion diagram of LWAs representing the leaky range and the harmonics[40].

LWAs are theoretically able to scan the beam in a range of −90º to 90º [40]. However, scanning in the range of −90º, 0º and 90º is very difficult and similar to FSAs, the frequency range required for scanning becomes very large, and unrealistic for an application.

Over the last few years, LWAs have been intensively improved especially with structures with negative refractive index (CRLH) [53-54]. CRLHs are capable to perform an almost perfect beam scan in the whole range from -90º to 90º [55]. However, depending to the technology used, CRLHs are not suitable for high power applications such as weather radar. This would be possible with metallic waveguides and not with the printed structures.

2.2.3 Circular Configuration Antenna Array

Different linear configurations for beam scanning antenna arrays have been discussed previously. However, the scan range of these linear arrays is not more than 180º. For example, the meteorological application requires the beam scanning in the whole azimuth plane (360º) [56]. In this case, circular configuration array can be an appropriate candidate. Circular configuration arrays for fast electronic beam steering and their advantage over planar phased arrays for the weather broadcasting were studied in [57-58].

Recently, a network of detectors consisting of hundreds of small radars has been designed [56] to assimilate the weather data perfectly [59-60]. Many circular configuration arrays forming radar call for economical and agile antenna system designs and several researchers have worked to develop appropriate solutions [61-62].

For the circular array in Figure 2.6, the identical radiating elements are spaced by arc lengths of $R\Delta\varphi$ along the circle and have their main beams pointing in the radial direction. Equation (2.4) returns the expression of the antenna factor of a circular antenna array in the azimuth plane [63].

$$AF(\theta,\varphi) = \sum_{n=1}^{N} a_n f(\theta - n\Delta\varphi) e^{j\beta_0 R \cos(\theta - n\Delta\varphi)} \tag{2.4}$$

Here, a_n represent excitation coefficients for the n^{th} element, $f(\theta - n\Delta\varphi)$ is the rotated normalized radiation pattern of each element, $\Delta\varphi$ is the angular separation between the elements in the circular array (which is $2\pi/N$), R is the radius of the array and β_0 is the wavenumber in free space [63].

In [56], a new configuration of fast beam steering antenna using an agile mechanical feed system for exciting circular arrays was proposed. The structure consists of a fixed circular array of antenna elements (patch antennas) which were excited by a parallel plate waveguide (PPW) acting as the circular beamforming system which was rotated to ensure the 360° azimuth coverage (Figure 2.7). The patch antennas remained in their fixed positions while the beam was steered. Therefore their weight did not contribute to the moment of inertia of the rotating structure. Of course, in the case of patches the moment of inertia is quite small and there is not much advantages. However, the concept is equally applicable to other radiating elements, such as linear waveguide-fed slot arrays, which are heavy and bulky. In that case the reduction of inertia is significant. Only the azimuth scanning was addressed. In our project, these patches would have to be replaced by vertical

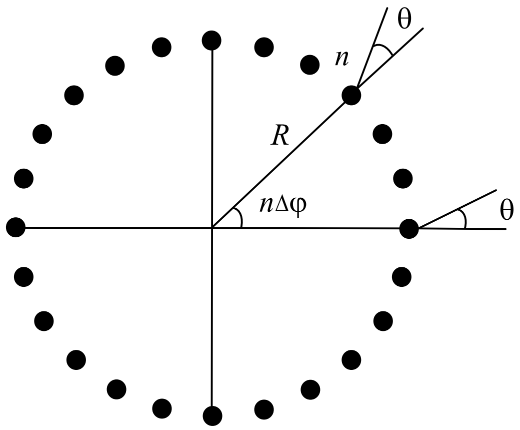

Figure 2.6: Circular configuration array.

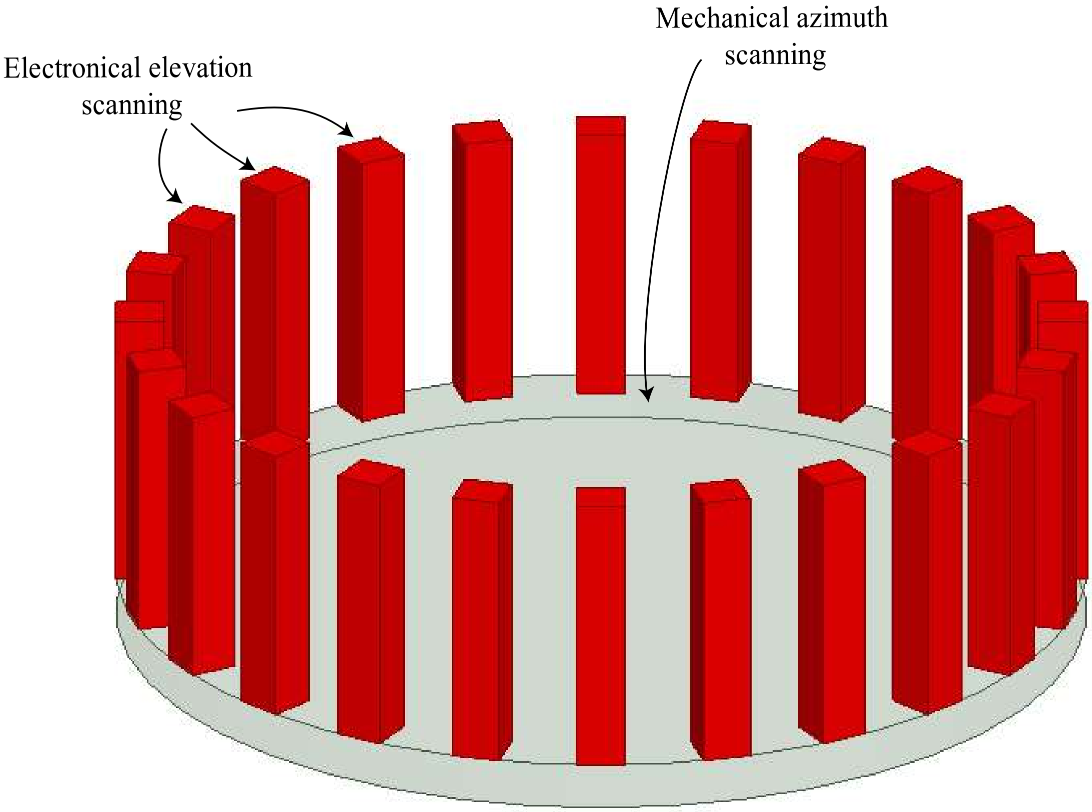

Figure 2.7: Fast beam steering antenna with an agile mechanical feed system for exciting circular array presented in [55].

configuration arrays such as broad-wall/narrow-wall slotted waveguide that are long enough to provide the desired beamwidth and beam scanning in the elevation.

A continuous PPW delay lens beamformer was presented in [64] with the goal of providing wide scanning performance while maintaining the mechanical design in a possible simple way [65]. This beamformer solution was defined using a technique similar to constrained lenses ([66-69]) to produce multiple focal points enabling to steer in a wider angular range without the complexity and limitation in bandwidth resulting from the lens discretization [65]. The proposed continuous PPW delay lens [64] is characterized by a transversal ridge in the PPW section which limits the shape of the inner and outer lens contour in order to generate the desired wave fronts for multiple beam applications [65].

2.3 Slotted Rectangular Waveguide Antennas

In our project, we benefit moving small parts (dielectric slabs) in a rectangular waveguide in order to scan the beam. A class of antenna design problems of wide practical interest includes linear or planar arrays of uniformly spaced slots cut in one of the walls of a rectangular waveguides [70]. In this work, we have established the slots on the broad wall and narrow wall of the waveguide with rotating dielectric slabs in them in order to scan the main beam. The physical parameters and also the arrangements of the slots need to be determined such that a specified pattern and a specified input impedance level are achieved. To do this successfully we must account for the mutual coupling between slots. Thus there is need to develop some design curves which relate slot admittance/impedance with the slot physical parameters [71]. For radiating broad wall slots, design curve of resonant length and offset from the waveguide center plane against slot admittance are required.

In the past, researchers used to achieve these curves through investigation by making repeated measurements on fabricated modules but it was an expensive, annoying and a time consuming method [71]. In addition, the measurement and fabrication errors have been increased. Integral equations [72] or FDTD techniques [73-74] is useful to evaluate properly the slot characterizations. In [74] simulation models were introduced for precisely evaluating waveguide slots in a full wave EM analysis software.

Once design data is achieved for radiating resonant elements, the next steps is to form a slot array antenna. R. S. Elliot [75] in 1978 presented a method for the design of linear and planar slotted waveguide antennas containing the effect of mutual coupling between the radiating elements. In 1983 [76] he established the same design process to be applied for a dielectric filled slotted waveguide. Later, Elliot took into account the effects of internal higher order mode coupling between radiating elements in his method [77]. The broad wall slotted waveguide presented in this work has been designed including the effects of mutual coupling between radiating elements.

2.3.1 Rotating Dielectric Slab inside the Waveguide

Earlier work around a similar concept [78] used a rotated metallic bar instead of dielectric slabs (see Figure 2.8). The drawback of this is the possibility to excite a TEM mode, with zero cutoff

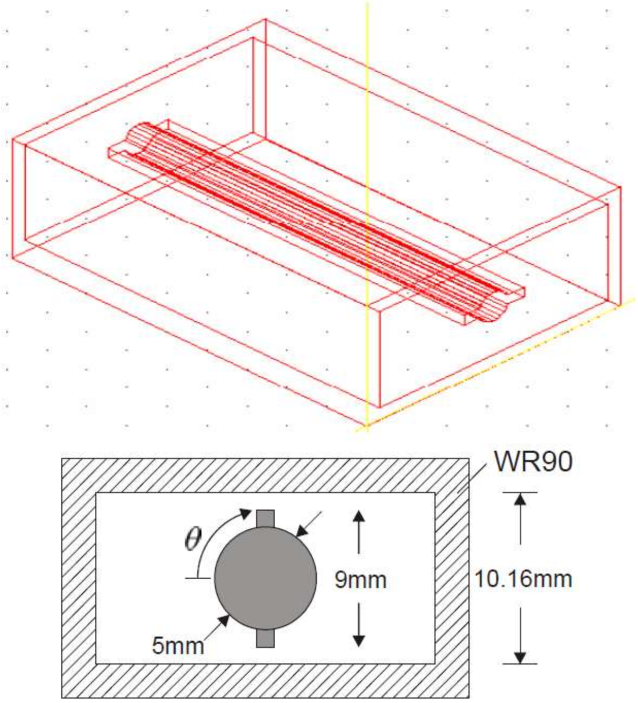

Figure 2.8: Rectangular waveguide with a rotating metallic bar presented in [78]. The metallic bar is supported with a solid sylindrical dielectric rod.

frequency in the waveguide in addition to the desired TE_{10} mode. By using dielectric slabs instead of metal, we eliminate the possibility of a TEM mode. A wide single mode band of operation is possible.

In addition, the concept of Solbach *et al.* used only one rotated bar, which created asymmetric field distribution in the waveguide when the rotation was oblique. As a consequence, the slots on either sides of the waveguide center plane had different amplitude excitations depending on rotation, which led to large variations of return loss and poor stability of the antenna pattern. In our design, the symmetric arrangement of the slabs alleviates these effects that will be discussed in the next chapters.

2.3.2 Non-resonant slotted waveguide array

A basic type of slotted waveguide antenna is non-resonant array in which the slots are not spaced at half-wave intervals in order to avoid in-phase reflections. In non-resonant arrays, as the excitation waves travel along, the array part of it is radiated, leaving only a small part goes to the load [14]. The slot susceptance should be zero or smaller, so that the maximum power could be radiated. Larger waveguide arrays will have lower conductances per slot and larger conductance

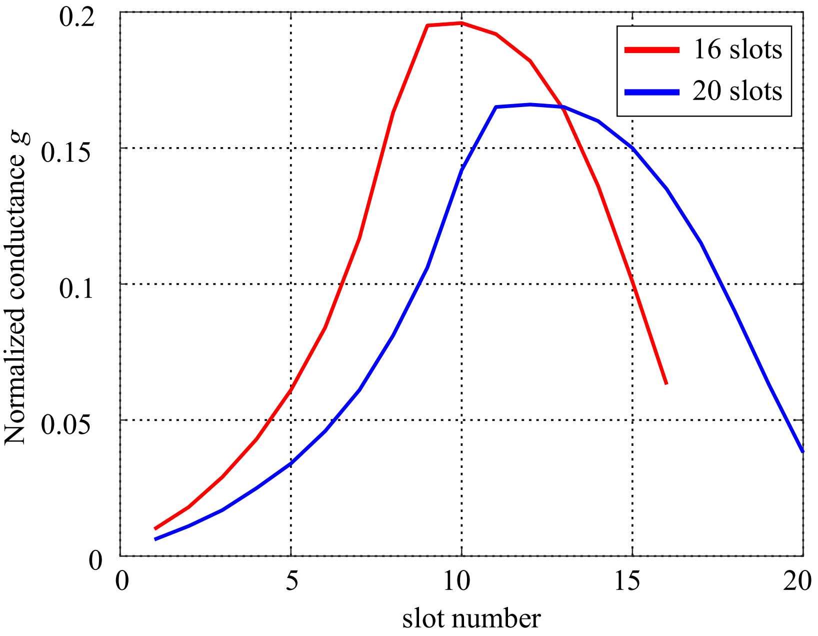

Figure 2.9: Comparison of triangular distribution of normalized conductance for arrays of 16 and 20 slots.

values are not only difficult to realize, but the effect of mismatch impedance may no longer be negligible [14]. The values of conductance are proportional to the part of power goes to the load.

Figure 2.9 shows a comparison of triangular distribution of normalized conductance for arrays of 16 and 20 slots and with 15% of power dissipated in the load. As the number of slots increase, the values of conductance and consequently the current amplitudes decrease.

2.4 Conclusion

After reviewing the various ways to perform the beam scanning, we are now able to get an idea to develop new solutions for our antenna. An azimuth scanning concept has been proposed in [56]. It is required to develop the elevation beam scanning elements in order to reach the objectives discussed in Chapter 1.

Phased Array antennas are fast and accurate, however they are expensive and complicated to fabricate due to use of phase varying elements. The challenge would be to create a system to sweep the phase in a low cost way. Although, phased array antennas at a lower cost have been designed for example in [79], economical phased shifter design is still challenging. One way to reduce the cost is using passive phase shifters such as slotted waveguide.

Slot antenna arrays based on rectangular waveguides are used in many radars. When operated at a fixed frequency or in a very narrow band, which is typical for radars, frequency beam scanning based on series-fed arrays or LWAs cannot be used and instead the whole antenna has to be pivoted mechanically to scan the main beam. This is limiting the maximum scanning speed due to mechanical reasons, as for instance the inertia of the antenna platform itself. The solutions proposed in the next chapters allow beam steering without frequency variation and only needs rotation of small lightweight parts. They therefore have potential for higher steering speed, while maintaining high power handling which is currently needed in meteorological radar antennas.

CHAPTER 3 ARTICLE 1: A CONTINUOUS BEAM STEERING SLOTTED WAVEGUIDE ANTENNA USING ROTATING DIELECTRIC SLABS

Amirhossein Ghasemi, Jean-Jacques Laurin

Submitted in 2018 at IEEE Transactions on Antenna and Propagation

3.1 Abstract

The design, simulation and measurement of a beam steerable slotted waveguide antenna operating in X band are presented. The proposed antenna consists of a standard rectangular waveguide (RWG) section with longitudinal slots in the broad wall. The beam steering in this configuration is achieved by rotating two dielectric slabs inside the waveguide and consequently changing the phase of the slots excitations. In order to confirm the usefulness of this concept, a non-resonant 20-slot waveguide array antenna with an element spacing of $d = 0.6\lambda_0$ has been designed, built and measured. A 14° beam scanning from near broadside ($\theta = 4°$) toward end-fire ($\theta = 18°$) direction is observed. The gain varies from 18.33 dBi to 19.11 dBi and the antenna efficiency from 95% to 79%. The side-lobe level is -14 dB at the design frequency of 9.35 GHz. The simulated co-polarized realized gain closely matches the fabricated prototype patterns.

3.2 Introduction

Many types of beam scanning antennas have been designed and developed in the past. In particular, radar sensors for automotive applications use antennas with agile beams, either by mechanically moving the complete antenna or electronically scanning the beam of a fixed antenna [78]. Electromechanical beam scanning offers a low-cost solution but it is less agile compared to electronically steerable antennas. However, it can potentially be used at higher peak power levels because no electronic parts are used [56]. Special attention was paid to concept of a fixed antenna in which small parts are moved [80]. Many such concepts have been presented in [81-83], as candidates for millimeter wave scanning antennas and in [84-87] for satellite communications. The *Eagle Scanner* of World War II was possibly the first electromechanically beam scanning antenna and included movement of the narrow wall of a rectangular waveguide [88] in order to introduce phase shifting in a series-fed linear array. However, the realization of accurate and simultaneous linear displacement of the side wall over the total length of the antenna is not easy to accomplish.

Recent works on reconfigurable antennas have contributed an appropriate solution to accomplish the beam scanning with less complexity [89]. Such reconfigurable antennas use active components such as PIN diodes [90-91], varactor diodes [92] and microelectromechanical systems (MEMS) [93]. A possible disadvantage of using RF PIN as a switch is that it needs additional passive elements for the DC biasing circuitry, which may affect the antenna dimensions. Efficiency and return loss performance can also be affected [94]. Moreover, as the power increases, implementing the active components becomes more difficult and challenging because of their nonlinear response.

Frequency scanning antennas based on series-fed arrays or leaky-wave structures may possibly offer a simple and low-cost solution compared with phased arrays. However, frequency variation over a wide bandwidth to scan the main beam is required [95] which is not suitable for the narrow bandwidths generally allocated to the certain applications such as X-band weather radars.

In order to simplify the requirements of the beam steering mechanism, a new concept is proposed which consists of a waveguide linear slot array in which beam scanning is achieved by rotating two dielectric slabs inside the rectangular waveguide. The configuration is inspired by an earlier design of a waveguide phase shifter presented in [96]. In this design, the wavelength of the travelling wave is changed depending on the angle of the slabs relative to the dominant mode field.

The proposed design allows continuous beam scanning without semiconductor devices and therefore can handle high power compared to the concepts presented in [90-91]. Although this concept has been first presented in [81] and worked out in [78], this work exhibits more scan range with low side-lobes due to symmetric field distribution inside the waveguide. Furthermore, a matched transition from a coaxial port to the waveguide filled by the rotating slabs is presented.

The paper is organized as follows. Section II introduces the design methodology of the slotted waveguide antenna. In Section III, engineering details on the design method are given. Finally, simulation and experimental results are provided and discussed in Section IV.

3.3 Design of the slotted waveguide antenna

3.3.1 Rotating dielectric slabs inside the waveguide

The experimental evidence of the scanning capabilities realized by rotating a single ridge in a metal waveguide was given by Solbach *et al.* [78]. Such configuration allows the propagation of a TEM mode. The longitudinal slots in a rectangular waveguide are not excited by the TEM mode because the current flow is not perpendicular to the slots. However, at the feeding transition, modes can couple and therefore affect the return loss. Also, the power in the TEM mode will be dissipated in the terminating load, resulting in reduced the antenna efficiency. In [78], another drawback was the presence of high side lobes due to the asymmetric field distribution inside the waveguide. The asymmetry of the structure can be observed in Figure 3.1a, showing the non-symmetric excitation of the slots on the RWG when the position of single slab is oblique. To avoid the asymmetric coupling, we propose using two symmetrically positioned rotating slabs in the waveguide, as shown in Figure 3.1b. Also, the slabs are made of dielectric instead of metal in order to eliminate the TEM mode.

The dimensions of the waveguide and the dielectric slabs have to be chosen to ensure single mode propagation at the desired frequency of operation, and to maximize the variation of the mode propagation constant with the rotation of the slabs. In order to simplify the fabrication, a standard WR-62 waveguide size made of aluminium was used. Figure 3.2 shows the propagation constant versus frequency for two different dielectric slabs with relative permittivities of 6.15 and 10.2. Since the cutoff frequency of the second mode for the case $\varepsilon_r = 10.2$ is close to the design frequency of 9.35 GHz, the dielectric with $\varepsilon_r = 6.15$, corresponding to RT/Duroid 6006 from Rogers, is preferred. The dimensions are given in Table 3.1. The values of a_{slab} and $d_{rotation}$ were varied in simulations to maximize the variation of wavenumber β_g. The curves of Figure 3.2 were obtained with the 3D full-wave solver of Ansys-HFSS, with no slots on the waveguide. The cut-off frequency of the air-filled WR62 waveguide is 9.49 GHz. In Figure 3.2a we see that it varies between 7.6 and 8.5 GHz for the fundamental mode, depending on the rotation state of the slabs. It can be noted that at the chosen operation frequency of 9.35 GHz applicable to weather radars, the 2nd mode is well attenuated and the waveguide supports only one mode for all the rotation states of the slabs when $\varepsilon_r = 6.15$.

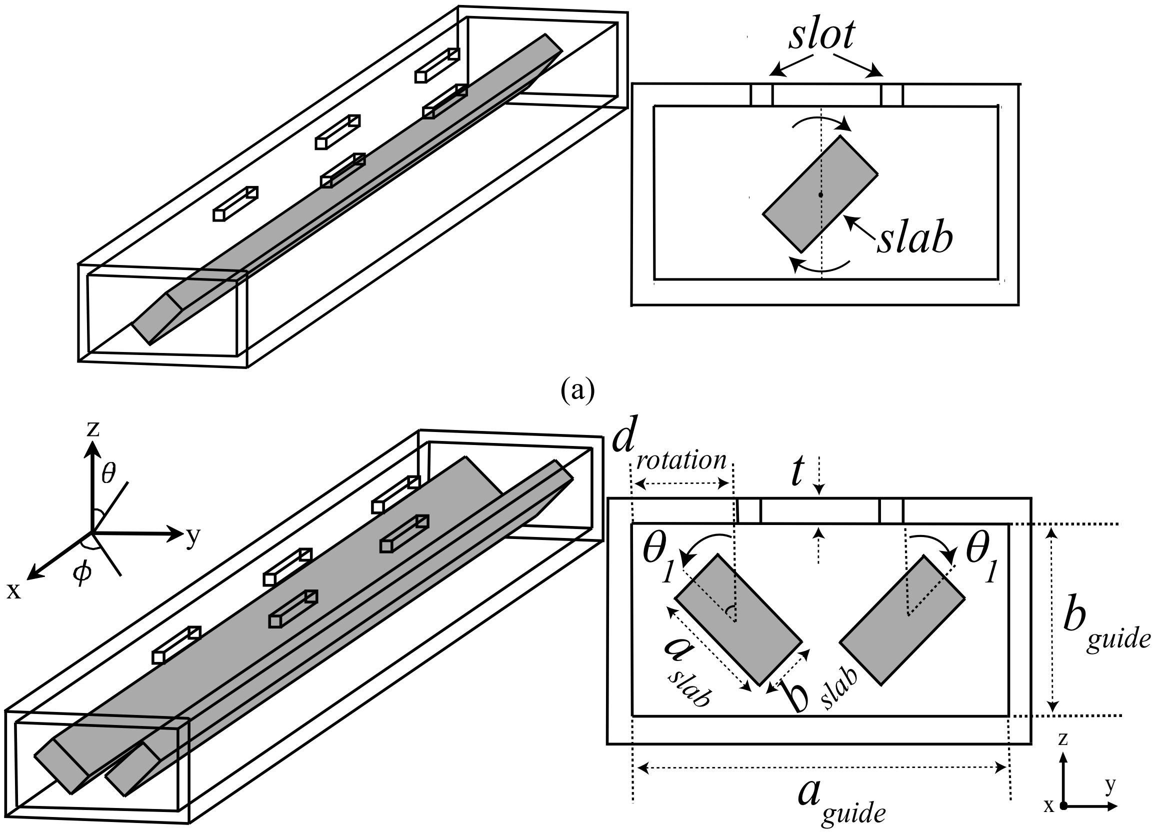

(a)

(b)

Figure 3.1: Simulation model of the rotating dielectric (a) single slab, (b) two symetrically positioned slabs.

3.3.2 Non-resonant array with the slots alternatively displaced

The two basic types of slotted waveguide antennas are the resonant array (standing wave) and the non-resonant array (travelling wave). Since we wish to scan the beam off-broadside, the case of interest is the non- resonant array. For that case, the slot-to-slot spacing differs from $\lambda_g/2$ so the reflections from the different slots do not add up in phase at the input of the waveguide, leading to

Table 3.1: Dielectric Slab and Waveguide Parameters

a_{guide}	b_{guide}	a_{slab}	b_{slab}	t	ε_{r_slab}	$tan\ \delta_{slab}$	$d_{rotation}$
15.8mm	7.9mm	5mm	2.5mm	1mm	6.15	0.0019	4.45mm

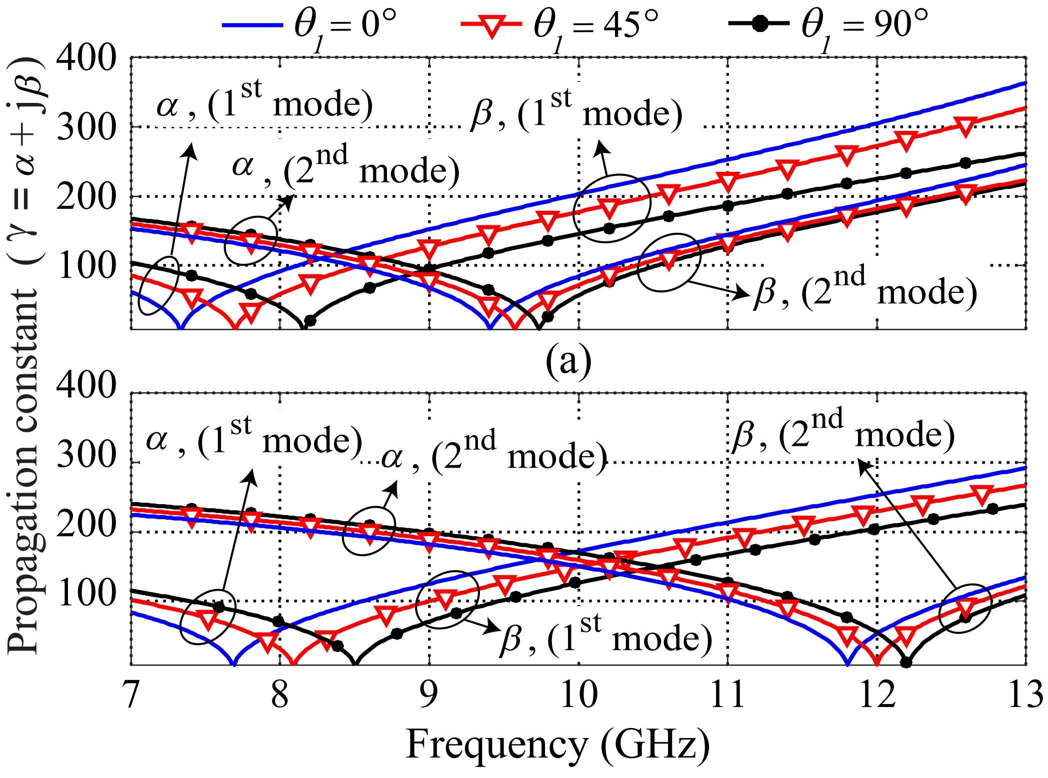

(b)

Figure 3.2: Propagation constant for the different rotation states of the dielectric slabs of (a) $\varepsilon_r = 6.15$ ($tan\ \delta = 0.0019$) and (b) $\varepsilon_r = 10.2$ ($tan\ \delta = 0.0023$). Waveguide simulated without slots.

a small reflection coefficient. Thus, the aperture distribution experiences a phase progression that is uniform, or nearly so, which is why these arrays are also referred to as travelling wave fed arrays [96]. Non-resonant arrays include a matched-load termination, necessary to avoid undesirable reflection causing a back-lobe responsible for the degradation of the antenna pattern. The main advantage of these arrays is a larger bandwidth in terms of side lobe level (SLL) and input matching, which makes them suitable for performing as beam scanning antennas [96]. In the non-resonant slotted waveguide antenna, the slot spacing can be chosen so that we can produce a main lobe at almost any arbitrary angle θ relative to the axis of the array. If offsets are alternated on opposite sides of the symmetry plane, then the array factor is given by [97]:

$$AF = \sum_{n=1}^{N} a_n e^{[jn(\beta_0 d \sin\theta - \beta_g d + \pi)]} \tag{3.1}$$

where a_n is the slot excitation amplitude level, d is slot spacing, β_g is the guided phase constant and β_0 is the propagation constant in free-space. In order to have a good aperture efficiency, it is desired to scan the beam near broadside. Therefore, a non-resonant array with the slot spacing d is different, but close to $\lambda_g/2$ is necessary. The element spacing of $d/\lambda_g(\theta_l = 45°) = 0.4$ was chosen because array factor calculations based on the β_g values given in Fig. 2 for the design frequency of 9.35 GHz led to maximum beam deviation. By rotating the dielectric slabs from vertical to horizontal position, the wavenumber variation observed from Figure 3.2 is

$$\beta_g(\theta_l = 0°) - \beta_g(\theta_l = 90°) = 45 \text{ rad/m} \qquad (3.2).$$

This gives 14° of beam scanning based on (3.1). A 20-slot waveguide was chosen in this study based on limitations of the fabrication means available to the authors. A triangular amplitude distribution over a pedestal was used in order to demonstrate the capability to control the SLL.

If the relative excitation level of the n^th slot is a_n, the power P_n radiated by this slot will be proportional to a_n^2 ($P_n = ka_n^2$) [97].

Let r be the fraction of the incident power to be dissipated in the match load. The equivalent circuit for the array is shown in Figure 3.3. Assuming a 1-watt power input and a lossless waveguide, we must have $r + \sum_{n=1}^{N} P_n = 1$. According to the non-resonant array design method presented in [97] we have $g_n = \frac{P_n}{r+\sum_{i=n}^{N} P_i} = \frac{P_n}{1-\sum_{i=1}^{n-1} P_i}$. Figure 3.4 shows the values of distribution amplitude (a_n), radiated power (P_n) and normalized conductance (g_n) for a triangular taper excitation of a 20-element array, with $r = 0.15$.

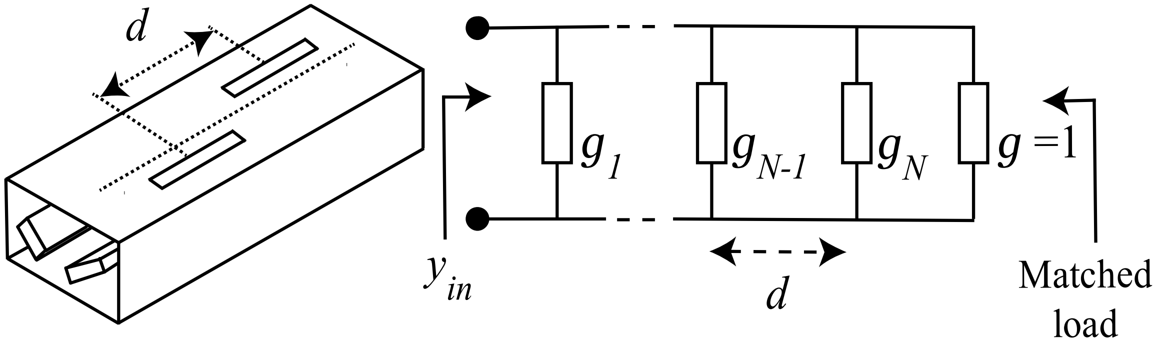

Figure 3.3: Physical form and equivalent circuit model of the non-resonant array.

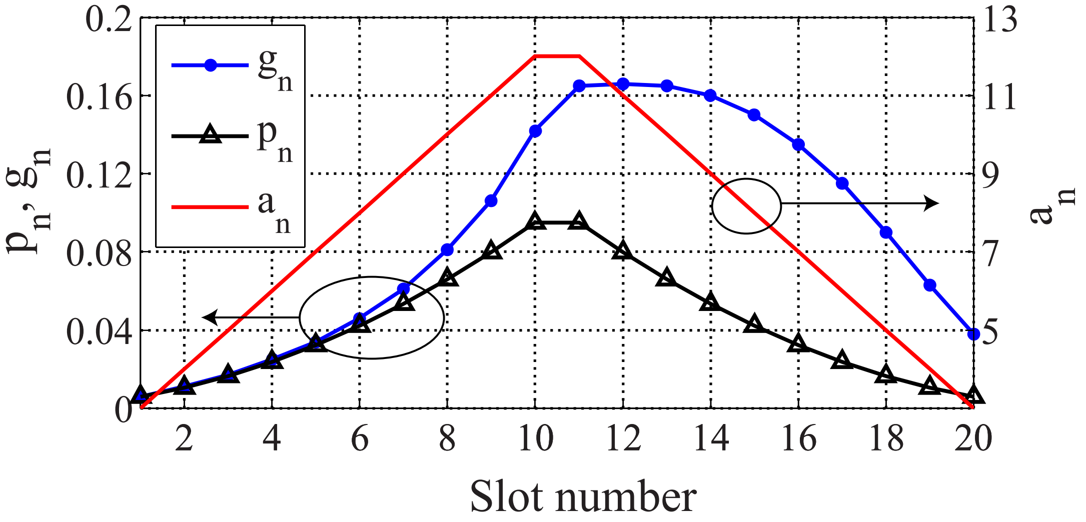

Figure 3.4: Triangular current amplitude distribution r = 0.15.

3.3.3 Evaluation of offset and length of the slot

We compare two different methods to analyze the dielectric-loaded slotted waveguide. The effect of mutual coupling between the slots is taken into account in both methods.

One way to consider the mutual coupling is to simulate an array of several coupled slots and extract their characteristics. For radiating slots, design curve of resonant length and offset from the waveguide center plane against slot admittance are required. Once lengths and offsets are obtained for the radiating slots, the next steps is to design a slot array antenna.

The design of the series-fed array is simpler if we can ignore the effect of coupling with adjacent elements. In order to observe if coupling has a significant effect, we have simulated resonant arrays of various length.

Method 1: Resonant array

Although we are considering scanning non-resonant arrays, the resonant array case is useful to estimate the admittance of the slots. As Figure 3.5 illustrates, the slots of resonant arrays are spaced by $\lambda_g/2$, so that all of them share the same phase excitation necessary to produce a broadside main lobe. Typically, a short circuit is placed at the end of the waveguide, at a distance of $\lambda_g/4$ after the last slot. The input admittance y_{in} is the sum of all the admittances ($y_{in} = \sum y_i$) due to the spacing

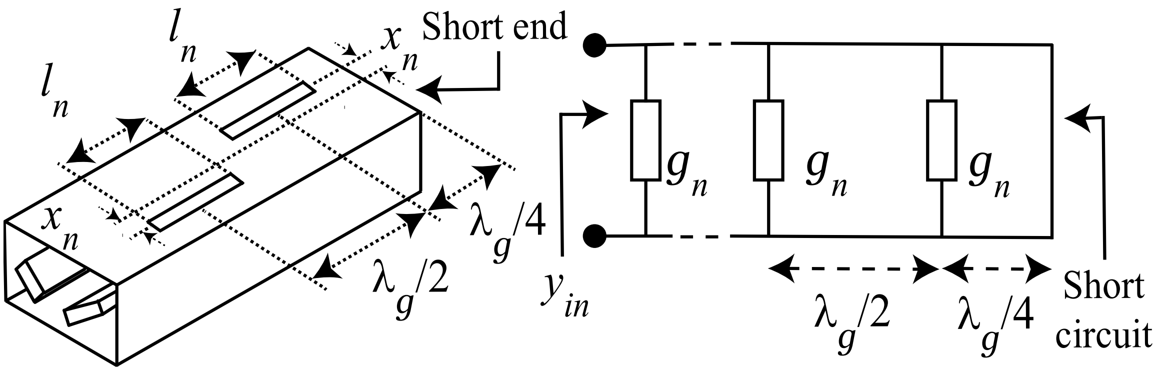

Figure 3.5: Physical form and equivalent circuit model of the resonant array.

of $\lambda_g/2$ between the elements. A linear relationship between the admittance (y_{in}) and the number of slots is obtained for array of 5 identical slots in the simulations.

Method 2: 2-slot non-resonant array using periodic boundary condition

In this method, we use periodic boundary conditions to simulate a large array of mutually coupled slots, as described in [98]. This method also assumes a uniform amplitude excitation but it is still helpful to design the proposed array because the change in the excitation coefficients is gradual as shown in Figure 3.4. The periodic boundary condition is implemented using Master-Slave boundaries in Ansys-HFSS. Figure 3.6 illustrates the 2-slot non-resonant array with periodic

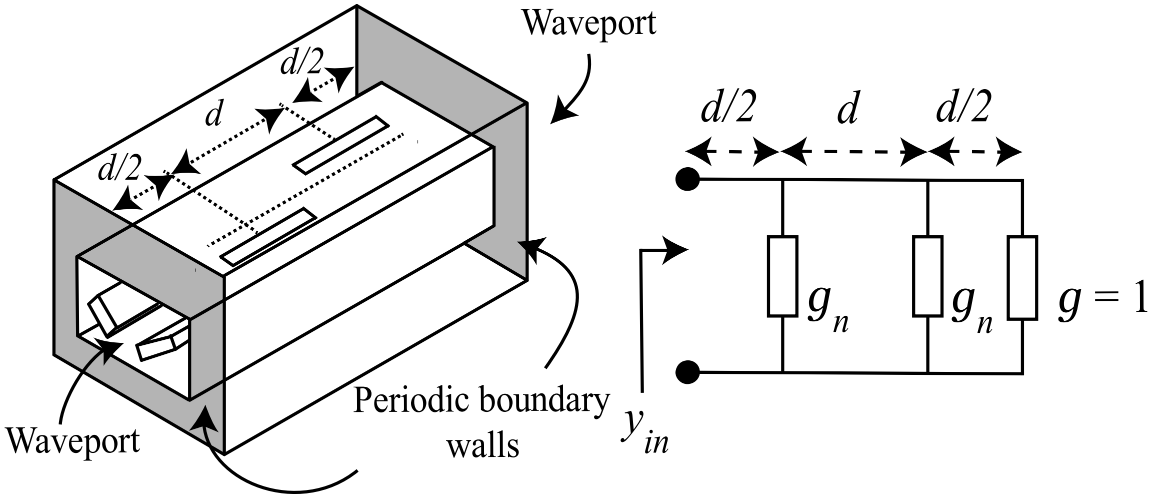

Figure 3.6: Physical form and equivalent circuit model of the non-resonant array with periodic boundary condition.

boundary walls. In this method, the value of d is not necessarily $\lambda_g/2$. We have used $d = 0.4\lambda_g$ because it corresponds to $\theta_l = 45°$, which is in the middle of the range.

For both methods, we need to find the resonant length (l_r) for each given slot offset (x_i) for each slot. This was accomplished by running a parameter sweep with HFSS for each x_i. The normalized susceptance (b) of the slot must be zero at resonance. The parameter sweep returns a set of admittance points that was processed in order to determine l_r (i.e. corresponding to zero susceptance) for a given slot offset.

For that, we used an interpolation routine implemented in Matlab to generate a contour corresponding to the resonant condition in the length-offset plane for each method. This contour is shown in solid curves in Figure 3.7. Then, for each point on this contour we can determine the corresponding conductance (g) at resonance, see Figure 3.7. At the end of this process, two interpolation polynomials for each method were derived to give the slot resonant offset (x_r) and l_r versus required resonant slot conductance. These interpolation curves are illustrated in Figure 3.8.

Using the values of conductance from the triangular distribution given in Figure 3.4 and the polynomials shown in Figure 3.8 we can obtain the resonant parameters of the antenna.

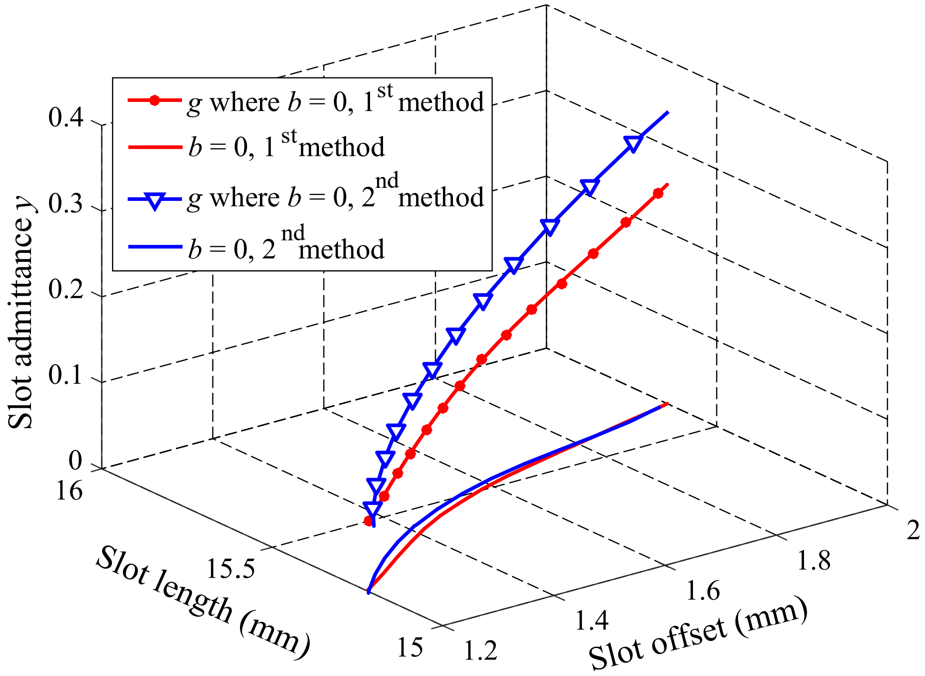

Figure 3.7: Slot admittance (y) versus slot length (l) and slot offset (x).

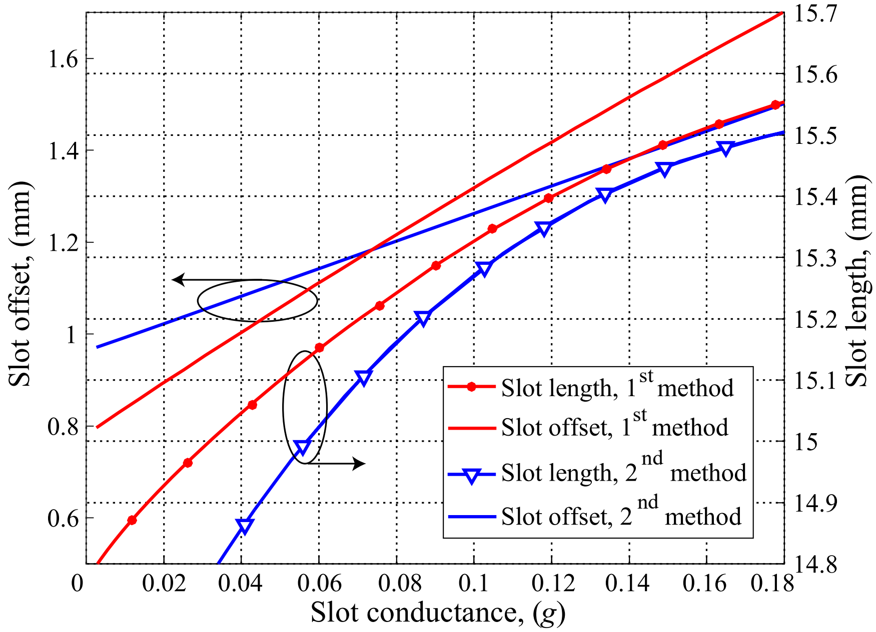

Figure 3.8: Slot offset and slot length versus slot conductance, obtained for $\theta_1 = 45°$.

Table 3.2 summarizes the final antenna parameters calculated for both methods. As can be seen in the table, the difference between the resonant lengths obtained with the two methods is very small. The largest difference is 0.32 mm (about 2%) and it occurs for n = 1 where amplitude weight (a_1) is very small. As for the slot offsets, the largest difference observed at n = 11 and n = 13 is 0.19 mm (about 13%) where amplitude weighs are large. The impact of these differences on the antenna pattern are shown in Section II. D.

Table 3.2: Slot current distribution a_n, conductance g_n, offset x_n(mm) and length l_n(mm) for the 20-slot array design using triangular amplitude distribution

n	a_n	g_n	x_n (#1)	l_n (#1)	x_n (#2)	l_n (#2)
1	3	0.006	0.80	14.81	0.98	144.49
2	4	0.011	0.83	14.84	0.99	14.55
3	5	0.017	0.86	14.89	1.01	14.62
4	6	0.025	0.91	14.94	1.03	14.71
5	7	0.034	0.96	15.00	1.06	14.80
6	8	0.046	1.03	15.07	1.10	14.91
7	9	0.061	1.11	15.16	1.14	15.03
8	10	0.081	1.22	15.25	1.20	15.16
9	11	0.106	1.35	15.36	1.28	15.30
10	12	0.142	1.53	15.47	1.38	15.42
11	12	0.165	1.64	15.53	1.45	15.48
12	11	0.166	1.64	15.53	1.46	15.48
13	10	0.165	1.64	15.53	1.45	15.48
14	9	0.160	1.61	15.52	1.44	15.47
15	8	0.150	1.57	15.49	1.41	15.44
16	7	0.135	1.50	15.45	1.36	15.40
17	6	0.115	1.40	15.39	1.30	15.33
18	5	0.090	1.27	15.29	1.23	15.22
19	4	0.063	1.13	15.17	1.15	15.04
20	3	0.038	0.99	15.03	1.07	14.83

3.3.4 Array simulation

In order to validate the design approach, the values of g_n in Table 3.2 were used in a simulation of the circuit model shown in Figure 3.3 (using ADS® from Keysight). The complex currents (i_n) in the shunt conductances representing the slots were used to calculate the array factor with:

$$AF_{ct} = \sum_{n=1}^{N} i_n e^{[jn(\beta_0 d \sin\theta+\pi)]} \tag{3.3}$$

This procedure takes in consideration the propagation and the multiple reflections between the loads (i.e. the g_n's) in the transmission line network. The resulting array factors are plotted in Figure 3.9 (solid curves), along with the normalized H-plane patterns of the array with the various slabs rotation angles simulated with HFSS. Simulations are shown for designs based on the two sets of slot parameters given in Table 3.2. The beam steering of 14° predicted by the variation of

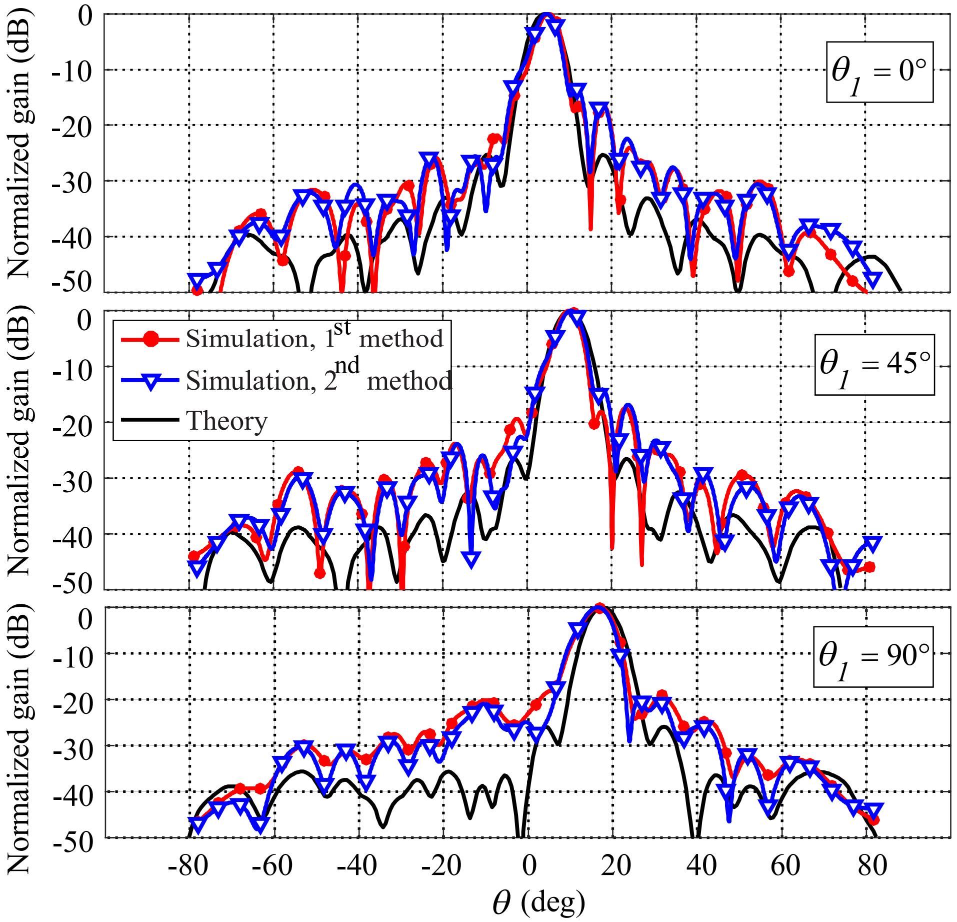

Figure 3.9: Comparison of the normalized H-plane ($\phi = 0$, see the axes presented in Fig.1) antenna factor simulated with HFSS with the normalized array factor obtained from circuit analysis (eq. (3)).

β_g is nearly achieved in both cases. The two full-wave results are very similar in terms of beamwidth and SLL. Looking at the three cases of slab rotation shown in Figure 3.9, there is no clear advantage of one method over the other. The fabricated prototype presented in Sections 3.4 used the values of x_{n} and l_{n} obtained with Method 1.

3.4 Design guidelines

3.4.1 Matched load design

Non-resonant slotted waveguide arrays require a matched load termination. In this section, the design of a matched load for the dielectric loaded waveguide used in the antenna is proposed. Standard rectangular waveguide matched load cannot be used since our waveguide is loaded with dielectric slabs. However it is quite straighthforward to design a matched load by inserting absorber material. At this end, we havechosen the DD-10214 Silicon from ARC Technologies Inc, with $\varepsilon = (17 - 0.2j)\varepsilon_0$ and $\mu = (1.6 - 1.8j)\mu_0$ at the operation frequency of 9.35 GHz. Absorber strips with a thickness of 0.762 mm were placed on one of the broadwalls of the waveguide. Based on this information, a load for WR62 with rotating dielectric slabs has been designed. As illustrated in Figure 3.10, a stand made of Rohacell was used to support the slabs and since it is located after the absorber, it is not causing reflections. Return loss greater than 25 dB was obtained in simulations over a wide frequency range for the all rotation angles of the dielectric slabs (see Figure 3.10).

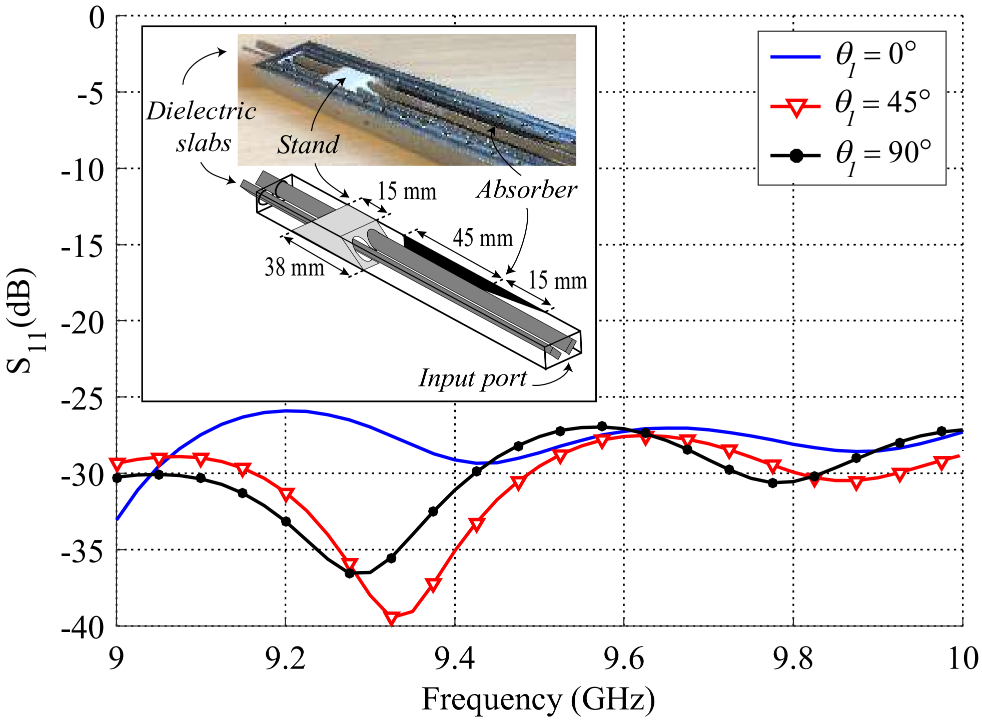

Figure 3.10: WR62 matched load, simulated return loss result in different slabs positions.

3.4.2 Waveguide transitions

The cut-off frequency of the air-filled WR62 waveguide is 9.49 GHz. Since our operation frequency for the RWG loaded with dielectric slabs is 9.35 GHz, it is required to reduce the cut-off frequency of the waveguide feeding the antenna. This was realized with a metallic ridge, as shown in Figure 3.11, which reduced the cut-off frequency to 7.8 GHz. A coaxial to ridge waveguide transition was designed.

The size of the coaxial probe and its location with respect to the shorting wall were varied to optimize matching. Simulated return loss of more than 20 dB was achieved in the frequency band of interest, as shown in Figure 3.11. Then, a second transition, this time from the ridge waveguide to a waveguide loaded with dielectric slabs was designed. Wedge shaped tips on both the ridge and the dielectric slabs led to good simulated return loss for all rotation angles of the slabs, as shown in Figure 3.12 for three cases.

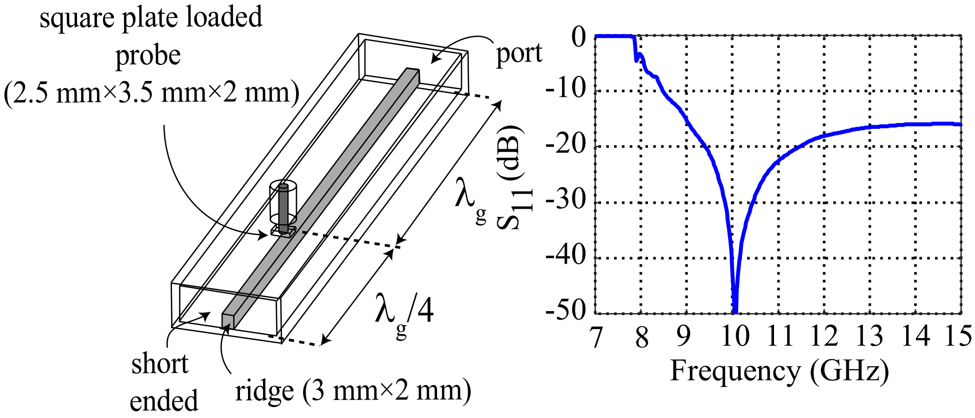

Figure 3.11: (a) Coaxial to waveguide transition, (b) simulated return loss.

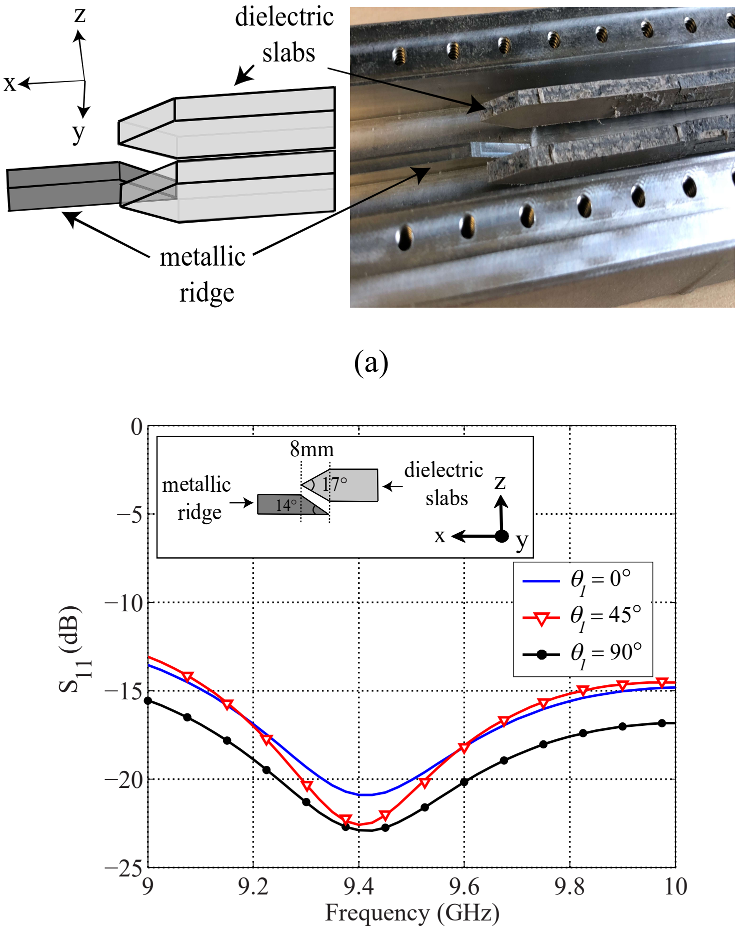

(a)

(b)

Figure 3.12: Triangular tapering cross section of the dielectric slabs and the ridge, (a): Simulated model and fabricated prototype, (b): Return loss of the Coaxial to waveguide transition.

3.4.3 Directional flare

In order to improve the gain of the antenna, a low-profile flare section was added on the broad wall radiating surface of the waveguide (Figure 3.13). This generates a narrower beam in the E plane. The triangular amplitude taper of the slots excitation was maintained in order to keep the H-plane side lobes low. The dimensions of the directional flares were varied in HFSS simulations in order to achieve maximum antenna gain. The optimal values of H and α are shown in Figure 3.13. The realized gain increases by about 4 dBi with addition of the flare, as shown in Figure 3.14. It should

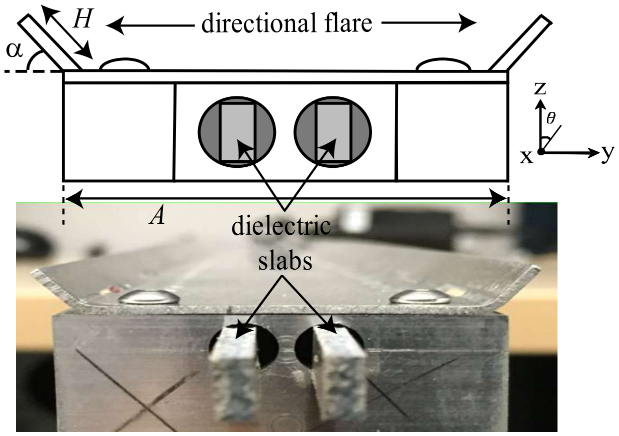

Figure 3.13: Configuration of the waveguide with directional flare. The parameters are $A = 32\text{mm}$, $H = 5.5\text{mm}$, and $\alpha = 40°$.

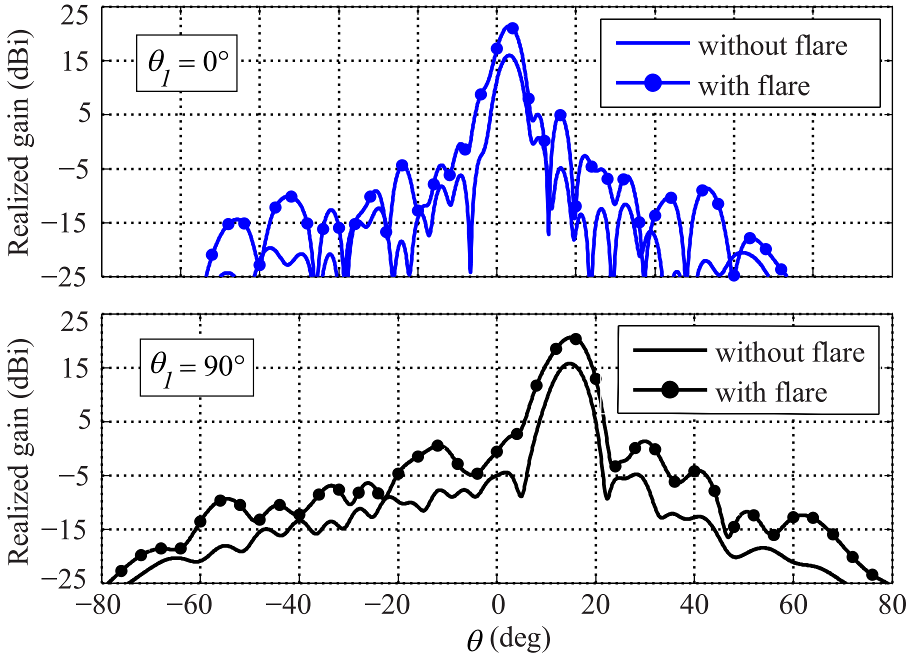

Figure 3.14: Effect of the flare on the simulated H-plane radiation pattern (($\phi = 0$), see the axes presented in Figure 3.1) of the antenna.

be noted that, if a much larger value of H is used, a horn is formed and the gain will increase more but the 3-dB gain beamwidth in the E-plane will decrease and the antenna would not generate a fan beam.

3.5 Prototype of the antenna and measurement

An antenna prototype has been built using the WR62 standard waveguide according to the detailed design given in sections 3.3 and 3.4. The 20 slots have been milled onto the upper broad wall in accordance with the dimensions of the resonant parameters given in Table 3.2. The coaxial to waveguide transition and the matched-load described in Section 3.4 were implemented. A prototype of the antenna can be seen in Figure 3.15. The dielectric slabs can be seen at the end of the waveguide. In our test they were rotated manually but adding a controlled motor is an easy task. It should be noted that although the antenna exhibits continuous beam steering with continuous rotating of the dielectric slabs, measured patterns are only shown here for θ_1 = 0°, 45° and 90°.

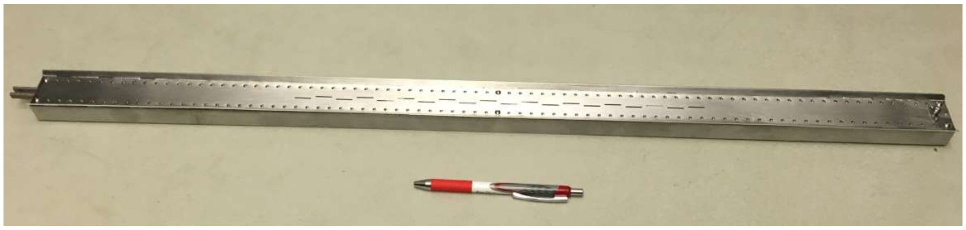

Figure 3.15: Prototype of the 20-slot array antenna.

3.5.1 Impedance matching

Measurement of the return loss has been made on the antenna coaxial port for three positions of rotating slabs. The results are shown in Figure 3.16, together with the simulations. The antenna was designed for a frequency of 9.35 GHz and $\theta_1 = 45^\circ$. We can see that return loss is greater than 10 dB for the three rotation states. A good agreement between measured and simulation S_{11} parameters is obtained for three slab rotation states over the frequency band of 9 GHz to 10 GHz (BW = 10.5%).

The power lost in the terminating load was not measured due to the non-standard waveguide at the end of the antenna, but the S_{21} parameters were simulated with HFSS and are also shown in Figure 3.16. In the simulations, port 2 replaces the matched termination at the end of the waveguide. The array was designed by assuming dissipation of 15% (−8.2 dB) of the input power in the terminating load. We can see in Figure 3.16 that the simulated S_{21} at the design frequency of 9.35 GHz for the three rotation states is less than −10 dB which is lower than the assumption.

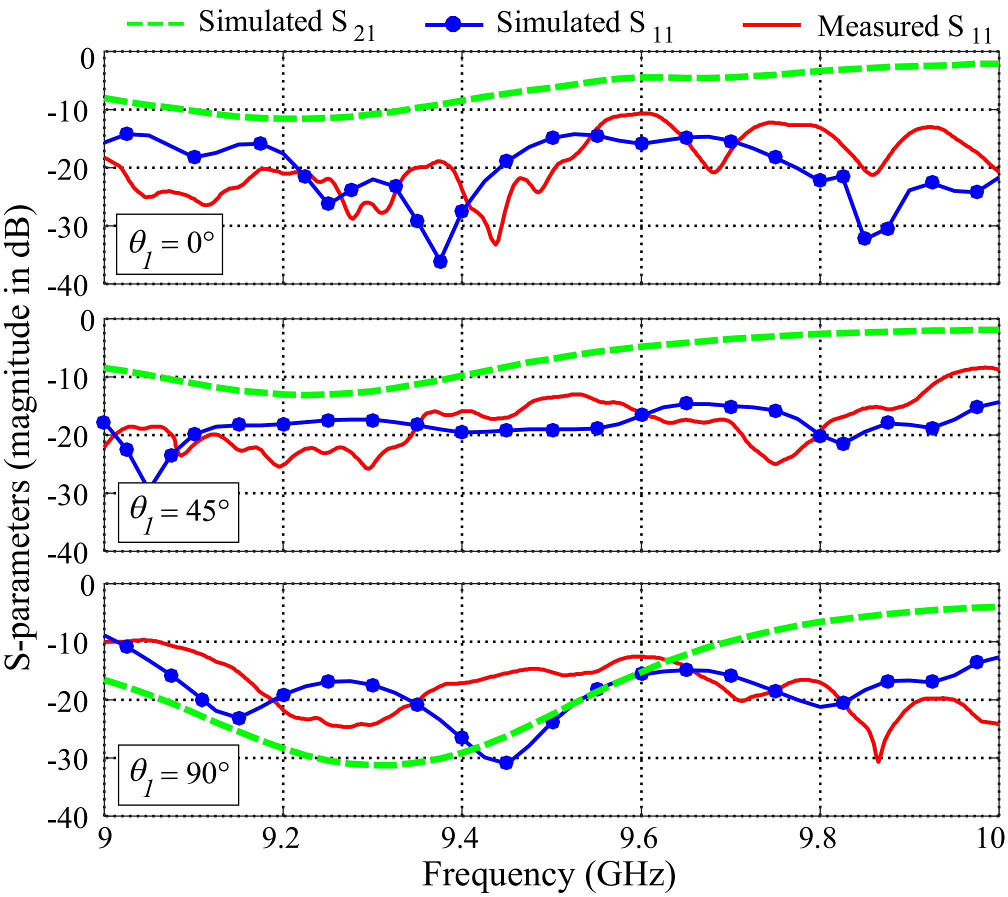

Figure 3.16: Return loss of the antenna, simulated and measured in different position of the dielectric slabs.

3.5.2 Radiation patterns

The radiation properties of the antenna prototype were simulated with HFSS and have been measured in an anechoic chamber. H-plane patterns of the realized gain at the design frequency of 9.35 GHz are presented in Figure 3.17. A good agreement is obtained between simulations and measurements for the three scanning states. As expected, the main beam steering for θ_1 varying from 0° to 90° is around 14°. The measured and simulated tilt angles and beamwidths are slightly different, but the differences are more visible on the side lobes, especially at $\theta_1 = 0°$. As seen in Figure 3.9, the triangular tapered distribution applied is leading to a SLL of about −25 dB in theory. However, both simulated and measured patterns have higher SLLs. The discrepancies between measurements and simulations have multiple causes. This includes the mechanical errors during fabrication and assembly of the antenna structure, inaccurate setting of angle θ_1 in the experiments,

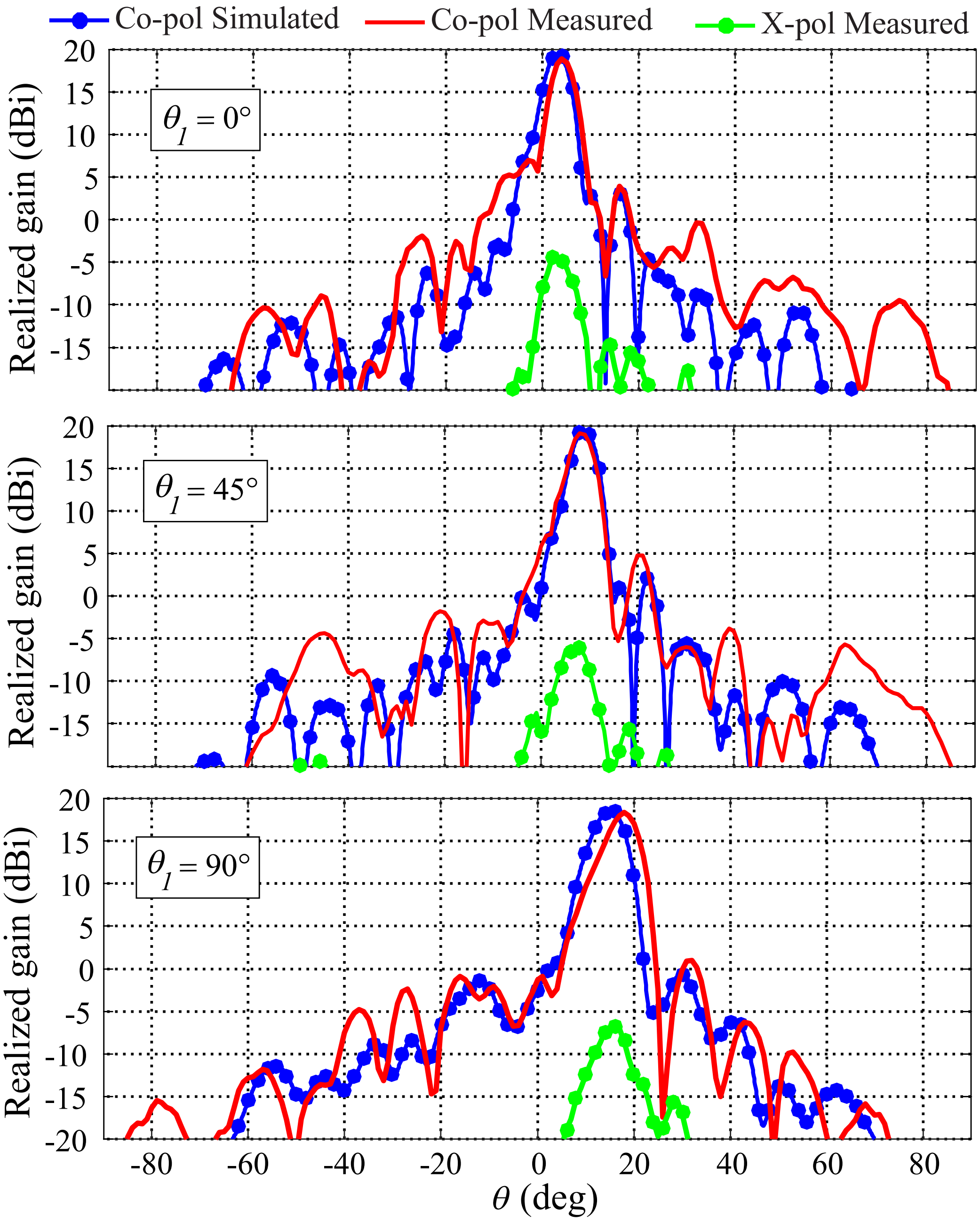

Figure 3.17: H-plane radiation patterns (($\phi = 0$), see the axes presented in Figure 3.1) of the antenna, simulated and measured in different values of θ_1.

inaccuracies of the specified material properties for the dielectric slabs and matched load absorbers, etc. A detailed sensitivity analysis would be required to understand each of these effects, but this has not been considered in this work.

The cross-polarization levels at H-plane have also been measured. For the operating frequency, they remain 20 dB below the co-polarization level in the main beam direction.

3.5.3 Antenna gain

The realized gain of the antenna for three rotating angles has been measured by the gain comparison method in the anechoic chamber. This gain is shown in Figure 3.18a. The antenna efficiency based on simulated realized gain and directivity is shown in Figure 3.18b. The maximum in gain and

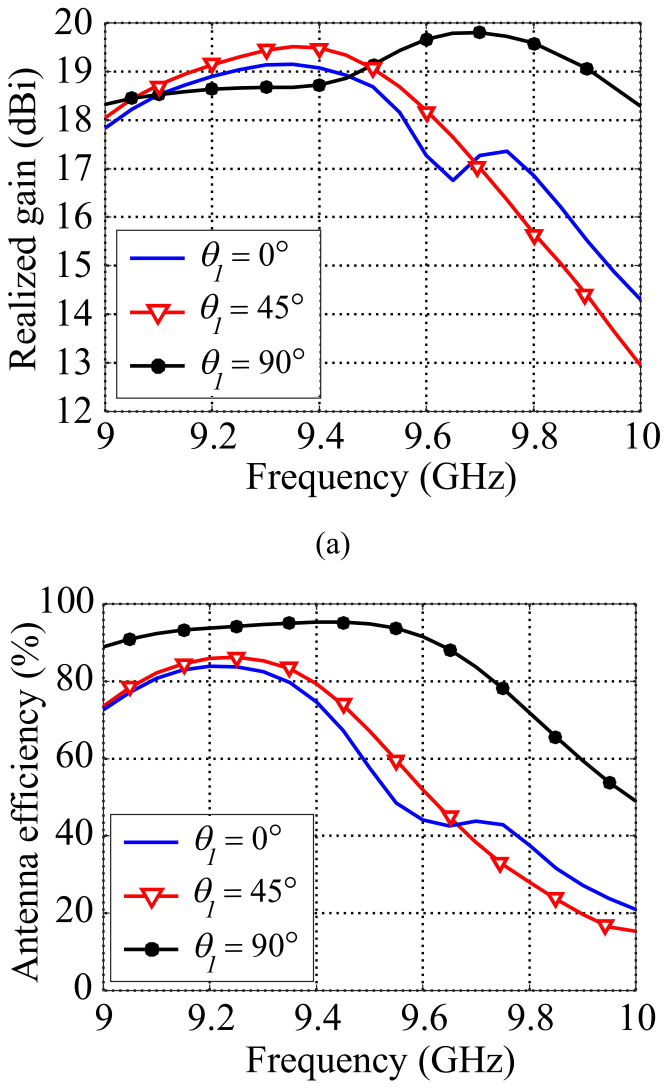

(a)

(b)

Figure 3.18: (a) Measured realized gain and (b) antenna efficiency versus different rotations of the dielectric slabs. The antenna was designed for a frequency of 9.35 GHz and $\theta_l = 45^\circ$.

efficiency are close to the target frequency of 9.35 GHz for θ_1 = 45˚. Figure 3.19 illustrates simulated realized gain and main beam direction over a continuous range of rotation angles of θ_1.

The simulated reflection coefficient for θ_1 = 45° and at the design frequency is around −19 dB, corresponding to a power loss of 1.25%. Based on simulations at the design frequency and for slabs rotation of 45 degrees, the realized gain is 19.52 dBi and the directivity is 20.32 dBi. This gives an overall antenna efficiency of 83.2%. The sum of return loss (S_{11} = −19 dB) and losses in the

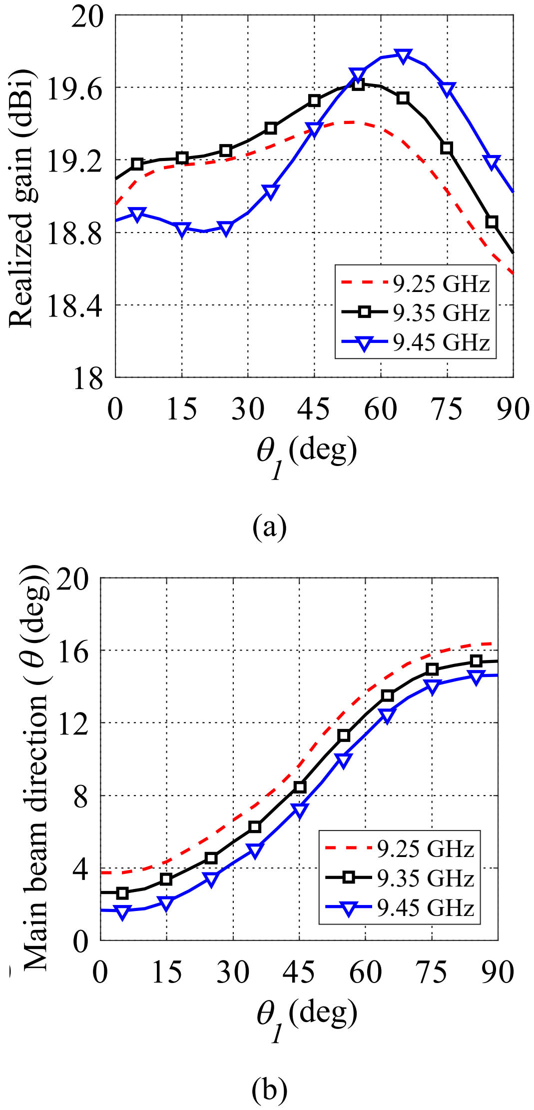

(a)

(b)

Figure 3.19: Simulated (a) realized gain and (b) main beam direction versus different rotations of the dielectric slabs (θ_1).

terminating load ($S_{21} = -11.23$ dB according to Figure 3.16), represents 7.53% of power. Therefore 8.02% of the incident power is dissipated in metallic and dielectric materials.

At the design frequency and for $\theta_1 = 45°$, the measured 3-dBi gain beamwidth in the H plane is 4.8˚ which is lower than the simulated value (5.14˚). As the gain decreases with scan, the 3-dB gain beamwidth correspondingly increases to 6.6˚ when the slabs are at $\theta_1 = 90°$. The simulated and measured radiation performance of the antenna at three rotation states of the slabs is summarized in Table 3.3.

Table 3.3. H-plane Radiation performance of the antenna at the design at 9.35 GHz

Slabs rotation states		$\theta_1 = 0˚$	$\theta_1 = 45˚$	$\theta_1 = 90˚$
Simulated	Beam direction (˚)	3	8.5	15.5
	Realized gain (dBi)	19.17	19.52	18.74
	3-dB gain beamwidth (˚)	5.18	5.14	7.25
	SLLs (dB)	-16.5	-16.46	-18.2
	Realized gain/Directivity (%)	79.6	83.2	95
	Dissipated power* (%)	9.7	8.02	4.2
Measured	Beam direction (˚)	4	8	18
	Realized gain (dBi)	18.85	19.11	18.33
	3-dB gain beamwidth (˚)	5.2	4.8	6.6
	SLLs (dB)	-14.3	-14.9	-17.33

$^{*}P_{dissipated} = 1 - |S_{11}|^2 - |S_{21}|^2 - P_{radiated}$

3.6 Conclusion

The design of the slot array antenna using rotating dielectric slabs inside the waveguide in order to allow continuous scanning of the antenna main beam has been presented. The antenna shows 14° of continuous beam scanning at the design frequency with a good scanning performance. Although the antenna was designed at a single frequency, it presents an overall experimental 10.5% bandwidth for 10 dB return loss. The SLL remains lower than −14 dB over the scanning range. The antenna realized gain ranges between 18.33 dBi to 19.11 dBi. The antenna efficiency including the reflection loss and losses in the terminating load is better than 79% over the scan range.

One of the difficulties in the proposed design is to preserve good matching conditions for all the rotation states of the slabs. In this work, we optimized matching of the tapered transitions between the ridge and dielectric-loaded sections by considering only three values of θ_1.

Although the experimental evidence of scanning capabilities of rotating a ridge in a metal waveguide slot array has already been explored by Solbach *et al.* [78], the proposed solution has lower side-lobes due to the symmetric field distribution inside the waveguide, more beam scanning range and no TEM mode propagation due to dielectric material used for the slabs.

The concept is promising for high power continuous beam scanning applications, and could be improved by applying a global optimization method. It would be also a less-complicated and cost-effective solution compared to the active phased-array concepts presented in [90-91].

Many antennas presented in literature [94] use periodically loaded leaky waveguides and operate on the frequency scanning principle. In certain applications such as X-band weather radars the allocated bandwidth is very narrow and such concepts cannot be used. The antenna proposed in this paper can realize beam scanning at a fixed frequency, and it is not limited in power handling due to the absence of nonlinear active components. Mechanical scanning speed is of course limited, but remains acceptable for slowly moving targets.

A good agreement between simulations and measurements also confirms the reliability and accuracy of the slot characterisation previously done. Since no optimization of the complete model in a full-wave simulator has been done, there is still room for improvement of the antenna performance.

3.7 Acknowledgement

The authors would like to thanks the technical staff of Poly-Grames Research Center for the support and the constant interaction during the fabrication and testing phases of this work.

CHAPTER 4 BEAM STEERING IN BROAD WALL SLOTTED WAVEGUIDE USING I-SHAPED RESONATORS

According to [4], scanning range of the X-band meteorological radar is 24° in elevation. We achieved 14° H-plane beam scanning in Chapter 3 which is not enough for weather radar and it needs some improvement. To do this successfully, a continuous beam scanning concept in slotted waveguide at X-band is proposed. In this configuration, beam scanning is accomplished by rotating two dielectric slabs with periodically printed I-shaped resonators (ISR) inside the waveguide and therefore, varying the phase of the slots excitations. The slot offset and length with the presence of ISR-loaded slabs have been determined in order to achieve a specified distribution tapering and a maximum radiating power. The mechanical rotation of the slabs is facilitated by the possibility of using a controlled motor outside the waveguide in order to isolate the RF fields. The dimensions of the ISRs have been optimized to maximize the range of steering angle. To validate the antenna concept, a non-resonant 20-slot waveguide array with the element spacing of $d = 0.44\lambda_0$ at 9.35 GHz has been designed and fabricated. Good agreement between the simulations and the measurements has been obtained. The antenna scanning range is up to 28 º (14° more than the scanning range achieved in Chapter 3), the sidelobe level is below −15 dB and the overall bandwidth (S_{11} less than -10 dB) is from 9.2 GHz to 9.5 GHz.

4.1 Introduction

Previously in Chapter 3, we have presented a continuous beam steering concept using rotating dielectric slabs inside the slotted waveguide. In this paper, we show that by printing (I-shaped resonators) ISRs on the slabs, the phase-varying effect is augmented, leading to an increased range of beam scanning. The presented design is optimised for an X-band weather radar or low orbit ground station satellite application. As shown in Figure 2.7, it would be required that the cylindrical network elements be able to scan about 30° in elevation.This ISR-loaded slotted waveguide antenna exhibits more scan range with lower side lobes compared to the design presented in [78].

The chapter is organized as follows. Section 4.2 briefly introduces the design methodology of the ISR-loaded phase shifter. Antenna configuration and design are discussed in Section 4.3. In Section 4.4, engineering details on the feeding transition and matched load are presented. Finally, a comparison of experimental and simulation results are provided and discussed in Section 4.5.

4.2 ISR-Loaded phase shifter design

The proposed ISR-loaded waveguide is an extension of the earlier design presented in [99]. The configuration is illustrated in Figure 4.1a. The waveguide is periodically loaded with I-shaped resonators printed on the dielectric slabs. The phase constant of the propagating waveguide modes is changed by rotating the slabs. The axes of rotation are at a height $b_{guide}/2$ from the waveguide bottom wall, and at distances $d_{rotation}$ from the two narrow walls. This phase shifting controls the antenna main beam direction in the H plane. The dimensions and material of the dielectric slab have to be chosen to propagate a single mode at our operation frequency (9.35 GHz). The waveguide considered here is WR62 and the rotating dielectric slabs material are Rogers RT/duroid 6002 ($\varepsilon_r = 2.94$ and $\tan\delta = 0.0012$). To design the phase shifter we used the Eigen-mode solver of HFSS and applied Master-Slave conditions on a single-ISR cell in the waveguide in order to

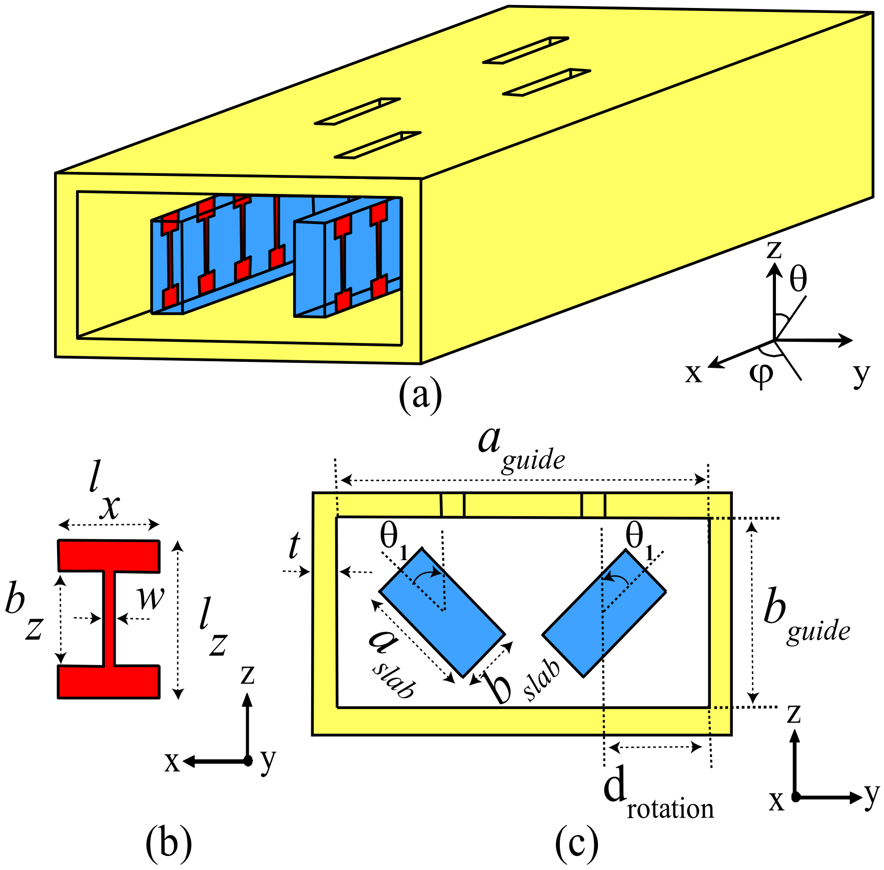

Figure 4.1: ISR-loaded slotted waveguide; (a) 3−D view, (b) front view.

apply a phase delay. The ISR-loaded waveguide and the equivalent circuit are shown in Figure 4.2a. Figure 4.2b shows the dispersion diagram obtained from simulations.

The components associated with the TE_{10} mode in Figure 4.2a are equivalent per-unit-length parameters [100] that predict the propagation and the cut-off frequency of the empty waveguide.

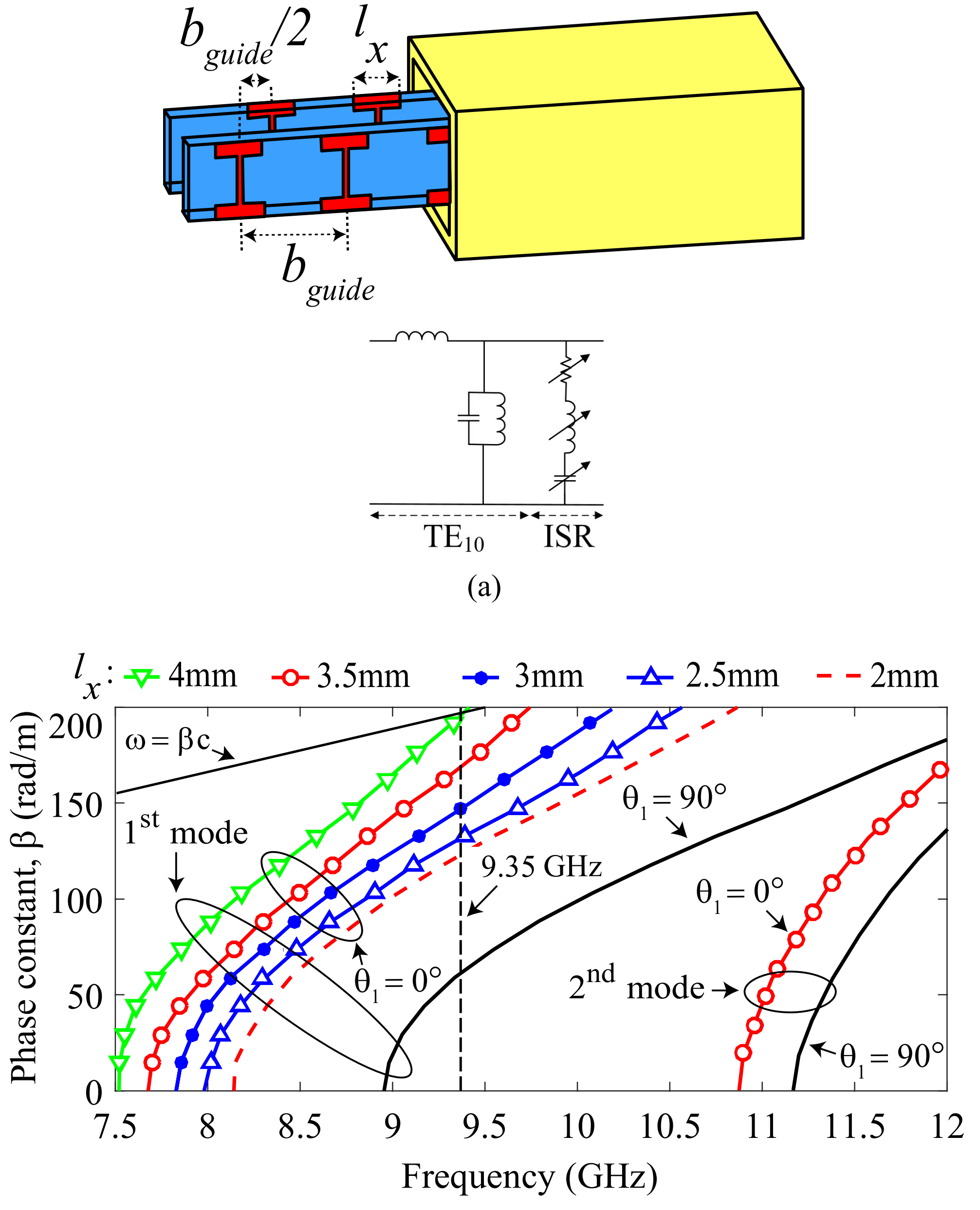

Figure 4.2: (a) Configuration and equivalent transmission line representation of the ISR loaded waveguide for TE_{10} waves and (b) dispersion diagram for the different values of l_x (See Figure 4.1).

The parallel LC branch goes from an inductive behavior below cut-off, to a capacitive behavior above cut-off. The branch containing the tunable elements is associated with the periodically repeated ISRs, and tenability results from the rotation of the dielectric slab. The capacitance is due to the proximity between the broad walls of the waveguide and the ISR segments of length l_x. The ISR vertical segment is introducing an inductive component.

Figure 4.2b is showing the dispersion diagram of the waveguide loaded with the dielectric slab with printed ISRs. Calculations were done with HFSS for various values of the ISR horizontal segment length (l_x) and for $\theta_1 = 0°$ and 90°. When $\theta_1 = 90°$, the ISR is perpendicular to the E field, and therefore l_x has no effect on the dispersion diagram. This is why we shown only one curve at this angle in the figure.

It can be seen in Figure 4.2b that as the value of l_x increases for $\theta_1 = 0°$, the cut-off frequency decreases, which demonstrates the increasing capacitive effect of the series LC branch in the considered frequency band. The segments of length l_z and l_x become respectively parallel to the H field and perpendicular to the E field of the TE_{10} mode, when rotating the dielectric slabs from $\theta_1 = 0°$ to 90° in Figure 4.1b, which makes the effect of the ISR vanish. Therefore, the presence of ISR can reduce the cut-off frequency considerably. When $\theta_1 = 0°$, the E fields in the center of the broad wall of the waveguide become stronger whereas, there is no effect on the E fields when $\theta_1 = 90°$. As illustrated in Figure 4.2b, by increasing the values of l_x from 2 mm to 4 mm, the phase velocity decreases. However, at the design frequency of 9.35 GHz and $l_x = 4$ mm, the phase is near to the slow wave region. Therefore, we have used $l_x = 3.5$ mm in our antenna design to reach the maximum phase variation caused by slab rotation in the fast wave region. Based on the geometrical parameters given in Table 4.1, Figure 4.3 shows the wavenumber variations of the ISR-loaded waveguide when the ISRs are rotating from $\theta_1 = 0°$ to 90°. The second mode is well attenuated at the design frequency of 9.35 GHz and the waveguide is evidently single mode.

4.3 Antenna configuration and design

In order to control the beam, we consider a non-resonant array with the slot spacing smaller than $\lambda_g/2$. The main beam direction of the array factor which is the angle of θ relative to the z axis is given by:

$$\sin\theta = \frac{\beta_g d - \pi}{\beta_0 d} \tag{4.1}$$

Table 4.1. Dielectric Slab and Waveguide Parameters (in mm)

a_{guide}	b_{guide}	a_{slab}	b_{slab}	t	l_x	l_z	b_z	w
15.8	7.9	5	1.5	1.5	3.5	5	3	0.4

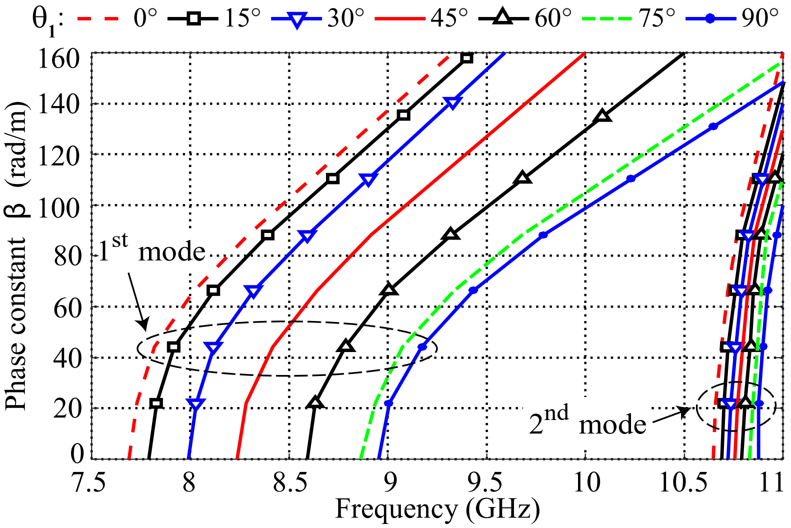

Figure 4.3: Waveguide phase varying for l_x = 3.5 mm and various rotation angles of θ_1.

where β_0 is the propagation constant in free-space, β_g is the guided phase constant and *d* is the slot spacing. The term π radians in the numerator comes from the alternative consecutive slot offsets on opposite sides of the H plane. To reach maximum beam steering at 9.35 GHz, the array factor calculations based on $\beta_g(\theta_1 = 45°)$ = 120 rad/m given in Fig. 3 led to choose the slot spacing of d/λ_g= 0.35. The value of β_g varies from $\beta_g(\theta_1 = 0°)$ = 162 rad/m to $\beta_g(\theta_1 = 90°)$ = 62 rad/m at 9.35 GHz, which gives beam steering from θ = 2° to 33° based on (4.1).

The length (*l*) and offset (*x*) of each slot are controlling the slot admittance. They should be determined such that the specified tapering is achieved. In order to determine the slot admittances we considered a $3\lambda_g/4$ long section of waveguide as illustrated in the inset of Figure 4.4. The design was done for the ISRs angle rotation of θ_1 = 45° which is in the middle of the range of interest. The waveguide is short-circuited at a distance of $\lambda_g/4$ after the slot and the other end is the excited port. It should be noted that the ISRs on the two slabs are offset by a half period (see $b_{guide}/2$ in Figure 4.2a) in the x direction. This offset was used to decrease the effect of ISRs on the E field. The input admittance at the excitation port is the admittance of the slot because the broad wall slot appears as a shunt load. We first need to find the resonant length for each given offset. The full-wave solver of HFSS performing a 3D port analysis was used. We used a parameter sweep simulation in which length l is varied for each x. Since the normalized slot susceptance must be zero at resonance, for a given x, the parameter sweep l returns a set of admittance points which was processed to determine the resonant l.

As in Chapter 3, a triangular amplitude taper for a non-resonant 20-slot ISR-loaded waveguide with 15% of power dissipated in matched load ($r = 0.15$) was used in order to control the side lobe levels. As illustrated in Figure 4.4, two polynomials were derived to give the slot resonant lengths and offsets as a function of conductance.

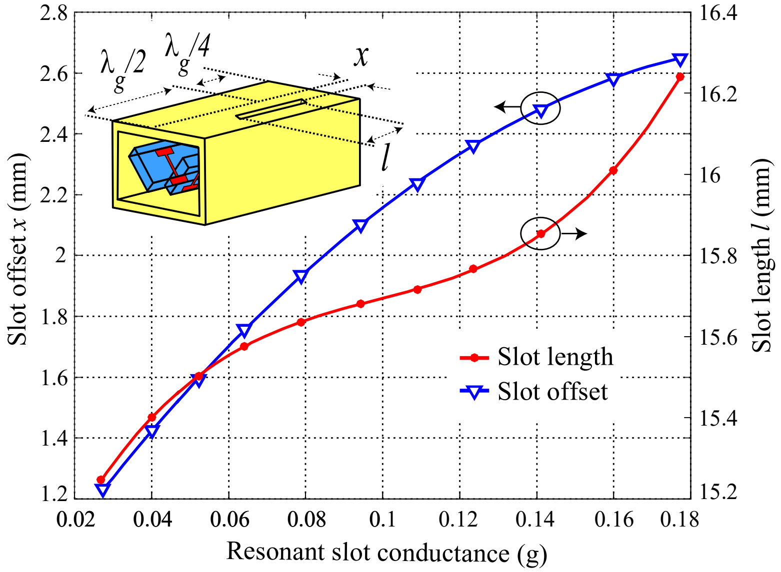

Figure 4.4: Resonant conductance (g) and slot length (l) versus slot offset (x) obtained with curve fitting method for ISRs rotation angle $\theta_1 = 45°$.

4.4 Transitions and matched load design

The chosen operation frequency of 9.35 GHz but the cut-off frequency of the standard WR62 waveguide is 9.49 GHz. Therefore, we used a metallic ridge, as shown in Figure 4.4a, to reduce the cut-off frequency below 9.35 GHz. To feed the antenna, two different transitions expired from

Chapter 3 were designed. The first one was a coaxial to ridge waveguide transition in which the size and the location of the coaxial probe were varied with respect to the shorting wall in order to optimize matching. The second transition, this time from the ridge waveguide to a waveguide loaded with the dielectric slabs and ISRs, was designed. As shown in Figure 4.5, wedge shaped tips on both the ridge and the ISR-loaded dielectric slabs led to good simulated return loss for all rotation angles of θ_1. As shown in Figure 4.5a, a stand made of rohacell was used to support the

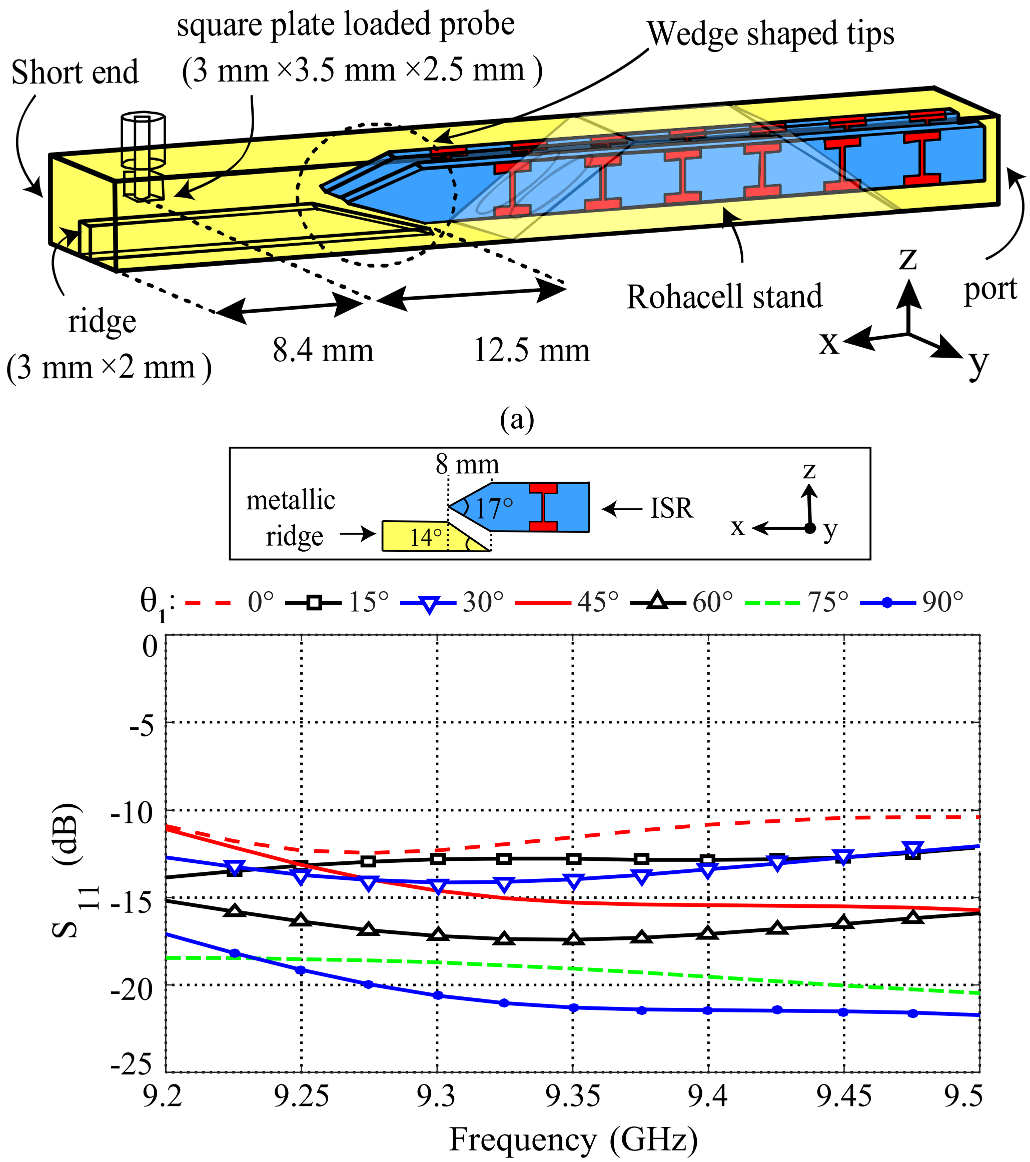

(a)

(b)

Figure 4.5: (a) Coaxial to waveguide transition and (b) wedge shaped tips of the ridge and the slabs (in the inset) and S_{11} of the transition for different values of θ_1.

dielectric slabs inside the waveguide. Figure 4.5b illustrates the return loss of more than 10 dB of the transition for different rotation angles of the slabs.

Based on the method given in Chapter a matched load termination for this non-resonant array was designed to reduce the degradation of the pattern coming from undesirable reflection at the end of the guide. Standard waveguide matched load cannot be realized since our waveguide is loaded with dielectric slabs and ISRs. The absorbing material used here is the same as Chapter 3 but with different dimensions. Figure 4.6 shows the configuration and the simulated return loss of the

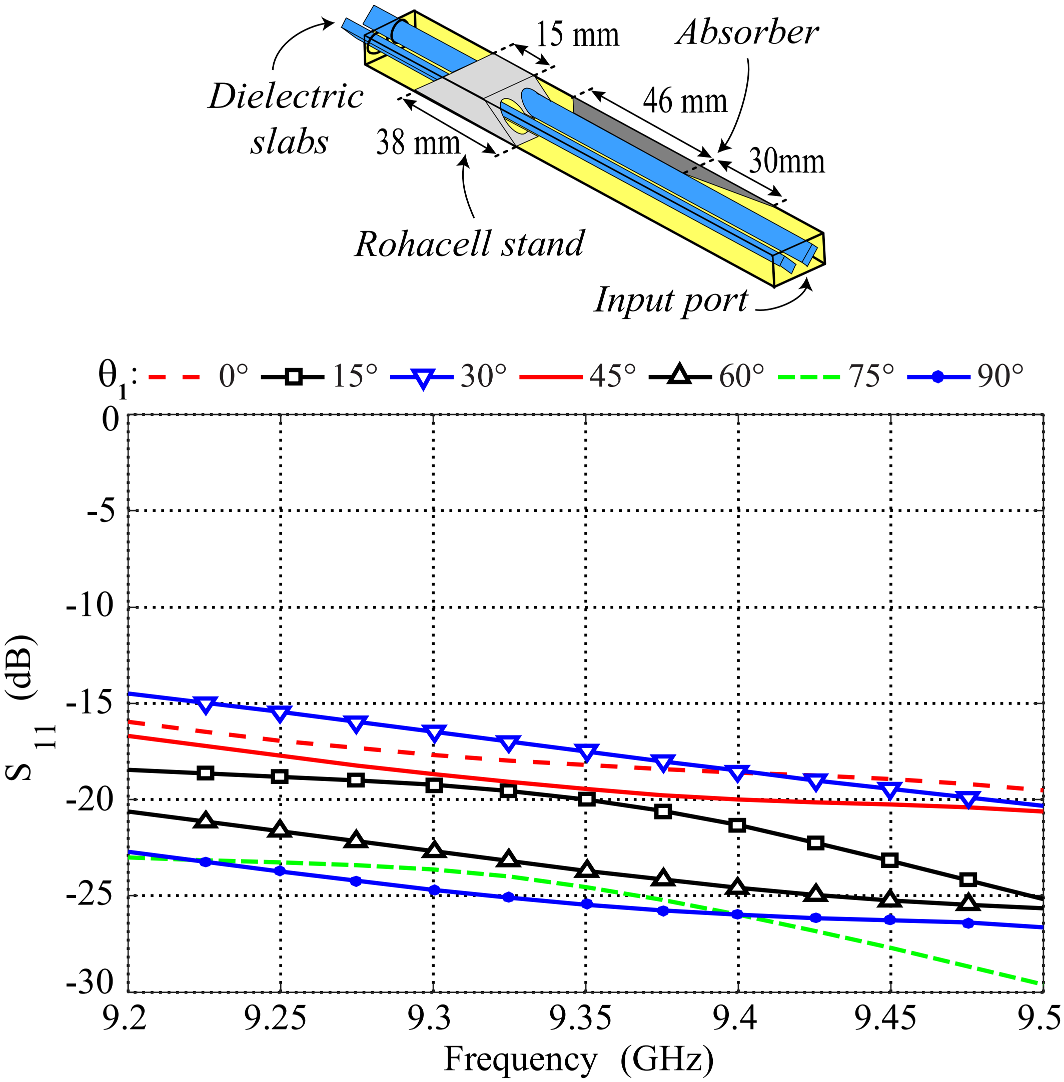

Figure 4.6: Simulated model and S_{11} of the matched load in different rotating angles θ_1 of the ISRs.

matched load. The rotating dielectric slabs are going through the matched load and protrudes outside the end of the guide, as shown in the inset of Figure 4.6. This way, the rotation mechanism (motor, gear, etc.) is not perturbing the RF fields inside the waveguide.

4.5 Experimental and simulation results

An antenna prototype has been fabricated based on the design given in previous sections. The antenna elements (transition, ISR-loaded slotted waveguide and matched load) were optimized for a slabs rotation angle of $\theta_1 = 45°$ and a frequency of 9.35 GHz. All the simulations have been done with HFSS version 19.

The antenna is designed for continuous beam scanning with continuous rotating angle from $\theta_1 = 0°$ to 90° and its performance has been measured for several rotating angles θ_1 with steps of 15°. A 10 dB return loss level is obtained in the 9.2 GHz to 9.5 GHz bandwidth for all configurations, for

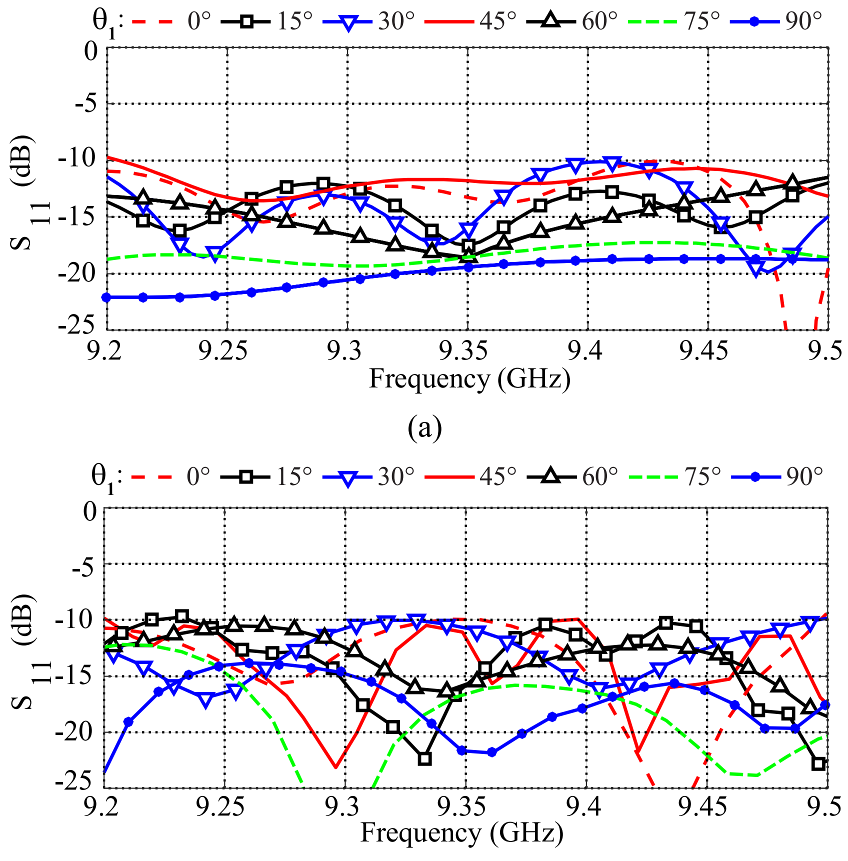

(a)

(b)

Figure 4.7: Reflection coefficients of the antenna for different values of θ_1. (a) Simulation. (b) Measurement.

both simulations and measurements, as shown in Figure 4.7. The simulated and measured scanning performance in the H-plane at the design frequency of 9.35 GHz are illustrated in Fig Figure 4.8.

The antenna has a scanning range of 28º (scanning range of the X-band weather radar is 24° in elevation according to [4]) and the sidelobe level remains at −15 dB between $\theta = -90°$ and 90°. Instead of the monotonically increasing scan loss usually observed in travelling wave antennas when scanning from near broadside towards end-fire, Figure 4.8 shows that the gain increases when the beams scan from 4° ($\theta_1 = 0°$) to 15° ($\theta_1 = 45°$) from broadside. A possible reason for this is the fact that the slots were optimized for the case $\theta_1 = 45°$. For other slab rotation angles they might not be resonant. Consequently, less power will be radiated form the slot and hence more power will be propagated to the terminating load.

Figure 4.9 illustrates the percentage of lost power (dissipated in materials and radiated) $(1 - |S_{11}|^2 - |S_{21}|^2)$ and the radiation efficiency of the antenna. To calculate these S parameters, the matched load at the end of the structure is replaced by a wave-port (i.e. port #2). It should be noted that the efficiency is calculated by the ratio of the realized gain to the directivity.

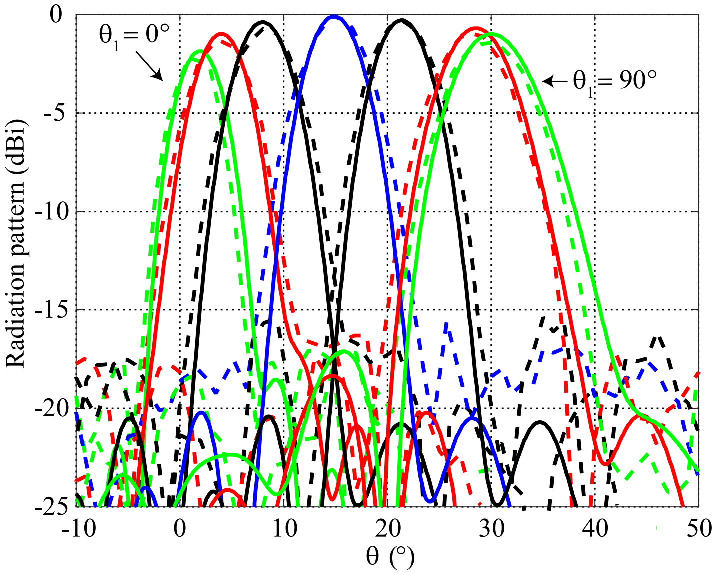

Figure 4.8: H-plane ($\phi = 0$) scanning performance of the antenna at 9.35 GHz. Simulated (solid line) and measured (dashed line) in different rotating angle θ_1 (see the axes presented in Figure 4.1). The step for rotating angle is $\Delta\theta_1 = 15°$.

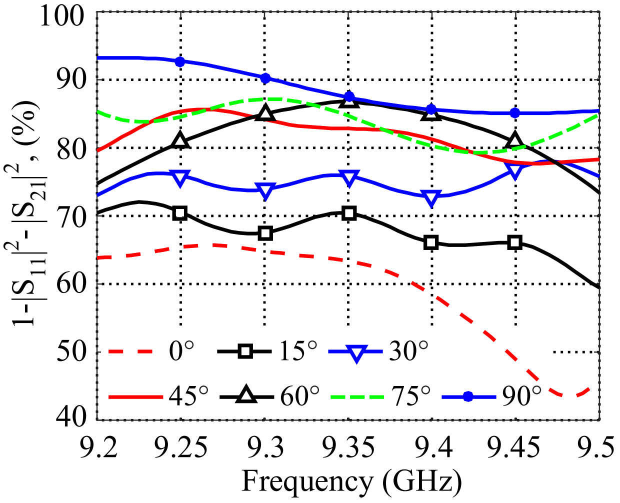

(a)

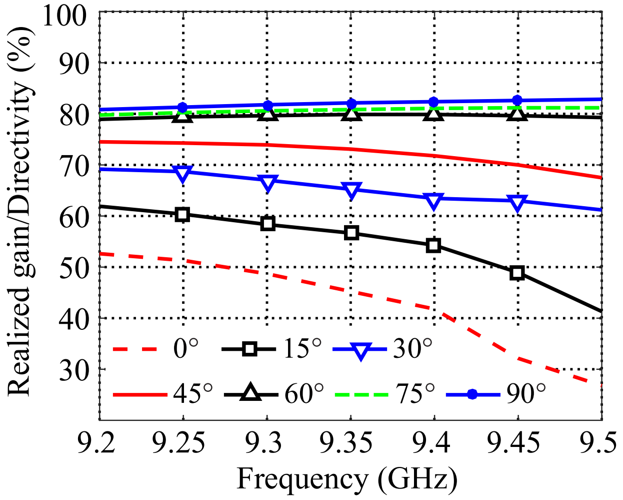

(b)

Figure 4.9: Simulated (a) radiated and dissipated power ($1-|S_{11}|^2-|S_{21}|^2$) and (b) antenna efficiency for various rotation angles of θ_1. The frequencies correspond to the weather radar application.

It therefore includes input return losses, which account for up to 10% (or −10 dB) of the power according to Figure 4.7. Except for slab rotations smaller than 30°, the efficiency is greater than 60% over the whole frequency range. For small slab rotations, the operation is limited to lower frequencies if we want to keep an efficiency of 50% or more. In addition to higher losses in the terminating load, this high loss at small rotation angles is due to ohmic loss in the ISRs, which increases as they become aligned with the E field in the waveguide.

The antenna gain for rotating angle $\theta_1 = 0°$ to 9 0 has been measured by the gain comparison method in the anechoic chamber. This gain is shown in Figure 4.10 along with main beam direction. It should be noted that, in order to have a fan beam in this design there is no directional flare and therefore we have a lower gain of about 5 dB in comparison with the design in Chapter 3. The simulated scanning performance with $\Delta\theta_1 = 5°$ is shown in Figure 4.11. The side lobe levels remain at −15 dB over the scanning range.

In this work, the achieved beam scanning range is more than our previous work [39]. However, the decrement of antenna efficiency at the design frequency is 10% which is due to the presence of

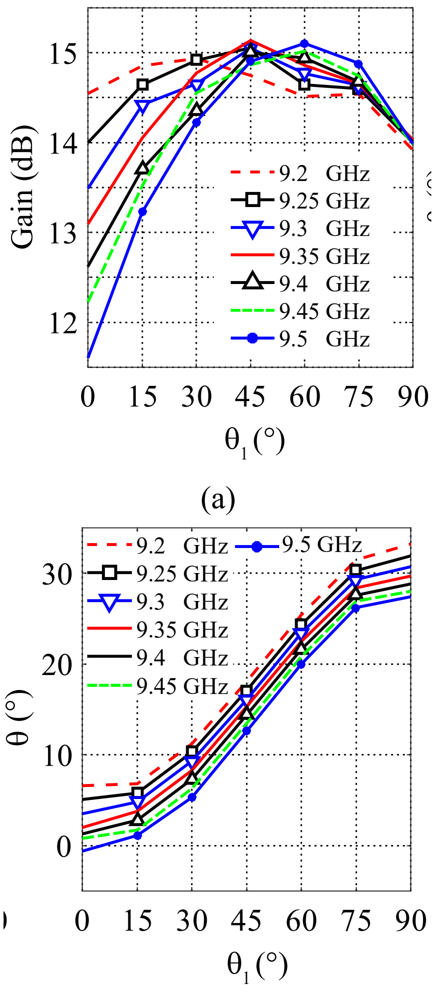

(a)

(b)

Figure 4.10: Measured (a) gain and (b) main beam direction for various ISRs rotation angles of θ_1. The antenna was designed for $\theta_1 = 45°$ at 9.35 GHz.

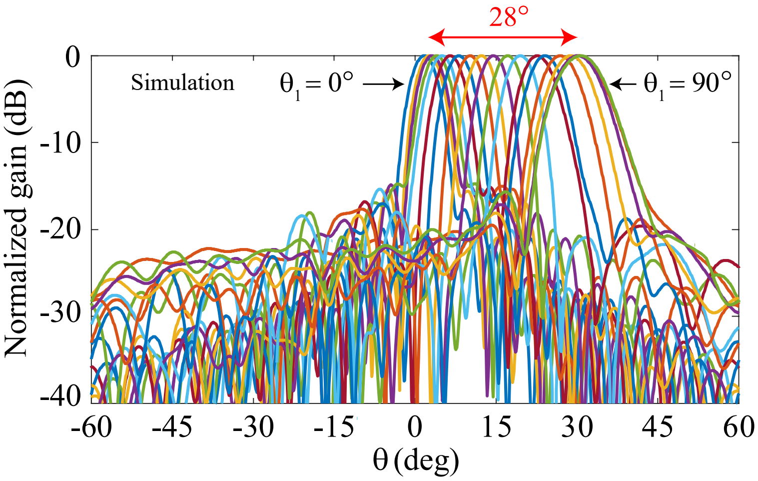

Figure 4.11: H-plane ($\phi = 0$ at 9.35 GHz) normalized patterns of the ISR-loaded broad wall slotted antenna, simulated in different rotating angle θ_1. Scanning range is 28°.

ISRs. Refs. [101-104] present more scanning range compared to this work, but they are based on frequency scanning principle in which a broad bandwidth (around 26%) is required.

4.6 Conclusion

The design of electromechanical continuous beam scanning antenna based on rotating ISRs inside a slotted-waveguide has been presented. The antenna shows a continuous beam scanning of 28º at the design frequency of 9.35 GHz (14° beam scanning range more than the previous Chapter) and overall experimental bandwidth (−10 dB) from 9.2 GHz to 9.5 GHz.

Although the idea of beam scanning capabilities by rotating a ridge in a waveguide was given in [78] and has been optimized in [39], this concept presents more scanning. Therefore, the presented technique is promising for high power continuous beam scanning applications. Although the ISRs were rotated manually to measure the antenna's performance, a simple motor drive could be easily implemented to rotate them electromechanically.

CHAPTER 5 ARTICLE 2: CROSS-POLARIZATION REDUCTION OF A NARROW WALL SLOTTED WAVEGUIDE ARRAY FOR KU-BAND

Amirhossein Ghasemi, Jean-Jacques Laurin

Presented in 2018 at IEEE AP-S/URSI 2018, conference in Boston, USA

5.1 Abstract

A method to reduce cross-polarization (X-pol) of narrow wall slotted waveguide is presented. A 10 inclined slot array cut in the narrow wall of a rectangular waveguide with the element spacing of $d = 0.64\lambda_0$ operating in Ku-band is employed. The proposed slotted waveguide antenna consists of a perforated-metallic plate which acts as a polarization filter. The polarization filter reduces the maximum cross-polarization level by 10 dB at the design frequency of 14 GHz and 5 dB over the frequency band 12 GHz to 18 GHz.

5.2 Introduction

Slotted waveguide antennas have been used in several applications as radar and satellite communications obtaining high-quality performance and are mostly based on inclined slots for circular polarization [105] or longitudinal slots for linear polarization [39].

The slot inclination produces undesired X-pol when the slot is in the narrow wall of the waveguide. Such inclination is essential to control the slot admittance, which is directly related to the radiated power. Cross-polarized component increases strongly as the inclined slot array scanned at an angle away from broadside and produces interference and jamming problems. Various complex methods to decrease X-pol in the narrow wall slotted waveguide have been employed. One of the most effective method to reduce X-pol level is using untilted slots [106]. However, the fields inside the waveguide should be changed in order to excite the slots. In [107], to produce such a field distribution, the angled ridges were used under the untilted slots. Another way to avoid inclined slot in the narrow wall is using two small insets milled within the waveguide at opposite sides of the untilted edge slot [108]. However, the alternative solutions presented in [106-108] are costly and complicated to fabricate.

More recently in [109], a simpler alternative to excite untilted slots in the narrow wall was proposed. This new radiating structure basically consists of an untilted slot excited through the perturbation produced by a tilted parasitic dipole [109]. This dipole is etched on dielectric substrate and located within the waveguide, parallel to the narrow wall, and at a given distance from the slot. The inclination angle of the dipole controls the amount of power coupled to the slot. A possible drawback of this procedure is that it cannot handle high power.

The proposed design allows X-pol reduction of the inclined slotted waveguide with less complexity by using a polarization filter. This filter has less effect on the return loss and the efficiency of the antenna, and allows high power handling.

5.3 Design of the Filtered Antenna

The configuration of the inclined slotted filtered waveguide and the optimized model are shown in Figure 5.1a and Figure 5.1b respectively. Here, we employ a WR-62 (15.8 mm × 7.9 mm) with 1.6 mm thickness of rectangular waveguide. The antenna was originally designed for pattern diversity and is capable to produce broadside or near broadside patterns depending on the phase difference of the excitations. In order to highlight the effect of the polarization filter, we considered a uniform non-resonant 10-slot array with an off-broadside main beam. For that case, the element spacing is $\lambda_g/2.1$ at the design frequency of 14 GHz so the reflections from different slots do not

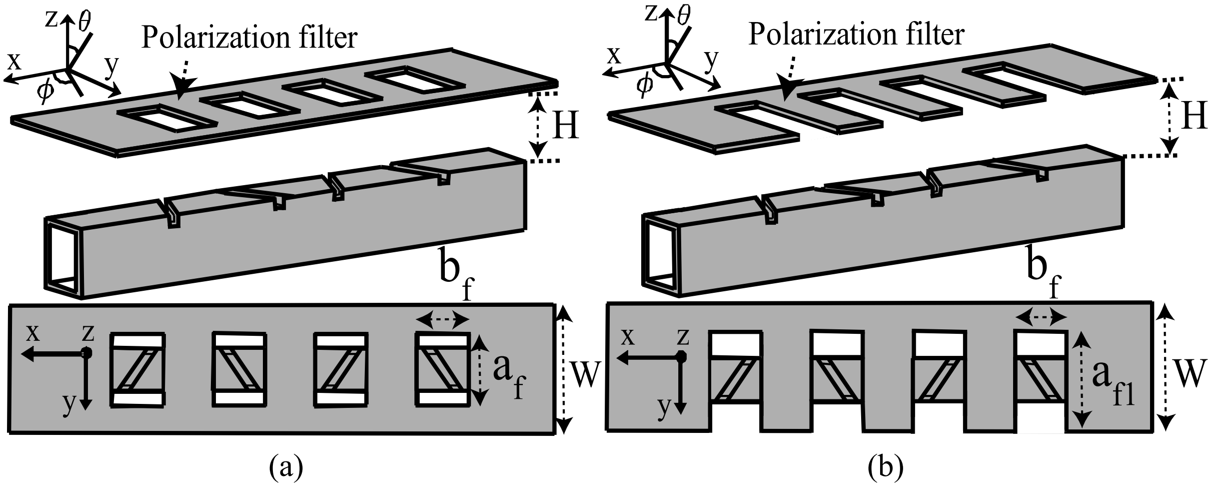

(a) (b)

Figure 5.1: (a) Simulation model of the slotted waveguide and the polarization filter, the parameters are H = 22 mm, W = 32 mm, b_f = 9 mm and a_f = 18 and (b) optimized polarization filter model with a_{f1} = 25 mm.

add up in phase at the input of the waveguide and the return loss will be small and the main beam will be steered near broadside ($\theta = -3^\circ$). Each slot has common width of 1.7 mm, cut depth of 1.6 mm and inclined angle of 25° for resonance. A perforated rectangular metallic plate (polarization filter) is located parallel to the narrow wall with the dimensions specified in Figure 5.1. Matched ports were considered at both ends of the waveguide.

For the purpose of X-pol reduction, one should note that the field component in the plane $\phi = 90^\circ$ (yz plane) must be minimized. In order to reach the best X-pol over the design frequency band, we optimized the lateral size (a_{f1} and b_f) of the perforated -rectangular plate as well as the distance between the filter and the waveguide (H) using the 3D full-wave solver of Ansys-HFSS.

5.4 Simulation Results and Discussion

The simulation results of the analysis of the waveguide antenna are presented in this section. This was accomplished by running the full wave analysis of HFSS. Figure 5.2 shows the normalized

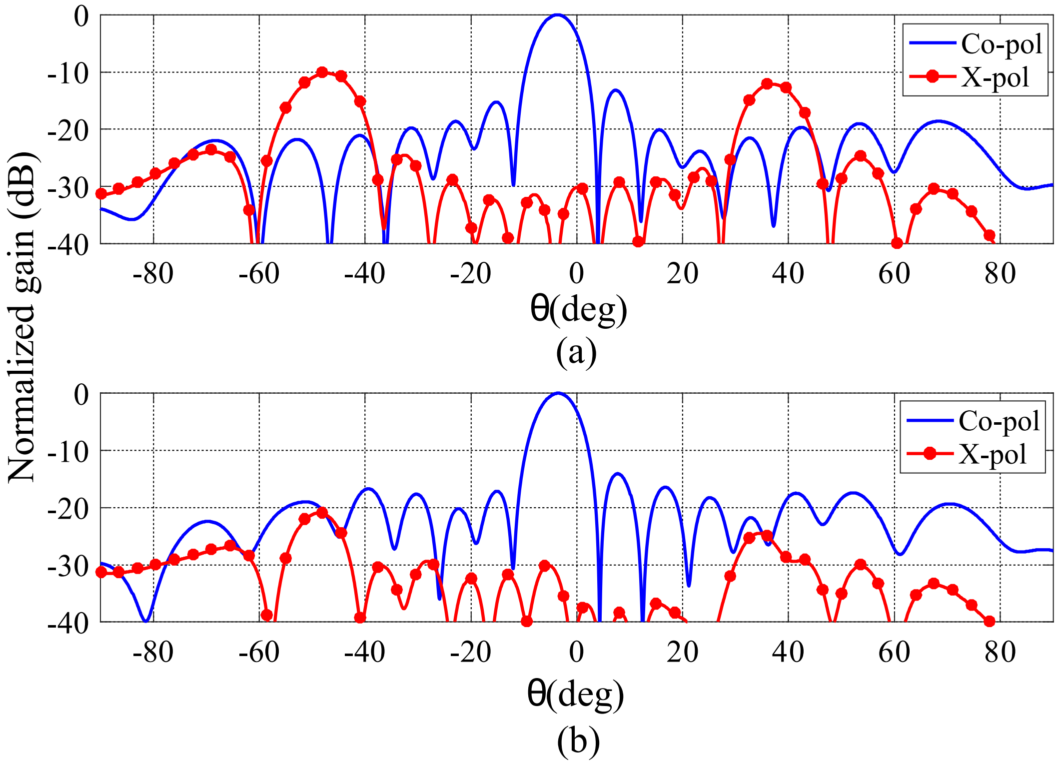

Figure 5.2: Normalized radiation pattern of (a) without filter and (b) with optimized-filter of the inclined slot waveguide at the design frequency of 14 GHz, $\phi = 0$ (see the axes presented in Figure 5.1).

radiation pattern of the optimized-filter and non-filtered waveguide antenna. It can be observed that the polarization filter reduces the maximum X-pol level by 10 dB at the design frequency of 14 GHz. Since the array is non-resonant, the main beam is 3° off-broadside.

Figure 5.3 shows the maximum X-pol level and peak gain of the antenna with and without the polarization filter. The filter reduces the maximum X-pol level from -4.5 dB to -14.5 dB at the design frequency of 14 GHz and down to 5 dB throughout the frequency band.

As illustrated in Figure 5.3b, the gain reduction of the filtered antenna is 3.77 dB at 14 GHz which goes up to 1.5 dB by using the optimized filter (a_{fl} = 25 mm). However, the polarization filter has less effect on the S_{11} and the efficiency (directivity/gain) of the antenna as shown in Figure 5.4.

5.5 Conclusion

A new concept of X-pol reduction of an inclined slotted waveguide antenna with less fabrication complexity compared to [106-108] has been presented. We have demonstrated the decrease of X-pol as the effect of polarization filter on the field component in the plane $\phi = 90^{\circ}$ (yz plane) of the antenna. The modelled filtered antenna is able to present a 10 dB X-pol reduction at the design frequency and a 5 dB reduction over the frequency band. Moreover, within the bandwidth of 12-18 GHz, the input match is better than -18 dB.

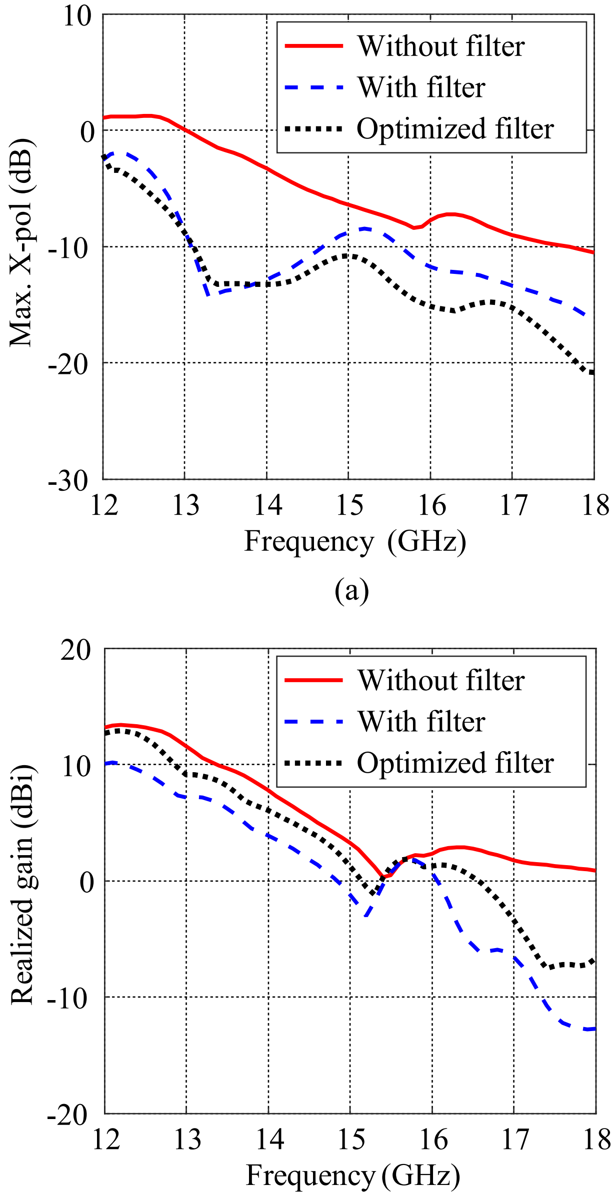

(a)

(b)

Figure 5.3: Maximum cross-polarization level and (b) peak gain of the antenna in the range of -90°< θ <90° and $\phi = 0$.

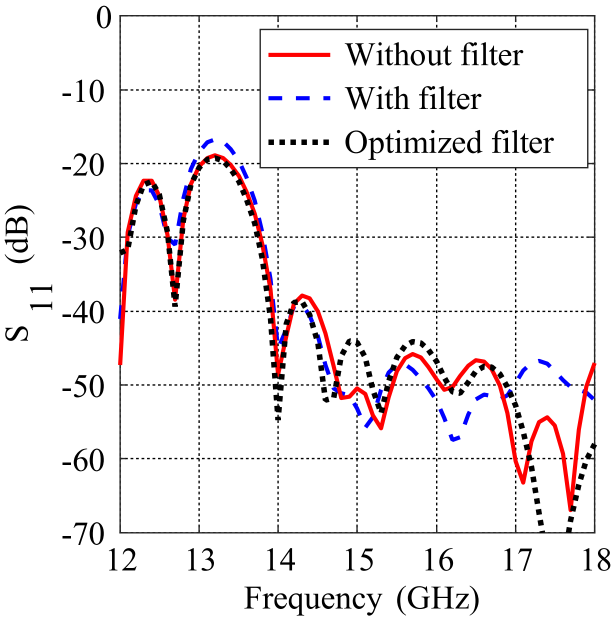

(a)

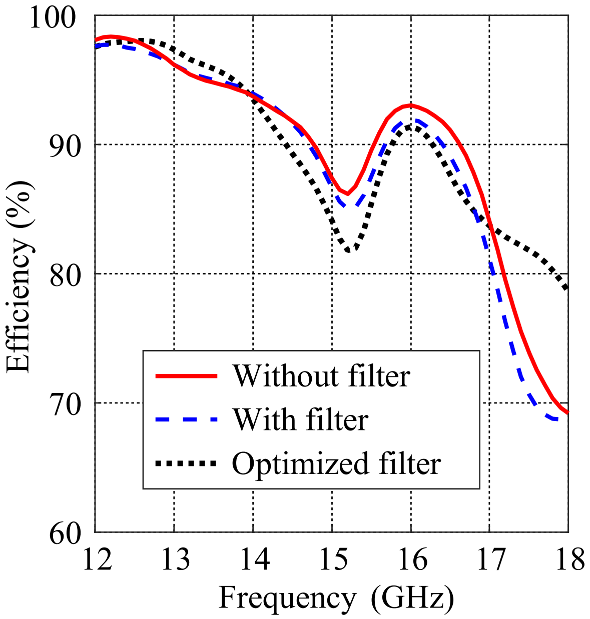

(b)

Figure 5.4: (a) S_{11} and (b) efficiency (directivity/gain) of the antenna.

CHAPTER 6 ARTICLE 3: BEAM STEERING IN NARROW WALL SLOTTED RIDGE WAVEGUIDE ANTENNA USING A ROTATING DIELECTRIC SLAB

Amirhossein Ghasemi, Jean-Jacques Laurin

Published in 2018 in the IEEE Antennas and Wireless Propagation Letters

6.1 Abstract

A beam steering technique in narrow wall slotted ridge waveguide at X-band is proposed. An array of inclined slots cut in the narrow wall of a rectangular ridge waveguide is employed. Beam steering is achieved by rotating a dielectric slab inside the waveguide. The change of wavelength at different rotation angles of the slab is used as the phase shifter. In order to confirm the usefulness of this method, a short non-resonant 20-slot waveguide array antenna with an element spacing of $d = 0.44\lambda_0$ has been designed, built and tested. It is shown that the main beam can be steered from near broadside ($\theta = 6^o$) toward end-fire ($\theta = 42^o$) by rotating the dielectric slab by 90^o. A directivity variation of 2.8 dB and a half-power beamwidth increase of 3^o are observed over this scan at the design frequency. The gain varies from 11.17 dB to 12.47 dB over the scanning range. Due to the relatively short length of the prototype, losses in the terminating load have limited the radiation efficiency to values between 43% and 86%. The E-plane radiation patterns measured at the operation frequency of 9.35 GHz and compared very well with the simulated results.

6.2 Introduction

Beam steering plays an essential role in many wireless applications including communication, radar, imaging and instrumentation. Mechanical beam steering systems using motors and gear arrangements to physically rotate and/or elevate the antenna are used for high power handling. Large antenna systems cannot be mechanically scanned rapidly, and because of this, the design of fixed antennas in which small parts moved [83] and [87] electromechanically have been developed. In [110], beam steering was accomplished by moving in or out, or deforming the narrow wall of a rectangular slotted waveguide. However, the realization of accurate and rapid linear motion of the narrow wall is difficult to achieve. The concept of beam steering capabilities realized by rotating a metallic ridge inside a slotted metal waveguide was proposed in [78]. This antenna suffered from separating the different modes of propagation (i.e. TEM) at the operation frequency.

Frequency scanning antennas based on leaky-wave slot-arrays ([100] and 102]) may offer a simple and low-cost solution compared to phased arrays. However, the frequency band required to scan the main beam over a wide angle can exceed the narrow bandwidths generally allocated to certain applications such as X-band weather radars.

In this paper, we present an electromechanical slotted ridge waveguide antenna in which beam scanning is achieved by rotating a lightweight dielectric slab in order to change the wavelength of the travelling wave. The proposed concept is an extension of the earlier design of a waveguide phase shifter presented in [95]. This slotted ridge waveguide antenna exhibits more scan range with lower side lobes compared to the design presented in [78] and [110].

The paper is organized as follows. Section II briefly introduces the design methodology of the narrow wall slotted ridge waveguide antenna. In Section III, engineering details on the feeding transition, matched load and polarization filter are presented. Finally, a comparison of experimental and simulation results are provided and discussed in Section IV.

6.3 Antenna Configuration and Design

As noted, beam steering in the ridge slotted waveguide is achieved by controlling the propagation constant via rotating a dielectric slab inside the waveguide. The configuration is shown in Figure 6.1. The dimensions of the dielectric slab and waveguide have to be chosen in order to propagate a single mode at the desired operational frequency. Here, we start with a WR-62 modified by adding a metal ridge and the dielectric slab in order to enable scanning at the weather radar application at 9.35 GHz. The effect of the ridge is to increase the range of single mode operation. The dielectric rotating slab is made of Rogers RT/duroid 6010 ($\varepsilon_r = 10.2$ and $\tan\delta = 0.0023$) material. All the dimensions of the waveguide cross section are given in Table 6.1.

A polarization filter located near the slotted wall of the waveguide to reduce the cross-polarization is implemented (see Figure 6.1). This filter inspired from [111] has rectangular aperture with $a_{filter} > \lambda_0/2$ and $b_{filter} < \lambda_0/2$. By analogy with rectangular waveguides theory, this aperture would allow propagation of the TE_{10} mode, with x-polarized E-field, but would be cutoff for the y-polarized TE_{01} mode. The dimensions (a_{filter}, b_{filter} and w_{filter}) and position (h_{filter}) of the

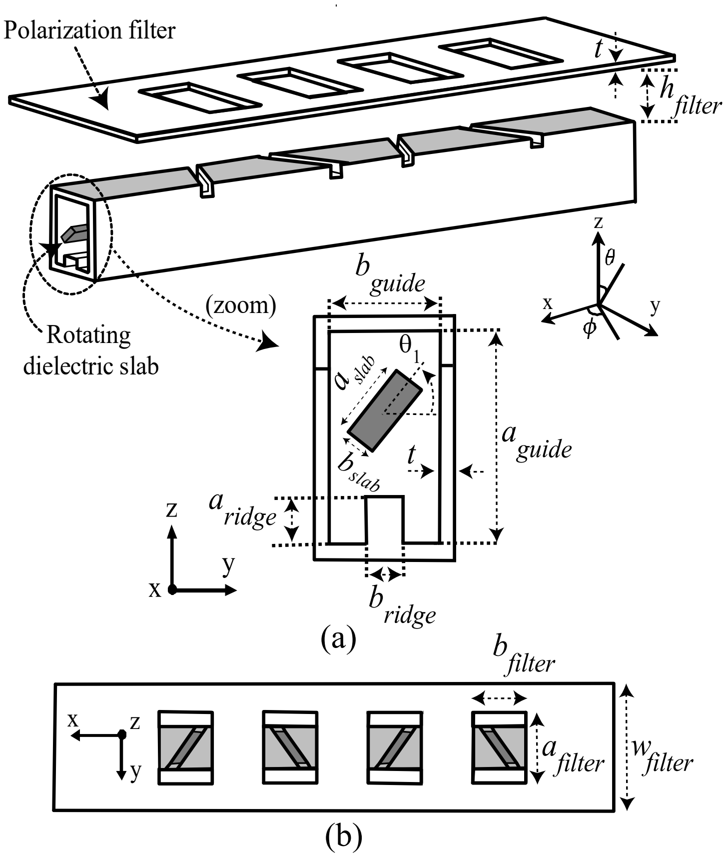

Figure 6.1: Antenna concept; (a) 3-D view, (b) top view.

Table 6.1: Dielectric Slab and Waveguide Parameters (in mm)

a_{guide}	b_{guide}	a_{slab}	b_{slab}	t	a_{ridge}	b_{ridge}	a_{filter}	b_{filter}	w_{filter}	h_{filter}
15.8	7.9	5	2.5	1.5	3.5	3	18	11	32	12

polarization filter shown in Figure 6.1 were chosen to ensure minimum cross-polarization level by minimizing the field component in the plane $\phi = 90°$ (yz plane) at 9.35 GHz. The slab is made of dielectric instead of metal (as in [78]) in order to avoid the TEM mode.

Figure 6.2 shows the propagation constant of the loaded guide versus frequency for the dielectric slab in three different values of the rotation angle θ_1 defined in Figure 6.1a. The highest cut-off frequency of the dielectric-loaded ridge waveguide, occurring at $\theta_1 = 90°$ is 8.75 GHz. In comparison, the cut-off frequencies are 10 GHz and 9.49 GHz for the WR-62 waveguide,

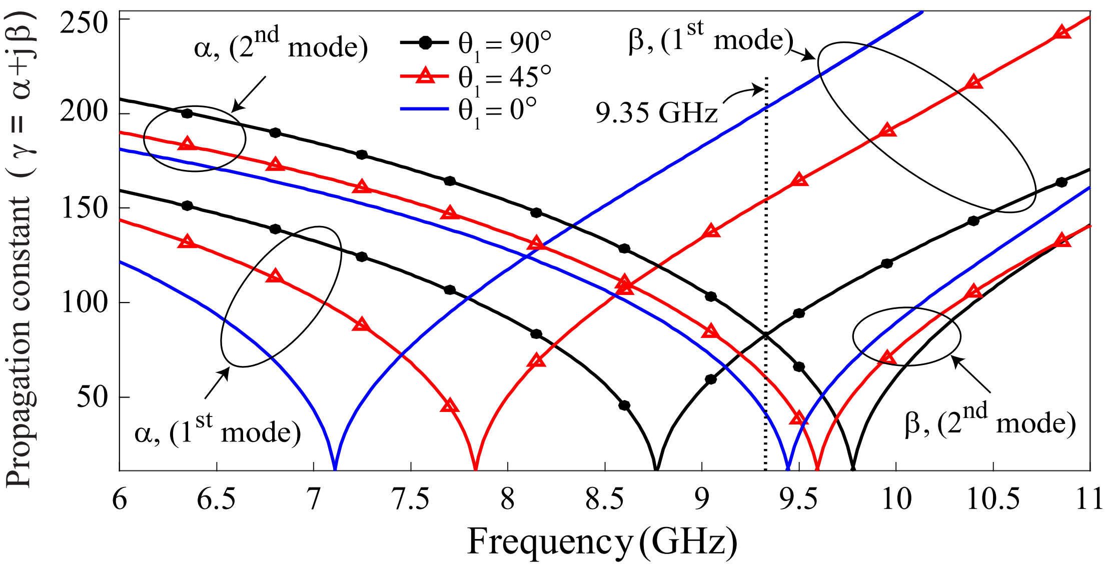

Figure 6.2: Propagation constant for the different rotating angle θ_1.

respectively with and without ridge. These propagation constants were obtained with the full-wave solver of Ansys-HFSS performing a 2D port analysis. The figure confirms that the guide operates in single-mode around the design frequency, while allowing large variations of β.

6.3.1 Parameter Evaluation for Radiating Elements

The inclination (I) and depth (d) of each slot needs to be determined such that a specified tapering and a low return loss level are achieved. To do this, we consider a $3\lambda_g/4$ long section of ridge waveguide with the dielectric slab rotated at 45º (In principle the optimal values of I and d depend on angle θ_1 but in practice, the optimization was done for 45°, which is in the middle of the θ_1 range of interest). An inclined slot is cut in the narrow wall of the waveguide.

A short circuit is placed at the end of the guide, at a distance of $\lambda_g/4$ after the slot, and the excitation wave port is placed at the other end. Here λ_g is the guided wavelength for $\theta_1 = 45°$. Since the narrow wall slot appears as a shunt load in a waveguide, the input admittance at the excitation port is equal to the admittance of the slot. For each slot, we need to find the resonant inclination (I_r) for each given slot depth (d_n).

We used a parameter sweep in HFSS 3D driven mode simulations, in which angle I is varied for each d_n. The normalized susceptance (b) of the slot must be zero at resonance. For a given d_n, the parameter sweep I returns a set of admittance points that was processed in order to determine I_r

(i.e. corresponding to zero susceptance). An interpolation routine was then implemented to generate a contour corresponding to the resonant condition in the inclination-depth plane. At the end of this process, two polynomials were derived to give the slot resonant depth (d_r) and I_r versus required resonant slot conductance as illustrated in Figure 6.3.

A non-resonant array is used in order to scan the beam off-broadside. Thus, the element spacing differs from $\lambda_g/2$ and the reflections from the different elements do not add up in phase at the input port. Hence the reflection coefficient is small [39]. The main advantage of a non-resonant array is a larger bandwidth in terms of sidelobe level and input matching, which makes it suitable for performing as a beam scanning antenna [96]. In the non-resonant slotted waveguide antenna, the slot spacing should be chosen in order to produce the main beam at almost any arbitrary angle θ relative to the axis perpendicular to the array. If slots on the narrow wall are alternately inclined on opposite directions, then the array factor is given by [97]:

$$AF = \sum_{n=1}^{N} a_n e^{[jn(\beta_0 p \sin\theta - \beta_g p + \pi)]} \tag{6.1}$$

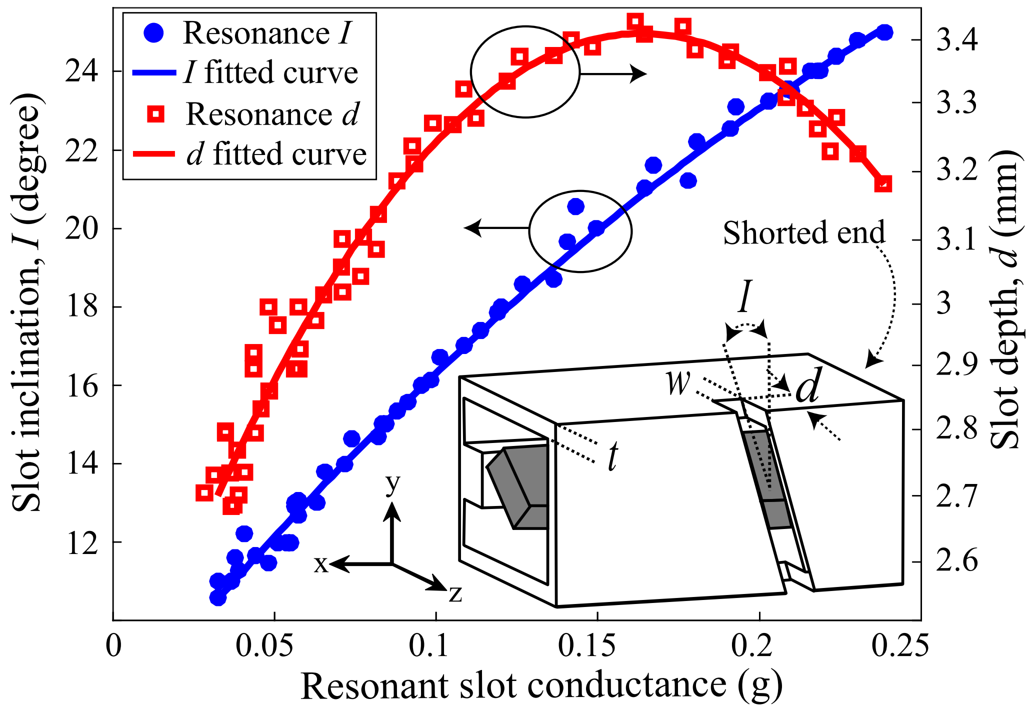

Figure 6.3: Slot inclination (I) and slot depth (d) versus conductance (Re(Y/Y_0)) obtained with curve fitting method ($w = t = 1.5$ mm).

where a_n is the slot excitation amplitude level, p is slot spacing, β_g is the guided wavenumber and β_0 is the propagation constant in free-space. In order to reach maximum beam deviation at the design frequency of 9.35 GHz, the array factor calculations based on the β_g values given in Figure 6.2 in which β_g ($\theta_1 = 45°$) = 151.7 rad/m, led to choose the element spacing of p/λ_g ($\theta_1 = 45°$) = 0.38. The wavenumber variation observed from Figure 6.2 at the design frequency of 9.35 GHz is 122.5 rad/m by rotating the dielectric slab from $\theta_1 = 0°$ to 90° which gives 37º of beam scanning based on (6.1). In order to control the SLL, a triangular amplitude taper for a 20-slot waveguide was used.

Let r be the fraction of the incident power to be dissipated in the match load. Assuming a 1-watt power input and a lossless waveguide, we must have $r + \sum_{n=1}^{N} P_n = 1$ where P_n is the radiated power by the n$^{\text{th}}$ slot. According to the non-resonant array design method presented in [97] we have

$$g_n = \frac{P_n}{r+\sum_{i=n}^{N} P_i} = \frac{P_n}{1-\sum_{i=1}^{n-1} P_i} \tag{6.2}$$

Table 6.2 summarizes the values of distribution amplitude (a_n), radiated power (P_n) and normalized conductance (g_n) for the triangular taper excitation of a 20-element array, with r = 0.15, used in the fabricated prototype.

6.3.2 Feeding and Matched Load Design

Rotating the dielectric slab from $\theta_1 = 0°$ to 90° to steer the antenna beam is causing a large change in the characteristic impedance of the guided wave. In order to maintain a low level of return loss for all slab rotation angles, a transition section acting as an impedance transformer had to be introduced (see Figure 6.4a), and the cross section of this transition had to be designed. Obviously, a dielectric rod with circular cross section would have a constant impedance for all rotation angles. The goal of this transition section is therefore to go from a high aspect ratio slab ($a_{slab} / b_{slab} = 2$), with high impedance variation, to a lower aspect ratio geometry.

The characteristic impedance ratio of the dielectric loaded ridge waveguide and the impedance transformer section for $\theta_1 = 0°$ and 90° is shown in Figure 6.4b. Values of Z_0 were obtained using the port analysis capability of HFSS. It can be seen that Z_0 ($\theta_1 = 90°$)/ Z_0 ($\theta_1 = 0$) = 1.85 for the dielectric loaded ridge waveguide at the design frequency of 9.35 GHz. The proposed impedance transformer reduces this ratio down to 1.23 at 9.35 GHz as seen in Figure 6.4b.

Table 6.2: Slot current distribution (a_n), conductance (g_n), inclination (I_n) and depth (*d)* for the 20-slot array design using triangular amplitude distribution

n	a_n	g_n	I_n (degree)	d_n (mm)
1	3	0.006	8.03	2.37
2	4	0.011	8.51	2.43
3	5	0.017	9.09	2.51
4	6	0.025	9.85	2.61
5	7	0.034	10.69	2.71
6	8	0.046	11.78	2.84
7	9	0.061	14.78	2.98
8	10	0.081	15.77	3.14
9	11	0.106	16.77	3.29
10	12	0.142	19.39	3.41
11	12	0.165	20.93	3.43
12	11	0.166	21	3.43
13	10	0.165	20.93	3.43
14	9	0.160	20.61	3.43
15	8	0.150	19.94	3.42
16	7	0.135	18.9	3.4
17	6	0.115	17.45	3.33
18	5	0.090	15.51	3.2
19	4	0.063	13.27	3
20	3	0.038	11.05	2.76

Feeding the loaded ridge waveguide with low return loss can be achieved with magnetic coupling. In order to realize a coupling loop perpendicular to the H plane, a copper square plate is connected from the end of a horizontal probe to the broad wall of the waveguide (Figure 6.4a). The size of the copper square plate and its location respect to the shorted-end wall of the waveguide were varied using parameter sweep of HFSS 3D simulation to optimise matching. As shown in Figure 6.4c, return loss of more than 15 dB was achieved at the design frequency, and is above 10 dB for a broad range of frequencies, and for three rotation angles of the slab.

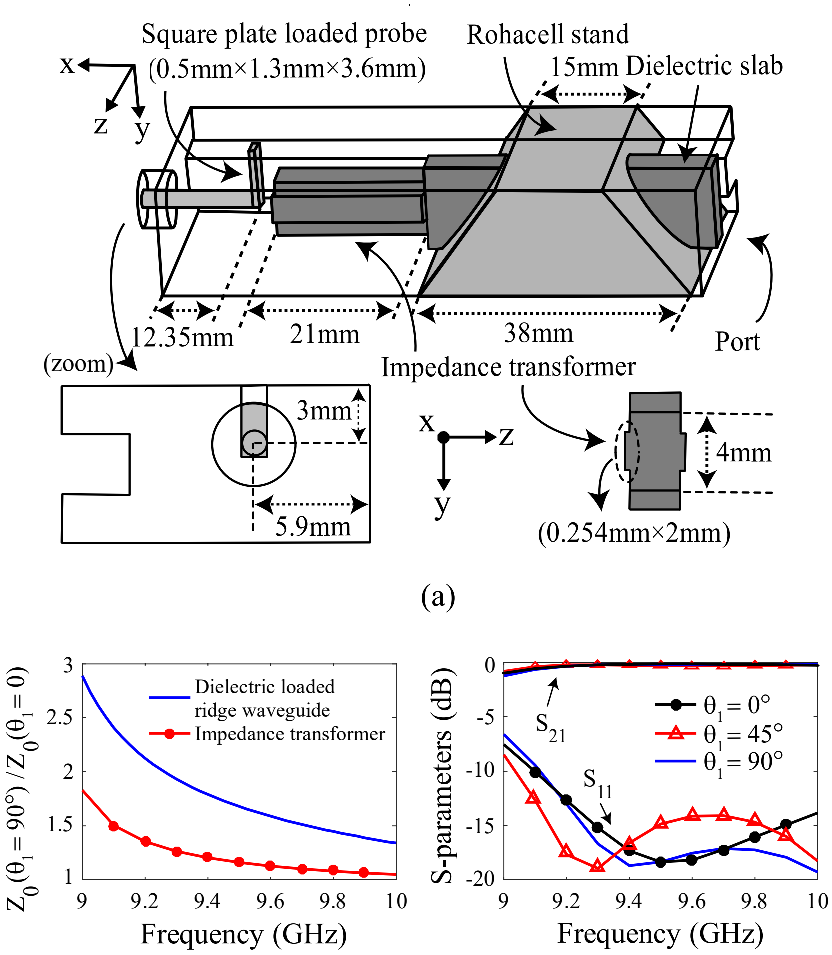

(b) (c)

Figure 6.4: (a) Simulated model, (b) characteristic impedance of the dielectric loaded ridge waveguide and the impedance transformer and (c) S-parameters of the coaxial to ridge waveguide feeding transition.

A matched load termination is necessary for the non-resonant slotted waveguide array in order to reduce undesirable reflection causing degradation of the antenna pattern. For our non-standard waveguide, this load was implemented with the DD-10214 Silicon from ARC Technologies Inc, with $\varepsilon = (17 - 0.2j)\varepsilon_0$ and $\mu = (1.6 - 1.8j)\mu_0$ at 9.35 GHz. A 0.76-mm thick absorber strip was placed on the narrow wall of the waveguide. A rohacell stand was used to support the dielectric slab, as illustrated in Figure 6.5.a. As shown in this figure, the dielectric slab is protruding outside the waveguide, in order to apply rotation. Simulated return loss of more than 20 dB was achieved over a wide frequency band, for the three rotation angles of the slab (See Figure 6.5). The antenna prototype is illustrated in Figure 6.5.b.

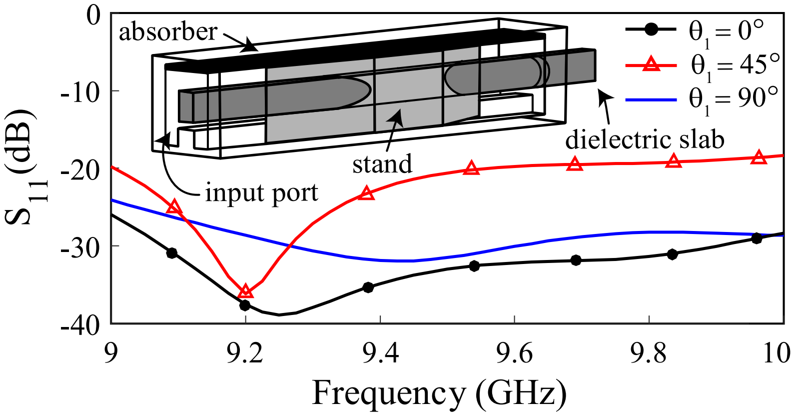

(a)

(b)

Figure 6.5: Simulated model and S_{11} of the matched load, (b) antenna prototype.

6.4 Experimental and Simulated Results

A 20-slot waveguide antenna prototype has been built according to the detailed design given in previous section. As illustrated in the inset of Figure 6.5a, the dielectric slab protrudes outside the waveguide at the end of the matched load, where it can be rotated manually. A simple motor drive isolated from the RF fields (i.e. located outside the waveguide) could be easily implemented. All the elements forming the antenna (feed, transition section, ridge waveguide, slot elements, matched load and polarization filter) were optimized for a slab rotation angle of $\theta_1 = 45°$ and a frequency of 9.35 GHz. Figure 6.6a shows that the return loss is greater than 10 dB for the three rotation states at 9.35 GHz and within a 200 MHz band typically allocated to weather radars. A better waveguide transition would be needed to diminish S_{11} at the lower frequencies (see Figure 6.4c).

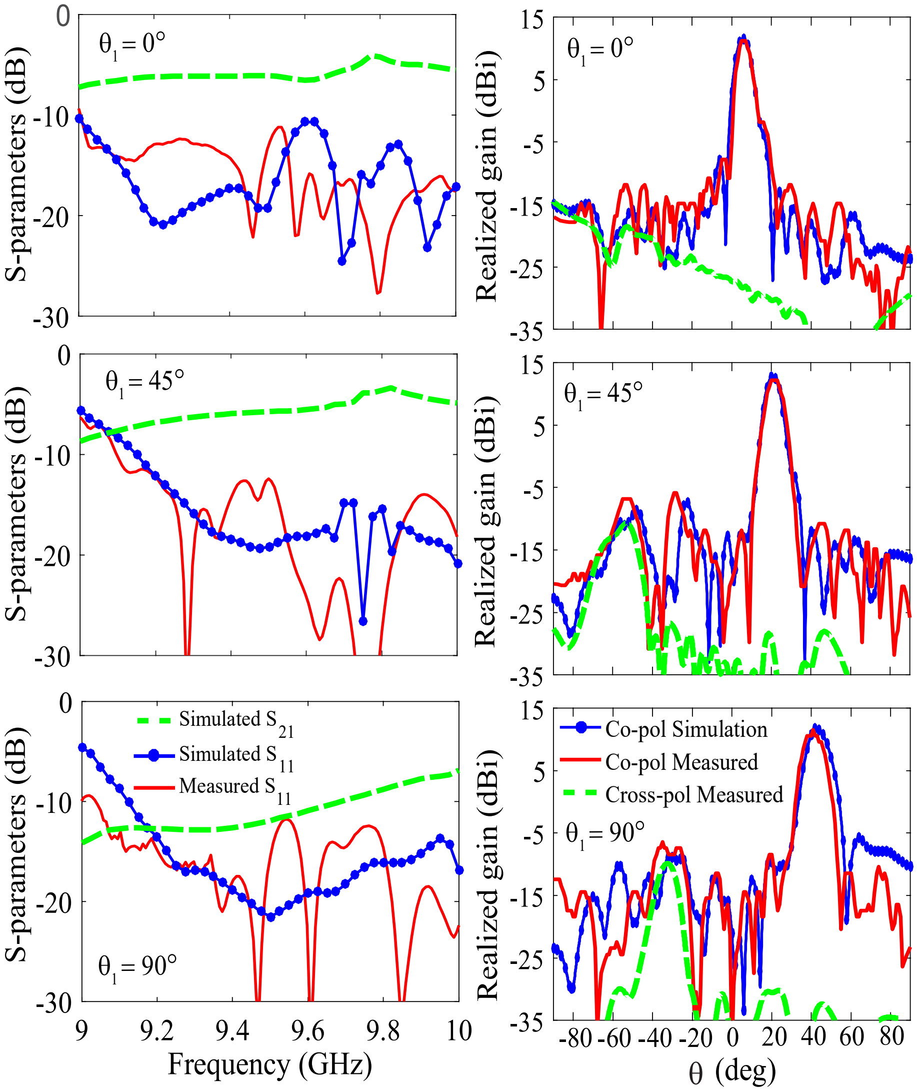

(a) (b)

Figure 6.6: (a) S-parameters and (b) E-plane ($\phi = 0$ at 9.35 GHz) radiation patterns of the antenna, simulated and measured in different rotating angle θ_1 (see the axes presented in Figure 6.1).

E-plane patterns measured in an anechoic chamber at 9.35 GHz are presented in Figure 6.6b. They show a beam steering angle of 6° to 42° from near broadside by rotating the dielectric form $\theta_1 = 0°$ to 90°. The simulated and measured patterns shown in Figure 6.6.b are in good agreement and the SLL remain lower than −18 dB for all the considered slab rotation angles.

The simulated realized gain and directivity at 9.35 GHz and for $\theta_1 = 45°$ are 12.64 dB and 14.78 dB, respectively which gives an overall antenna efficiency of 61%. Return loss ($S_{11} = -17.7$ dB) and losses in the terminating load ($S_{21} = -6.1$ dB according to Figure 6.6.a), represents 26.2% of power. Therefore 12.8% of the incident power is dissipated in metallic and dielectric materials. Losses in the terminating load are high in this short experimental prototype but they would decrease as the array length increases.

The measured cross-polarization levels at E-plane have been included in Figure 6.6b. They remain 29 dB below the co-polarization level in the main beam direction. Table 6.3 summarizes the simulated and measured radiation performance of the antenna in various rotation angles of the slab.

The simulated and measured scanning performance in the antenna E-plane for several frequencies is shown in Figure 6.7 and Figure 6.8. At the design frequency, gain, directivity, beam direction and beamwidth variations of 1.3 dB, 2.8 dB, 36° and 3° are respectively observed.

Table 6.3: E-plane Radiation performance of the antenna at 9.35 GHz

Slab rotation angles		$\theta_1 = 0°$	$\theta_1 = 45°$	$\theta_1 = 90°$
Simulated	Beam direction (˚)	6	21	43
	Realized gain (dBi)	11.58	12.64	11.61
	SLLs (dB)	-19.41	-20.18	-17.45
	Realized gain/Directivity (%)	43	61	86
	Dissipated power* (%)	27.5	12.8	6.9
Measured	Beam direction (˚)	6	21	42
	Realized gain (dBi)	11.17	12.47	11.57
	SLLs (dB)	-19	-18	-18

$^{*}P_{dissipated} = 1 - |S_{11}|^2 - |S_{21}|^2 - P_{radiated}$

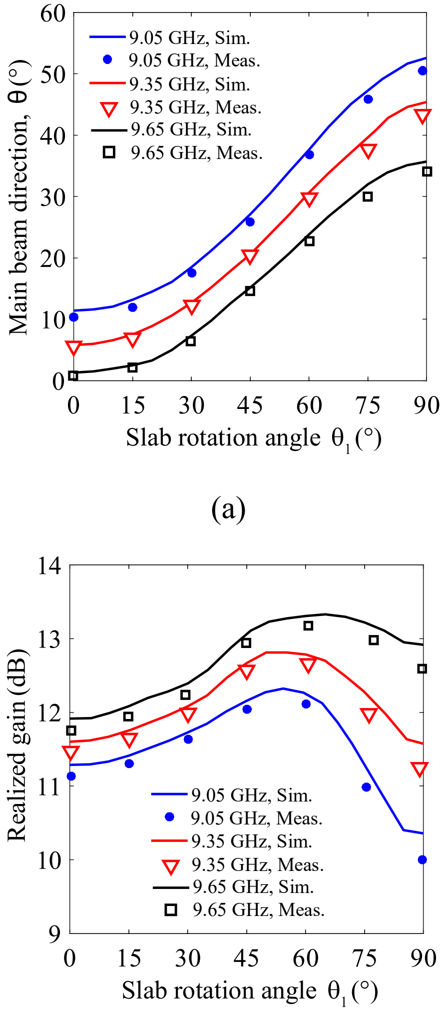

(a)

(b)

Figure 6.7: (a) Simulated and measured (a) main beam direction and (b) realized gain for various slab rotation angles of θ_1. The antenna was designed for a slab rotation of 45° and a frequency of 9.35 GHz.

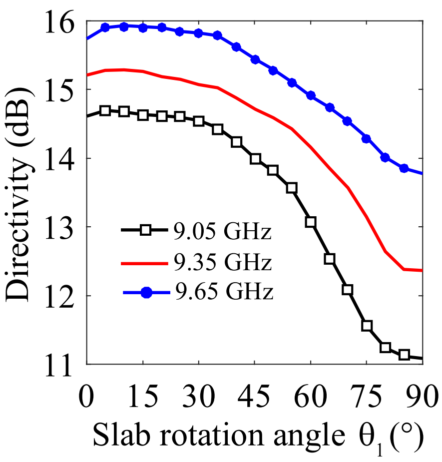

(a)

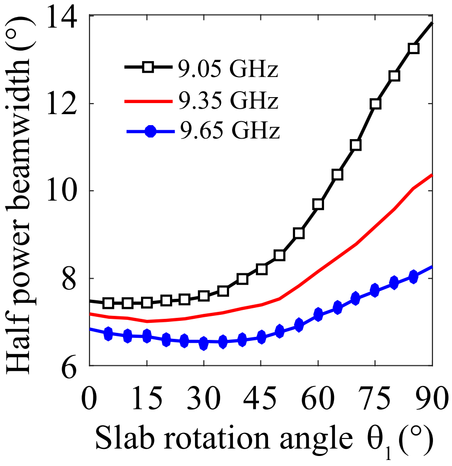

(b)

Figure 6.8: Simulated (a) directivity and (b) half power beamwidth for various rotation angle of θ_1. The frequencies correspond to the weather radar application.

Table 6.4 presents a comparison with other beam scanning antenna concepts based on waveguides [78], [102] and [110]. As in this work, refs. [78], [102] and [110] use mechanical modifications of the waveguide, but the achieved scanning range is much less. Ref. [102] has a similar scanning range but it is based on a frequency scanning principle and it requires a broad bandwidth (27%).

Table 6.4: Comparison with existing literature

	Ref. [78]	Ref. [102]	Ref. [110]	This work
Scanning range (º)	14	9	33	36
Frequency (GHz)	1.12	8-12	8-10.5	9.05-9.65
Number of slots	8	13	8	20
Gain (dBi)	not available	not available	-2 to 10	11.17 to 12.47
Sidelobe level (dB)	-10	-9	-10 to -22	-18
Scanning type	mechanical	mechanical	frequency	mechanical

6.5 Conclusion

A new beam scanning antenna based on a narrow wall slotted waveguide operating in X band has been presented. The measured antenna prototype has a scanning range of 36° at the design frequency and a 10 dB return loss bandwidth of 10%.The SLL remains at −18 dB over the scanning range and the realized gain changes by 1.3 dB.

The proposed antenna allows beam scanning without frequency variation and it only requires rotation of small lightweight part. It therefore has potential for higher scanning speed, which is currently required in weather radar antennas where the whole antenna needs to be rotated. In addition, this concept is a promising candidate for high power beam steering applications due to absence of nonlinear components. According to simulations, the air breakdown field is reached in the antenna when the input continuous power is 57 kilowatts in the worst case.

CHAPTER 7 GENERAL DISCUSSION

A comparison between different methods of beam scanning in rectangular waveguide designed of X-band radar frequencies is presented in this research work. The first method consists of rotating two dielectric slabs inside a broad wall slotted waveguide in order to achieve the element phase shifting in the slots excitations and consequently controlling the main beam direction. The antenna is a non-resonant 20-slot array with an element spacing of 0.58λ at the design frequency of 9.35 GHz. The simulated and measured design showed a 14° beam scanning from near broad side toward end-fire. The gain varied from 19.11 dB to 18.33 dB corresponded to the radiation efficiencies between 79.6% and 95%.

In the second method, we loaded the same waveguide with two I-shaped resonators (ISR) in order to improve the range of beam scanning to 28°. The gain variation was from 13.1 dB to 15.2 dB which was consistent with 45% to 82% radiation efficiency.

The third method was applying a rotating dielectric slab inside a 20-slot narrow wall waveguide with the element spacing of 0.44λ. A polarization filter was located near the slotted wall of the waveguide to reduce the cross-polarization, inspired form Chapter 5 was implemented. A 36° beam scanning was observed by rotating the dielectric slab with gain and radiation efficiency variation from 12.47 dB to 11.17 dB and from 86% to 43% respectively. The gain and efficiency decrement in method 2 and 3 was due to the presence of the ISR and relatively short length of the prototype respectively. In addition, there was no flare in method 2 and 3 to increase the gain.

The presented methods show the capability of electromechanical high power beam scanning in two different linear polarizations. The simulated and measured results are in good agreement. Table 7.1 presents a comparison of radiation performance between three methods.

The material and the dimensions of the dielectric slabs for all three methods have been chosen in order to propagate a single mode at the desired operational frequency. As it is briefly illustrated in Table 7.1, the dielectric material is $\varepsilon_r = 6.15$ and $\tan\delta = 0.0019$, $\varepsilon_r = 2.2$ and $\tan\delta = 0.0012$, $\varepsilon_r = 10.2$ and $\tan\delta = 0.0023$ for the first, the second and the third method respectively. Also, the dimensions of the dielectric slabs cross section are 5 mm and 2.5 mm for the first and the third methods and 5 mm and 1.5 mm for the second one. In addition, the elements spacing in all three methods is chosen in a way that, along with the excitation phase shifting of the elements, the antennas scan the main beam from near broad side toward end-fire direction. As a result, the aperture length of the third method is shorter than the others.

The dissipated power calculated for $\theta_1 = 45°$ and 9.35 GHz is shown in Table 7.1 for all three methods. The lowest dissipated power is seen in the first method that can possibly be the result of the desired resonant condition of the slots which leads to more radiated power. The second method has the highest dissipated power in the antenna because of the high ohmic loss due to the presence of the ISRs. The third method has less dissipated power than the second one because it does not use ISRs unlike the latter. However, due to its short aperture length, the dissipated power of the third method is more than the first one.

Table 7.1: Radiation performance of the three methods at 9.35 GHz

	Method I	Method II	Method III
Scanning range (º)	14	28	36
Gain variation (dBi)	19.11 to 18.33	13.2 to 15.2	11.17 to 12.47
Side lobe levels (dB)	−14	−15	−18
Efficiency variation (%)	79 to 95	45 to 82	43 to 86
Dissipated power* (%)	8.02	16	12.8
Scanning plane	H-plane	H-plane	E-plane
Dielectric material	$\varepsilon_r = 6.15$ $\tan\delta = 0.0019$	$\varepsilon_r = 2.2$ $\tan\delta = 0.0012$	$\varepsilon_r = 10.2$ $\tan\delta = 0.0023$
Element spacing	0.6λ	0.6λ	0.44λ
Aperture length	12λ	12λ	8.8λ
Flare	yes	no	no
Polarizer	no	no	yes

*for $\theta_1 = 45°$, $P_{dissipated} = 1 - |S_{11}|^2 - |S_{21}|^2 - P_{radiated}$

The first and the second methods are broad wall slotted waveguide and are presenting H-plane beam scanning while the third method is E-plane beam scanning in narrow wall slotted waveguide. Among these three methods, only the third one needs an X-pol filter because it has tilted slots cut on the narrow wall.

Although the narrow wall slotted waveguide (the third method) presents more beam scanning range, 8° and 22° more than the second and the first method respectively, the gain variation and the antenna efficiency variation are significantly less than the other antennas (see Table 7.1). The lower gain and efficiency are possibly due to the shortest aperture length of the third method. The gain variation in the second method is less than the first one because the ohmic loss is high due to presence of ISRs.

CHAPTER 8 CONCLUSIONS AND FUTURE WORKS

Three iterations of a waveguide-based beam scanning waveguide-fed slot array are presented in this work. Phase shifting is realized with electromechanical reconfigurable structures inserted in the waveguide. Element excitation phase shifting results in antenna beam steering. This antenna actuation mechanism is slow compared to electronically reconfigurable devices, nevertheless it can operate with high RF power levels and is less sensitive to temperature variations. Although the experimental evidence of the scanning capabilities of rotating a ridge in a metal waveguide slot array has already been explored by *Solbach al.* [78], to the knowledge of the author, an engineering approach has not been adopted to accomplish an antenna design achieving real specifications, so far.

An overview of the most generally-used slot arrays in classic waveguide technology has been performed in this project. Subsequently, in order to focus on the novelties – regarding the beam steering performance – derived from the employment of this approach, an analysis of these slot array waveguides with the rotating dielectric slabs has been done. Before the beginning of the design, a break into the synthesis approach has been done to remove the possible confusions that appear to the designer's mind. These confusions are possibly because of the validity of the classic design procedure when using a waveguide with rotating dielectric slabs.

A brief review of the main design has been accomplished to conclude that the triangular tapering design method, together with the same set of equations, is perfectly appropriate to achieve designs on the waveguide with the rotating dielectric slabs. Although other types of distribution such as Tylor and Chebyshev can also be applied to reduce the side lobe level, the triangular tapering method produced acceptably good results. This is the reason why we did not try other distribution types in this work. It should also be noted that since this is not possible to make a triangular tapering distribution design that works for all slabs rotation angles, the measured and the theoretically calculated side lobe levels are different. Therefore, trying to adjust the tapering to reduce the side lobe levels may not be necessary.

We were obliged to make shorter arrays due to some performance limitations because of the size of our measurement system and the fabrication facilities available in the laboratory. However, this is not a limit for the proposed design.

8.1.1 Dielectric covered slot

The complete pattern of a phased array is derived by multiplying the array factor by the element pattern [15]. The fine distinction in array multiplication is that as the array factor steers with the phase change, the element pattern remains unchanged and while the array is steered the peak of the total array pattern pursues the element pattern form. The unaffected element pattern has several effects on the total array. First, the peak of the main beam is decreased by the level of the element pattern at the desired angle. Secondly, the maximum of the antenna pattern and of the array factor are not in the same direction and as a result that the scan angle is a few degrees less than desired [15]. These are general trends in array scanning which yields the designer to improve the element pattern specifications [15].

The presence of a suitable dielectric substrate on the waveguide lowers the resonant conductance of the slot sets which can alter the characteristics of the individual slots and considerably affect the mutual coupling [112]. A very simple simulation using the method of [112] has been done by the dielectric cover of $\varepsilon_r = 2.2$ and a thickness of 0.254 mm. Figure 8.1 shows that as the dielectric covers the slot, the beam widens. This effect is promising in a way to improve the antenna concepts presented in this work.

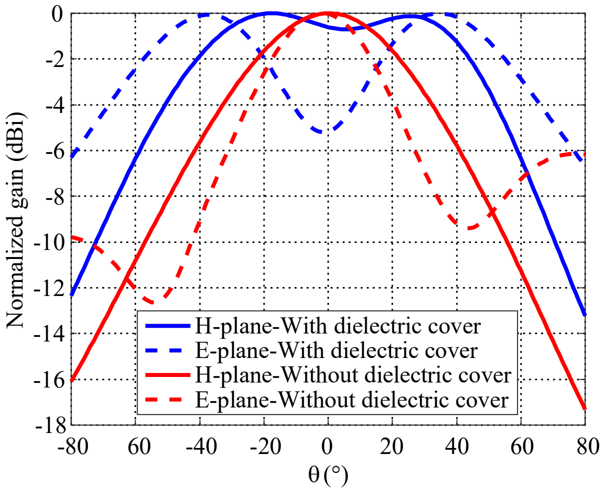

Figure 8.1: Effect of the dielectric covered slot on the element pattern.

8.1.2 1D Pencil beam scanning

A cylindrical parabolic reflector can be added in order to convert the fan beam of the slotted waveguide into a pencil beam. The cylindrical parabolic antenna consists of a cylindrical reflector with parabolic cross section and a line feed, which could be our slotted waveguide, along the focal line of the reflector (see Figure 7.2). A pencil beam can be scanned in one direction by creating the one-dimensional (1-D) phased array of waveguide antenna. Figures 8.3 and 8.4 show the simulation result.

The simulation characterisations of the cylindrical reflector are:

- 20-element array (see chapter 3)
- Triangular amplitude distribution (see chapter 3)
- Slots replaced by dipoles over a ground plane
- FEKO simulator: MoM for the array and PO for the reflector
- Non-optimized system however demonstrates good quality of focusing in the E plane by the reflector.

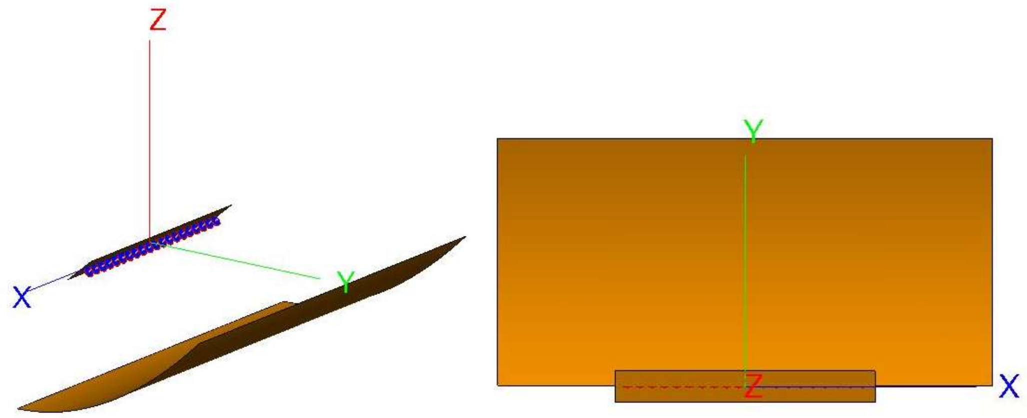

Figure 8.2: Simulation model of the array with cylindrical parabolic reflector.

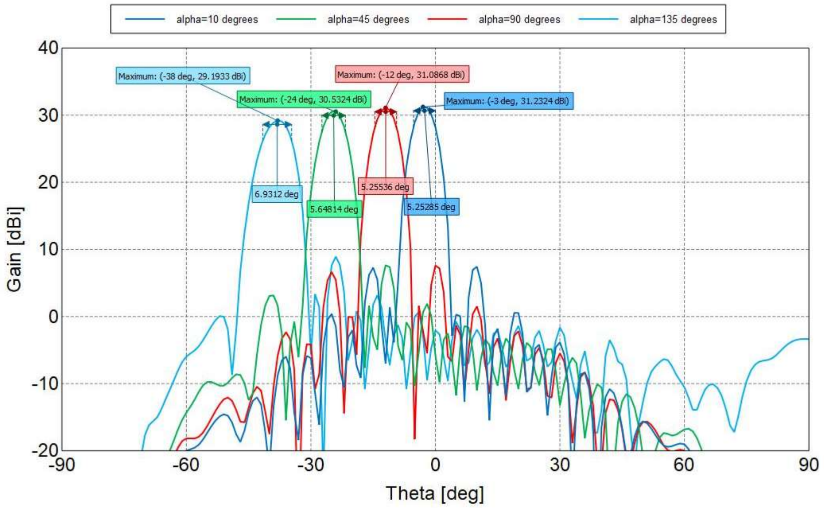

Figure 8.3: Simulated scanning performance of the array with cylindrical parabolic reflector at 9.35 GHz and $\phi = 0$.

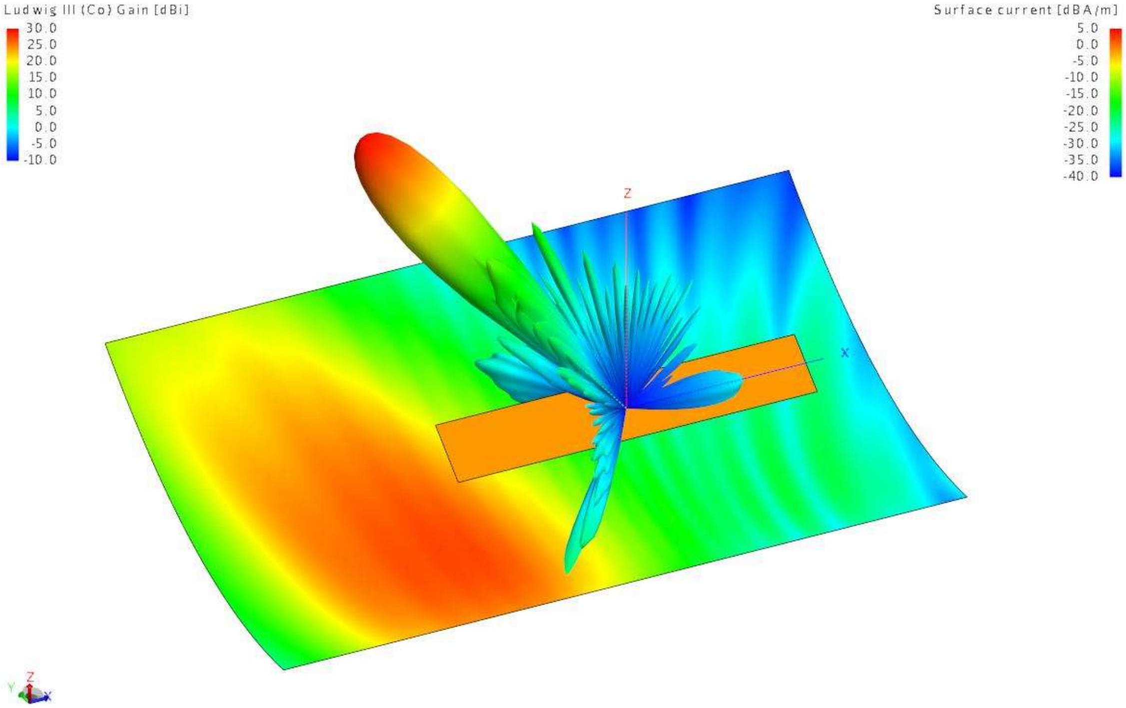

Figure 8.4: Simulated 3-D radiation pattern and current distribution on the reflector of the array with cylindrical parabolic reflector at 9.35 GHz. The beam is scanned at θ = 36°.

BIBLIOGRAPHY

[1] G. Caille, E. Vourch, M. J. Martin, J. R. Mosig, A. Martin Polegre, "Conformal array antenna for observation platforms in low earth orbit", *IEEE Antennas Propag. Mag.*, vol. 44, no. 3, pp. 103-104, Jun. 2002.

[2] L. A. Greda, A. Winterstein, A. Dreher A, "A satellite multiple-beam antenna for high-rate data relays", PIER, vol. 149, pp. 133–145, 2014.

[3] E. Re. "Antennas for Satellite Telecommunications Constellations: a key technology enabler," *39th ESA Antenna Workshop*, Netherlands, 2-4 October 2018.

[4] Canadian Weather Radar Network. Available at https://en.wikipedia.org/wiki/Canadian_weather_radar_network. Accessed November 2018.

[5] McGill JS Marshall Radar Observatory. Available at http://www.radar.mcgill.ca/facilities.html, accessed November 2018.

[6] M. Cooley and D.Davis, *Radar Handbook*, vol. Reflector antennas. New York : McGraw-Hill, 3rd ed., 2008.

[7] S.Q. Kidder, K.E. EIS, T.H. Vonder-Haar, "New GOES Imager System Products Suitable for Use on Field-Deployable Systems", *Battlespace Atmospheric and Cloud Impacts on Military Operations Conference Hanscom Air Force Base*, pp. 452-459, 1998.

[8] J. Sun and J. Wilson, "The assimilation of radar data for weather prediction," Meteorological Monographs, vol. 30, no. 52, pp. 175-175, 2003.

[9] K. Solbach and R. Schneider, "*Review of Antenna Technology for Millimeter wave Automotive Sensors*", EuMC1999, pp. 139-142, April 1999.

[10] J. Davis, "*Radar system for headway control of a vehicle*", Apr. 10 1990, US Patent 4,916,450. [Online]. Available: http://www.google.ca/patents/US4916450

[11] H. H. Meinel and J. Dickmann, "Automotive radar: From its origins to future directions", Microwave Journal, Vol. 56 pp. 24-40, September 2013.

[12] H.R. Ward, C.A. Fowler, H.I. Lipson, "GCA radars: Their history and state of development", *Proceedings of the IEEE*, vol. 62, no. 6, pp. 705-716, June 1974.

[13] C. E. Muehe, "New techniques applied to air-traffic control radars", *Proc. IEEE*, vol. 62, pp. 716-723, 1974.

[14] R. C. Hansen, Phased Array Antennas, New York, NY, USA, Wiley, 2009.

[15] W. Stutzman, L. Thiele, Antenna theory and design, Wiley, 3rd ED, 2012.

[16] J. D. Kraus and R. J. Marhefka, Antenna, 3rd ed. Beijing, China: Electronics Technology Press, 2011, pp. 69–89.

[17] Constantine A. Balanis, Antenna Theory, Analysis and Design, 3rd ed., John Wiley & Sons, 2005

[18] R.J. Mailloux, Phased Array Antenna Handbook, Artech House, Boston, 1994.

[19] E. Brookner, Practical Phased Array Antenna Systems, Artech House, Boston, 1991.

[20] Johnson, Richard C. Antenna Engineering Handbook, 3rd ed. McGraw-Hill, 1993.

[21] B. Muneer, Z. Qi, X. Shanjia, "A broadband tunable multilayer substrate integrated waveguide phase shifter", *IEEE Microw. Wireless Compon. Lett.*, vol. 25, no. 4, pp. 220-222, Apr. 2015.

[22] U. Shah et al., "Submillimeter-wave 3.3-bit RF MEMS phase shifter integrated in micro-machined waveguide", *IEEE Trans. THz Sci. Technol.*, vol. 6, no. 5, pp. 33-38, Sep 2016.

[23] M. Elkholy, S. Shakib, J. Dunworth, V. Aparin, K. Entesari, "Low-Loss Highly Linear Integrated Passive Phase Shifters for 5G Front Ends on Bulk CMOS", *IEEE Trans. Antennas Propag.*, vol. 66, no. 10, pp. 4563–4575, Oct. 2018.

[24] G. McDonald, C. Wilson, "High power ferrite phase shifters for phased array radars", *Active and Passive Components for Phased Array Systems, IEE Colloquium*, pp. 21-27, April 1992.

[25] R. K. Sorensen, M. F. Iskander, J. J. Lee, "Low-cost nonplanar microstrip-line ferrite phase shifter utilizing circular polarization", *IEEE Microw. Wireless Compon. Lett.* vol. 14, no. 1, pp. 25-27, Jan. 2004.

[26] Z. Zhao, X. Wang, K. Choi, A. T. Hunt, "Ferroelectric phase shifters at 20 and 30 GHz", *IEEE Trans. Microw. Theory Tech.*, vol. 55, no. 2, pp. 430-437, Feb. 2007.

[27] R. V. Garver, "Broad-band diode phase shifters", *IEEE Trans. Microw. Theory Techn.* vol. MTT-20, no. 5, pp. 314-323, May 1972.

[28] Y. Itoh, T. Murata, "An L-band SiGe HBT differential variable phase shifter with a combination of analog and digital phase control", *Microwave Conference, 2009. APMC 2009. Asia Pacific*, vol., no., pp.1589-1592, 7-10 Dec. 2009.

[29] National Severe Storms Laboratory, "Multi-function phased array radar (MPAR)", *NOAA National Severe Storms Laboratory,* Available: http://www.nssl.noaa.gov/tools/radar/mpar/, accessed November 2018.

[30] U. Kodak, G. M. Rebeiz, “Bi-directional flip-chip 28 GHz phased-array core-chip in 45nm CMOS SOI for high-efficiency high-linearity 5g systems”, *2017 IEEE Radio Frequency Integrated Circuits Symposium (RFIC)*, pp. 61-64, Jun. 2017.

[31] Y. Yusuf, X. Gong, “A low-cost patch antenna phased array with analog beam steering using mutual coupling and reactive loading”, *IEEE Antennas Wireless Propag. Lett.* vol. 7, pp. 81-84, 2008.

[32] M. Davis, “Leveraging commercial wireless communications industry advances to lower the cost of phased arrays”, *Microwave Symposium Digest (MTT), 2010 IEEE MTT-S International*, pp.680-683, 23-28 May 2010.

[33] Radartutorial.eu, assessed November 2018. Available at http://www.radartutorial.eu.htlm.

[34] G. Zhang, Q. Zhang, Y. Chen, T. Guo, C. Caloz, R. D. Murch, “Dispersive Feeding Network for Arbitrary Frequency Beam Scanning in Array Antennas”, *IEEE Trans. Antennas Propag.*, vol. 65, no. 6, pp. 3033–3040, June 2017.

[35] P. Antonik, M. C. Wicks, H. D. Griffiths, and C. J. Baker, “Frequency diverse array radars”, in *Proc. IEEE Conf. Radar*, p.3, Apr. 2006.

[36] S. Gupta, S. Abielmona, and C. Caloz, “Microwave analog real-time spectrum analyzer (RTSA) based on the spectral–spatial decomposition property of leaky-wave structures”, *IEEE Trans. Microw. Theory Techn.*, vol. 57, no. 12, pp. 2989–2999, Dec. 2009.

[37] S. Ver Hoeye, R. Camblor, C. Vázquez, M. Fernández, G. Hotopan, and F. Las Heras, “Terahertz frequency scanning 8 × 1 antenna array for imaging applications,” in *Proc. IEEE Int. Conf. Wireless Inf. Technol. Syst. (ICWITS)*, pp. 1–4, Nov. 2012.

[38] C. Vázquez, C. García, Y. Álvarez, S. Ver-Hoeye, and F. Las-Heras, “Near field characterization of an imaging system based on a frequency scanning antenna array,” *IEEE Trans. Antennas Propag.*, vol. 61, no. 5, pp. 2874–2879, May 2013.

[39] A. Ghasemi, J. J. Laurin, “Beam Steering Slotted Waveguide Antenna Using Rotating Dielectric Slabs for Meteorology Radar,” Submitted at *IEEE Trans. Antennas Propag.* 2017.

[40] F. Siaka, “Antenne à balayage de faisceau angulaire avec faible variation de la fréquence,” *PhD Thesis Ecole Polytechnique de Montreal*, 2015.

[41] S. S. Jaco du Preez, “Millimeter- Wave Antennas: Configurations and Applications,” springer, 2016.

[42] R. S. Elliott, Antenna Theory and Design, New York: Prentice-Hall, 1981.

[43] M. Takahashi, J. Takada, M. Ando, N. Goto, “A slot design for uniform aperture field distribution in single-layered radial line slot antennas,” *IEEE Trans. Antennas Propag.*, vol. 39, no. 7, pp. 954-959, Jul. 1991.

[44] W. Menzel, “A new traveling-wave antenna in microstrip,” *Arch. Elektron. Uebertrag. Tech.*, vol. 33, no. 4, pp. 137-140, Apr. 1979.

[45] A. A. Oliner, K. S. Lee, “The nature of the leakage from higher modes on microstrip line”, *IEEE MTT-S Int. Microw. Symp. Dig.*, pp. 57-60, Jun. 1986.

[46] C.-N. Hu, C.-K. C. Tzuang, “Analysis and design of large leaky-mode array employing the coupled-mode approach”, *IEEE Trans. Microw. Theory Tech.*, vol. 49, no. 4, pp. 629-636, Apr. 2001.

[47] K. C. Chen, C. K. C. Tzuang, Y. Qian, T. Itoh, “Leaky properties of microstrip above a perforated ground plane”, *IEEE MTT-S Int. Microw. Symp. Dig.*, pp. 69-72, 1999-Jun.

[48] C. Caloz, T. Itoh, A. Rennings, “CRLH metamaterial leaky-wave and resonant antennas”, *IEEE Antennas Propag. Mag.*, vol. 50, no. 5, pp. 25-49, Oct. 2007.

[49] S. Otto, A. Al-Bassam, A. Rennings, K. Solbach, C. Caloz, “Transversal asymmetry in periodic leaky-wave antennas for Bloch impedance and radiation efficiency equalization through broadside”, *IEEE Trans. Antennas Propag.*, vol. 62, no. 10, pp. 5037-5054, Oct. 2014.

[50] A. A. Oliner and D. R. Jackson, “Leaky-Wave Antennas,” Ch. 11 in Antenna Engineering Handbook, 4th Ed., J. L. Volakis (Ed.), McGraw-Hill, New York, 2007.

[51] Q. Yang, X. Zhao, Y. Zhang, “Composite right/left-handed ridge substrate integrated waveguide slot array antennas,” *IEEE Trans. Antennas Propag.*, vol. 62, no. 4, pp. 2311-2316, 2014.

[52] F. Frezza, “Introduction to Traveling-Wave antennas,” pp. 1-10, 2006.

[53] A. Lai, T. Itoh, and C. Caloz, “Composite right/left handed transmission line metamaterials”, *IEEE Microw. Mag.,* vol.5, no.3, pp.34-50, Sep. 2010.

[54] I. A. Eshrah, A. A. Kishk, A. B. Yakolev, and A. W. Glisson, “Rectangular waveguide with dielectric-filled corrugations supporting backward waves”, *IEEE Trans.Microwave Theory Tech.,* , vol.53, no.11, pp. 3298- 3304, Nov. 2005.

[55] S. Otto, Z. Chen, A. Al-Bassam, A. Rennings, K. Solbach, C. Caloz, “Circular polarization of periodic leaky-wave antennas with axial asymmetry: Theoretical proof and experimental demonstration”, *IEEE Trans. Antennas Propag.*, vol. 62, no. 4, pp. 1817-1829, Apr. 2014.

[56] A. Mirkamali, F. Siaka, J.-J. Laurin, and R. Deban, “Fast and low-cost beam steering using an agile mechanical feed system for exciting circular arrays,” *IET Microwaves, Antennas & Propagation,* vol. 10, no. 4, pp. 378–384, Mar. 2016.

[57] G. Zhang, R. J. Doviak, D. S. Zrnic, J. Crain, D. Staiman, Y. Al-Rashid, “Phase array radar polarimetry for weather sensing: A theoretical formulation for bias corrections”, *IEEE Trans. Geosci. Remote Sens.*, vol. 47, no. 11, pp. 3679-3689, Nov. 2009.

[58] S. Karimkashi, G. Zhang, “An optimal design of a cylindrical polarimetric phased array radar for weather sensing”, *Radio Sci.*, vol. 47, 2011.

[59] M. E. Weber, J. Y. N. Cho, J. S. Herd, J. M. Flavin, W. E. Benner, G. S. Torok, “The next-generation multi-mission U.S. surveillance radar network”, *Bull. Amer. Meteorol. Soc.*, vol. 88, no. 11, pp. 1739-1751, Nov. 2007.

[60] M. Sanchez-Barbetty, “Low cost electronically steered phase arrays for weather applications”, PhD thesis, University of Massachusetts, Amherst, 2011.

[61] P. Ioannides, C. A. Balanis, “Uniform circular and rectangular arrays for adaptive beamforming applications”, *IEEE Antennas Wireless Propagat. Lett.*, vol. 4, pp. 351-354, 2005.

[62] D. Piazza, J. Kountouriotis, M. D'Amico, K. Dandekar, “A technique for antenna configuration selection for reconfigurable circular patch arrays”, *IEEE Trans. Wireless Commun.*, vol. 8, no. 3, pp. 1456-1467, Mar. 2009.

[63] L. Jossefson, P. Persson, “Conformal array antenna theory and design”, IEEE Press, Wiley-Interscience, Hoboken, N. J.,2006.

[64] H. Legay, S. Tubau, E. Girard, J.-Ph. Fraysse, R. Sauleau, M. Ettorre, and N. J. G. Fonseca, “Multiple beam antenna based on a parallel plate waveguide continuous delay lens beamformer,” *International Symposium on Antennas and Propagation (ISAP)*, Okinawa, Japan, October 24-28, 2016.

[65] F. Doucet, N. J. G. Fonseca, E. Girard, H. Legay and R. Sauleau, “Analysis and design of a continuous parallel plate waveguide multiple beam lens antenna at Ku-band,” *2017 11th European Conference on Antennas and Propagation (EUCAP)*, Paris, 2017, pp. 3631-3635.

[66] M. Ettorre, R. Sauleau, and L. Le Coq, "Multi-beam multi-layer leaky-wave SIW pillbox antenna for millimeter-wave applications," *IEEE Trans. Antennas Propag*., vol. 59, no. 4, pp. 1093-1100, Apr. 2011.

[67] W. Rotman, "Wide-angle scanning with microwave double-layer pillboxes", *IRE Trans. Antennas Propag*., vol. 6, no. 1, pp. 96-105, Jan. 1958.

[68] C. Hua, X. Wu, N. Yang, and W. Wu, "Air-filled parallel plate cylindrical modified Luneberg lens antenna for multiple-beam scanning at millimeter-wave frequencies", *IEEE Trans. Antennas Propag*., vol. 61, no. 1, pp. 436-442, Jan. 2013.

[69] R. C. Rudduck and C. H. Walter, "Luneberg lens for space communications," *IRE Trans. Space Electronics and Telemetry*, vol. SET-8, pp. 31-37, 1962.

[70] R. S. Elliot, Antenna Theory and Design, Prentice Hall, 1981.

[71] S. H. Dar, Z. Ahmed, M. B. Ihsan, "Characterization of waveguide slots using full wave EM analysis software HFSS", *2008 IEEE International Multitopic Conference*, pp. 85-90, 2008.

[72] W. Ren, B. Gao, "Full wave Analysis of Broad Wall Slot's Characteristics in Rectangular Waveguides", *IEEE Trans. Antenna Propagat.*, vol. 52, no. 9, pp. 2436-2444, Sept. 2004.

[73] G. M. Shaw. S. R. Rengarjan, R. S. Elliot, "Analysis of mutual coupling in planar slot array antennas", *IEEE Antenna Propagat. Sym.,* Chicago, IL, July 1992.

[74] S. H. Dar, A. Zubair, M. Ihsan, "Design of a low side lobe slotted waveguide planar array", *IBCAST, Wireless Comm. and Radars*, 2007.

[75] R. S. Elliot, "An improved design procedure for small slot arrays", *IEEE Trans. Antenna Propagat*. Vol. 26, pp. 214-219, Mar. 1978.

[76] R. S. Elliot, and L. A. Kurtz, "The design of slot array antennas", *IEEE Trans, Antenna Propagat*., Vol. 31, pp. 48-53, Jan. 1983.

[77] R. S. Elliot, W. R. O`Loughlin, "The design of slot arrays including internal mutual coupling", *IEEE Trans. Antenna Propagat.* Vol. 34. Pp. 1149-1154. Sept. 1986.

[78] K. Solbach and D. Demirel, "Electro-mechanical beam scanning antenna using rotating ridge inside waveguide slot array," in *2007 2nd International ITG Conf. on Antennas,* Munich, Germany, Mar. 2007.

[79] Sanchez-Barbetty, Mauricio, "Low Cost Electronically Steered Phase Arrays for Weather Applications," *Open Access Dissertations.* Paper 343. 2011.

[80] A. Ghasemi, J. J. Laurin, “Beam Steering in Narrow Wall Slotted Ridge Waveguide Antenna Using a Rotating Dielectric Slab,” *IEEE Antennas Wireless Propag. Lett.* Aug. 2018.

[81] V. Manasson, L. Sadovnik, and R. Mino, “MMW scanning antenna,” *IEEE AES Syst. Mag.,* pp. 29–33, Oct. 1996.

[82] R. Schneider and W. J., “High resolution radar for automobile application,” *Advances in Radio Science,* vol. 1, no. 6, pp. 105–111, May. 2003.

[83] K. Tekkouk, J. Hirokawa, R. Sauleau, M. Ando, “Wideband and Large Coverage Continuous Beam Steering Antenna in the 60-GHz Band,” *IEEE Trans. Antennas Propag.* vol. 65, no. 9, pp. 4418–4426, Sept. 2017.

[84] X. Lu, S. Gu, X. Wang, H. Liu, W. Lu, “Beam-Scanning Continuous Transverse Stub Antenna Fed by a Ridged Waveguide Slot Array,” *IEEE Antennas Wireless Propag. Lett.,* vol. 16, pp. 1675–1678, Feb. 2017.

[85] N. K. Host, C.-C. Chen, J. L. Volakis, and F. A. Miranda, “Low cost beam-steering approach for a series-fed array,” in *2013 IEEE Int. Symp. on Phased Array Syst. and Technology*, pp. 293–300, Waltham, MA, USA, Oct. 2013.

[86] X. Fang, Y. Huang, and G. Wen, “A low-cost mechanical beam scanning waveguide slot antenna array,” IEEE AP-S Int. Symp., July 2017.

[87] N. K. Host, C.-C. Chen, J. L. Volakis, and F. A. Miranda, “Ku-band traveling wave slot array scanned via positioning a dielectric plunger,” *IEEE Trans. Antennas Propag.,* vol. 63, no. 12, pp. 5475–5483, Dec. 2015.

[88] H. Ward, C. Fowler, and H. Lipson, “GCA radars: Their history and state of development,” *Proc. IEEE,* vol. 62, no. 6, pp. 705–716, Jun. 1974.

[89] T. Sabapathy, M. F. B. Jamlos, R. B. Ahmad, M. Jusoh, M. I. Jais, and M. R. Kamarudin, “Electronically reconfigurable beam steering antenna using embedded RF PIN based parasitic arrays (ERPPA),” *Prog. In Electromag. Res.,* vol. 140, pp. 241–261, 2013.

[90] C. Ding, Y. J. Guo, P. Y. Qin, T. S. Bird, Y. T. Yang, “A defected microstrip structure (DMS) based phase shifter and its application in beamforming antennas”, *IEEE Trans. Antennas Propag.,* vol. 62, no. 2, pp. 641-651, Feb. 2014.

[91] J. R. De Luis, F. De Flaviis, “A reconfigurable dual frequency switched beam antenna array and phase shifter using PIN diodes”, in 2016 *IEEE Int. Symp. on Antennas and Propagat. (APSURSI)*, Charleston, SC, USA, June 2009.

[92] E. Ojefors, S. Cheng, K. From, I. Skarin, P. Hallbjorner, and A. Rydberg, “Electrically steerable single-layer microstrip traveling wave antenna with varactor diode based phase shifters,” *IEEE Trans. Antennas Propag.,* vol. 55, no. 9, pp. 2451–2460, Sep. 2007.

[93] L. Petit, L. Dussopt, and J.-M. Laheurte, “MEMS-switched parasitic-antenna array for radiation pattern diversity,” *IEEE Trans. Antennas Propag.*, vol. 54, no. 9, pp. 2624–2631, Sep 2006.

[94] N. Yang, C. Caloz, and K. Wu, “Full-space scanning periodic phase-reversal leaky-wave antenna,”*IEEE Trans. Microw. Theory Tech.,* vol. 58, pp. 2619-2632, Oct. 2010.

[95] A. Ghasemi, J. J. Laurin, “X-band waveguide phase shifter using rotating dielectric slab,” in 2016 *IEEE Int. Symp. on Antennas and Propagat. (APSURSI)*, Fajardo, Puerto-Rico, June 2016.

[96] M. Navarro-Tapia, J. Esteban, C. Camacho-Penalosa, “On the Actual Possibilities of Applying the Composite Right/Left-Handed Waveguide Technology to Slot Array Antennas,” *IEEE Trans. Antennas Propag.* vol. 60, no. 5, pp. 2183–2193, March 2012.

[97] R. E. Collin, *Antennas and Radiowave Propagation*, New York, NY, USA: McGraw-Hill, 1985.

[98] K. Sakakibara, J. Hirokawa, M. Ando, and N. Goto, “Periodic boundary conditions for evaluation of external mutual coupling in a slotted waveguide array,” *IEICE Trans. Commun.,* vol. E79-B, no. 8, pp. 1156-1164, Aug. 1996.

[99] A. Ghasemi, J. J. Laurin, “I-Shaped Resonator (ISR) Phase Shifter for Beam Steering Waveguide Antennas,” *Proc. 12th Eur. Conf. on Antennas and Propagation (EUCAP)*, 9-13 April 2016.

[100] E.C. Jordan and K.G. Balmain, Electromagnetic Waves and Radiating Systems, 2nd Ed., Prentice-Hall, 1968.

[101] A. Dadgarpour, B. Zarghooni, B. S. Virdee, T. A. Denidni, “Beam tilting antenna using integrated metamaterial loading,” *IEEE Trans. Antennas Propag.*, vol. 62, no. 5, pp. 2874-2879, May 2014.

[102] B.-J. Che, T. Jin, D. Erni, F. Y. Meng, Y.-L. Lyu, Q. Wu, “Electrically controllable composite right/left-handed leaky-wave antenna using liquid crystals in PCB technology,” *IEEE Trans. Compon. Packag. Manuf. Technol.*, vol. 7, no. 8, pp. 1331-1342, Aug. 2017.

[103] D. J. Kim, J.-H. Lee, "Beam scanning leaky-wave slot antenna using balanced CRLH waveguide operating above the cutoff frequency," *IEEE Trans. Antennas Propag.*, vol. 61, no. 5, pp. 2432-2440, May 2013.

[104] F. Siaka, J.-J. Laurin, and R. Deban, "New broad angle frequency scanning antenna with narrow bandwidth based on a CRLH structure," *IET Microw. Antennas Propag.* vol. 11, Iss. 11, pp. 1644–1650, Jun. 2017.

[105] P. Chen, W. Hong, Z. Kuai, J. Xu, "A substrate integrated waveguide circularly polarized slot radiator and its linear array", *IEEE Antennas Wireless Propag. Lett.*, vol. 8, pp. 120-123, 2009.

[106] A.R. Mallahzadeh and S. Mohammad ali nezhad, "An ultralow crosspolarization slotted waveguide chebyshev array antenna", *Proc. 5th Eur. Conf. Antenna Propag.*, pp. 1953-1956, Rome, April 2011.

[107] A. R. Mallahzadeh, S. Mohammad Ali Nezhad, "Cross-polarization and size reduction of slotted waveguide array antenna by angled ridges", *Proc. 6th Eur. Conf. Antenna Propag.*, pp. 1-5, Prague, Czech Republic, March 2012.

[108] D. Dogan, O. A. Civi, "Edge wall slotted waveguide antenna with low cross polarization", *Proc. IEEE Antennas Propag. Soc. Symp.*, pp. 1-4, Toronto, ON, Canada, Jul. 2010.

[109] J. Herranz-Herruzo, A. Valero-Nogueira, S. Martinez-Giner, A. Vila Jimenez, "Untilted narrow-wall slots excited by parasitic dipoles in groove-gap waveguide technology", *IEEE Transactions on Antennas and Propagation*, vol. 63, no. 11, pp. 4759-4765, Nov. 2015.

[110] C. C. Courtney, D. E. Voss, and T. McVeety, "Antenna beam steering concepts for high power applications," *Sensor Simul. Note*, vol. 491, pp. 1–13, Jan. 2004.

[111] A. Ghasemi, J. J. Laurin, "Cross-Polarization Reduction of a Narrow Wall Slotted Waveguide Array for Ku-Band," Accepted in 2018 *IEEE Int. Symp. on Antennas and Propagat. (APSURSI)*, Boston, Massachusetts, July 2018.

[112] B. Katehi, "Dielectric-covered waveguide longitudinal slots with finite wall thickness," *IEEE Trans. Antennas Propag.,* Vol. 38. No. 7. July 1990.

APPENDIX A – SINGLE ROTATING DIELECTRIC SLAB INSIDE THE SLOTTED BROADWALL WAVEGUIDE

In order to assess the effect of the single dielectric slab in the waveguide we have simulated an array of 10 slots applying the triangular amplitude distribution. The configuration is shown in Figure 3.1a. The normalized radiation pattern of a 10-slotted waveguide array with a single slab (with the parameters mentioned in Chapter 3) in three different rotation angle is shown below.

Figure A.1 shows the normalized radiation pattern of the array. The unavoidable grating lobe of the radiation pattern for the oblique position of the slab ($\theta_1 = 45°$) is regarded to the asymmetric field distribution inside the waveguide.

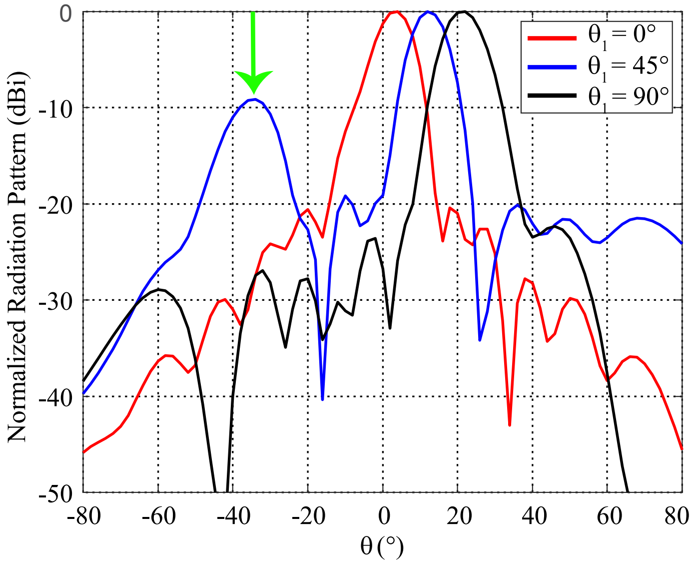

Figure A.1: Radiation pattern of the single slab inside the waveguide in three different rotation angles (H-plane at 9.35 GHz).

APPENDIX B – CONDUCTANCE CALCULATION OF A 20-ELEMENT NON-RESONANT ARRAY

The amplitude distribution over a 20-element array is chosen as a triangular distribution superimposed on a constant lower level:

$$a_1 = a_{20} = 1 + 2$$

$$a_2 = a_{19} = 2 + 2$$

$$a_3 = a_{18} = 3 + 2$$

$$a_4 = a_{17} = 4 + 2$$

$$a_5 = a_{16} = 5 + 2$$

$$a_6 = a_{15} = 6 + 2$$

$$a_7 = a_{14} = 7 + 2$$

$$a_8 = a_{13} = 8 + 2$$

$$a_9 = a_{12} = 9 + 2$$

$$a_{10} = a_{11} = 10 + 2$$

If the relative excitation level of the *n*th slot is a_n, the power P_n radiated by this slot will be proportional to a_n^2 . Thus when we specify the required amplitude distribution a_n to yield the desired beamwidth and side-lobe level we will know the P_n within a constant of proportionality.

Let *r* be the fraction of the incident power to be dissipated in the match load (Figure B.1) and we let $r = 0.15$. So we have

$$r + \sum_{n=1}^{20} P_n = 1$$

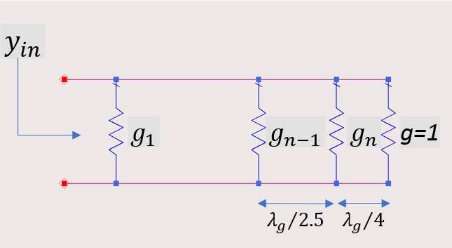

Figure B.1: Equivalent circuit model of the non-resonant array

We must normalize the values given above such that $2k(9+16+25+36+49+64+81+100+121+144)=1-r=0.85$ which give $k=6.5891\times10^{-4}$. The required P_n are found to be

$$P_1=P_{20}=9k=0.0059$$

$$P_2=P_{19}=16k=0.0105$$

$$P_3=P_{18}=25k=0.0165$$

$$P_4=P_{17}=36k=0.0237$$

$$P_5=P_{16}=49k=0.0323$$

$$P_6=P_{15}=64k=0.0422$$

$$P_7=P_{14}=81k=0.0534$$

$$P_8=P_{13}=100k=0.0659$$

$$P_9=P_{12}=121k=0.0797$$

$$P_{10}=P_{11}=144k=0.0659$$

By using the equation $g_n=\frac{P_n}{r+\sum_{i=n}^{N}P_i}=\frac{P_n}{1-\sum_{i=1}^{n-1}P_i}$ (4.176 of [97]) we find that the g_n are

$g_1=0.006$ $g_2=0.011$ $g_3=0.017$ $g_4=0.025$ $g_5=0.034$

$g_6=0.046$ $g_7=0.061$ $g_8=0.081$ $g_9=0.106$ $g_{10}=0.142$

$g_{11}=0.165$ $g_{12}=0.166$ $g_{13}=0.165$ $g_{14}=0.160$ $g_{15}=0.150$

$g_{16}=0.135$ $g_{17}=0.115$ $g_{18}=0.090$ $g_{19}=0.063$ $g_{20}=0.038$

For the non-resonant array a simplified design procedure may be used, provided the array consists of many slots (20 in this work) and is design for a beam angle not along normal to the array. In this case each slot radiates very little of the total power and hence represents a small discontinuity in the waveguide and produces only a small reflection of the incident wave. Furthermore, the slots are not spaced by $\lambda_g/2$ so the reflections from the different slots do not add up in phase and the total reflection coefficient at the input to the array will also be small.

APPENDIX C – SCANNING PERFORMANCE OF THE PROPOSED ANTENNAS

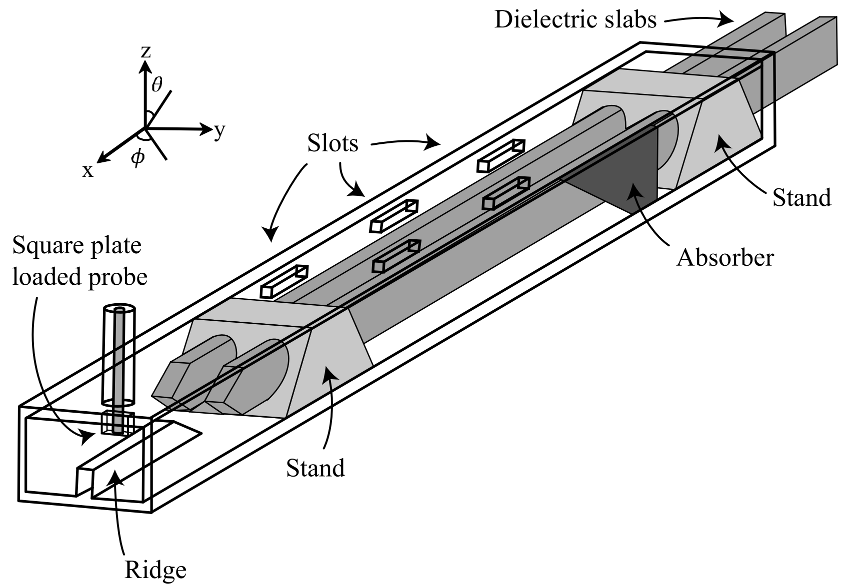

Figure C.1: Simulated model of broad wall slotted waveguide with rotating dielectric slabs.

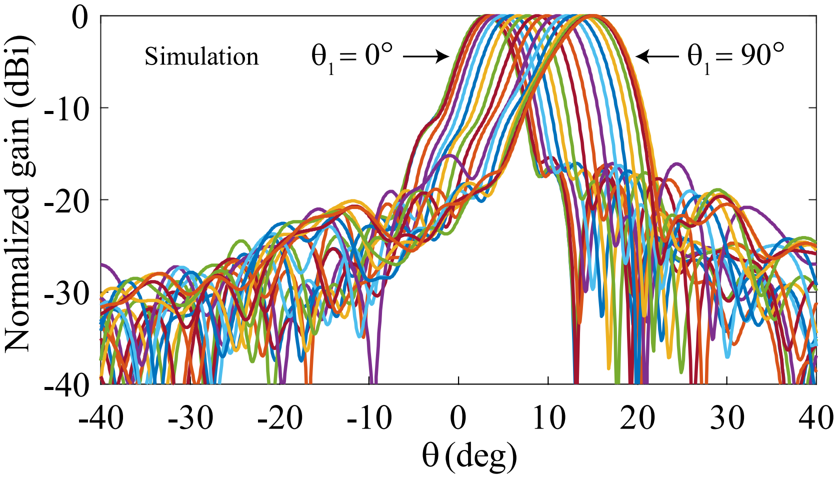

Figure C.2: H-plane ($\phi = 0$ at 9.35 GHz) normalized patterns of the broad wall slotted antenna, simulated in different rotating angle θ_1. Scanning range is 14°.

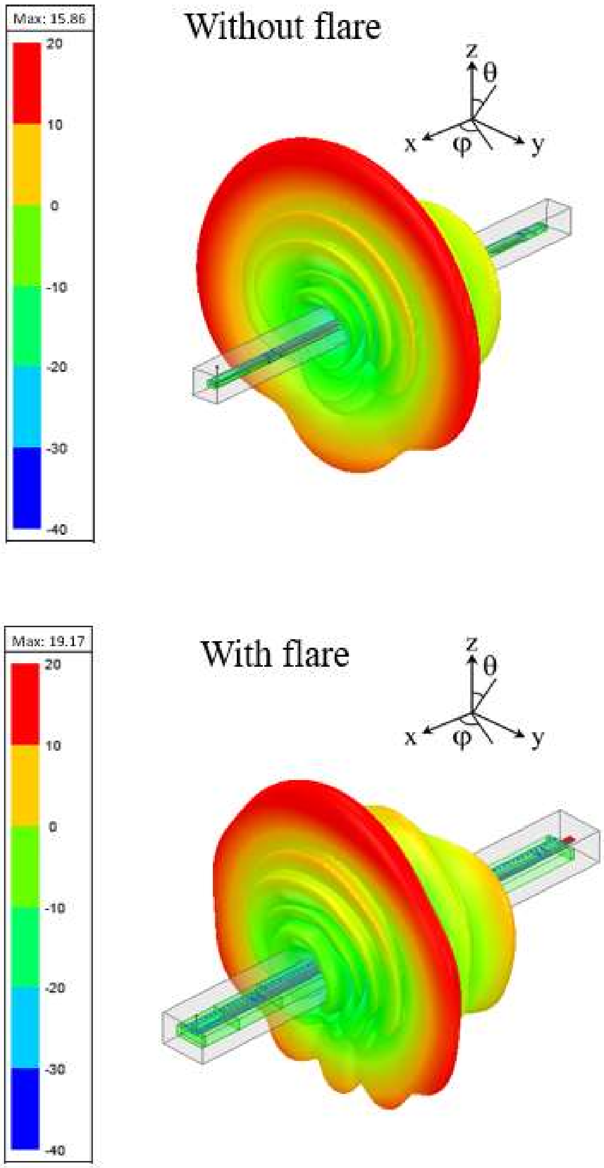

Figure C.3: 3D radiation patterns at 9.35 GHz of the broad wall slotted antenna (Chapter 3), with and without flare. The fan-beam deformed with the flare.

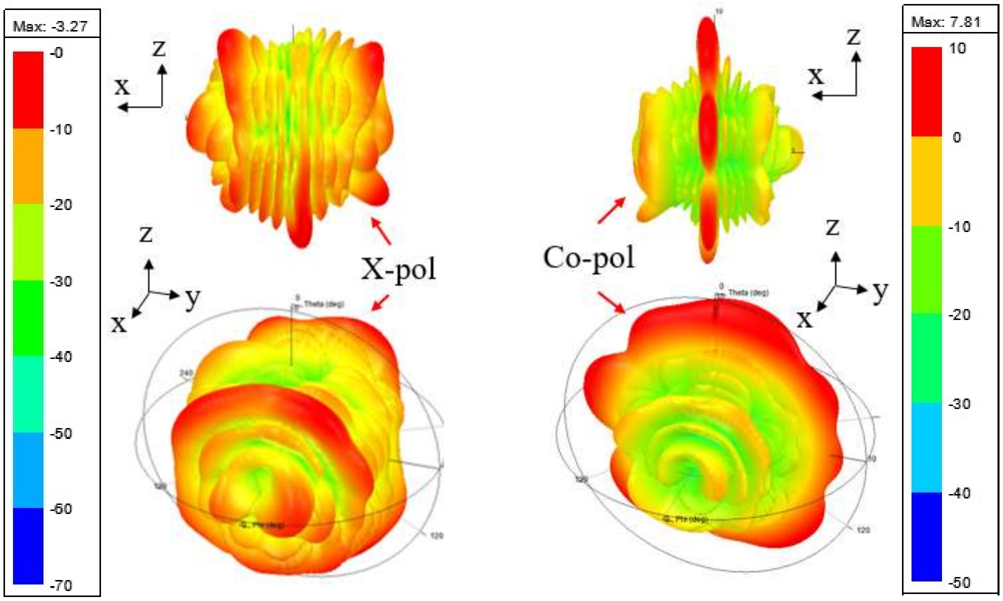

Figure C.4: 3D radiation patterns of the narrow wall slotted antenna at 14 GHz (Chapter 5). The antenna is without X-pol filter.

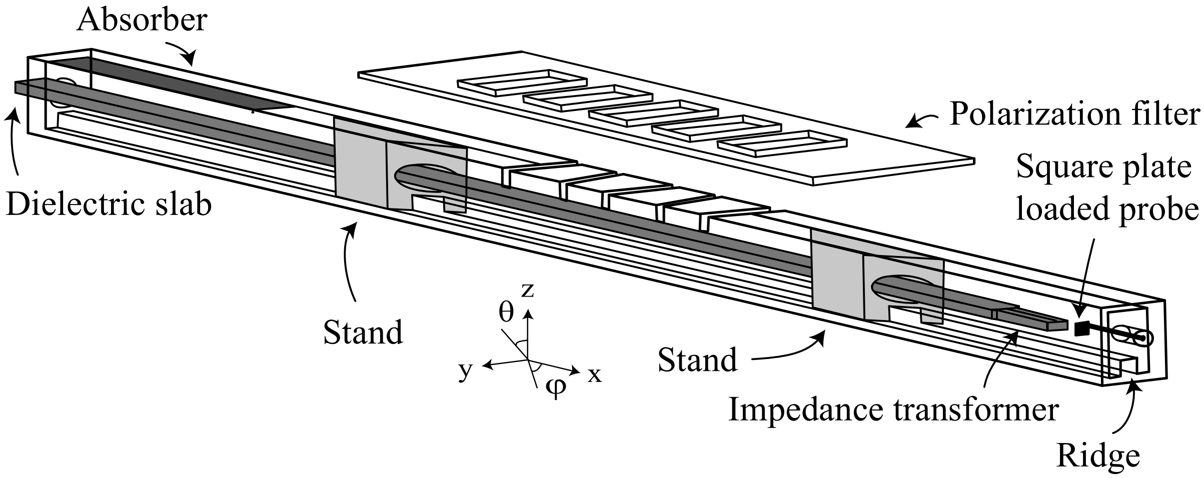

Figure C.5: Simulated model of narrow wall slotted ridge waveguide with rotating dielectric slab.

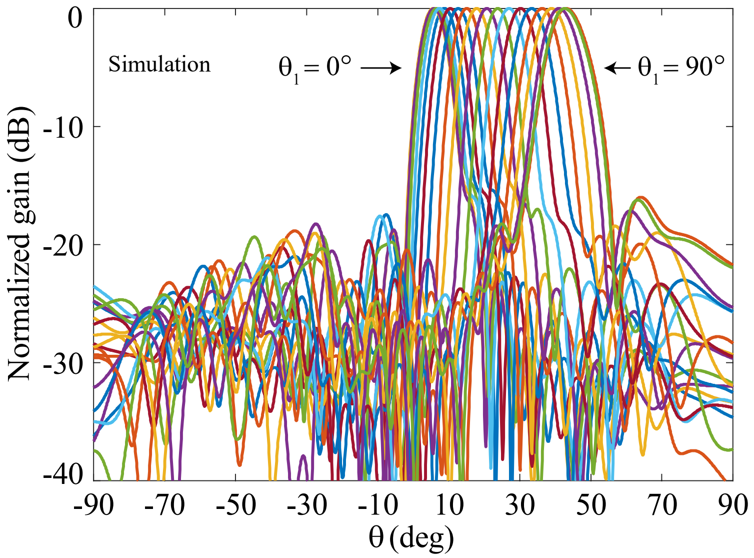

Figure C.6: E-plane ($\phi = 0$ at 9.35 GHz) normalized patterns of the narrow wall slotted waveguide, simulated in different rotating angle θ_1. Scanning range is 36°.

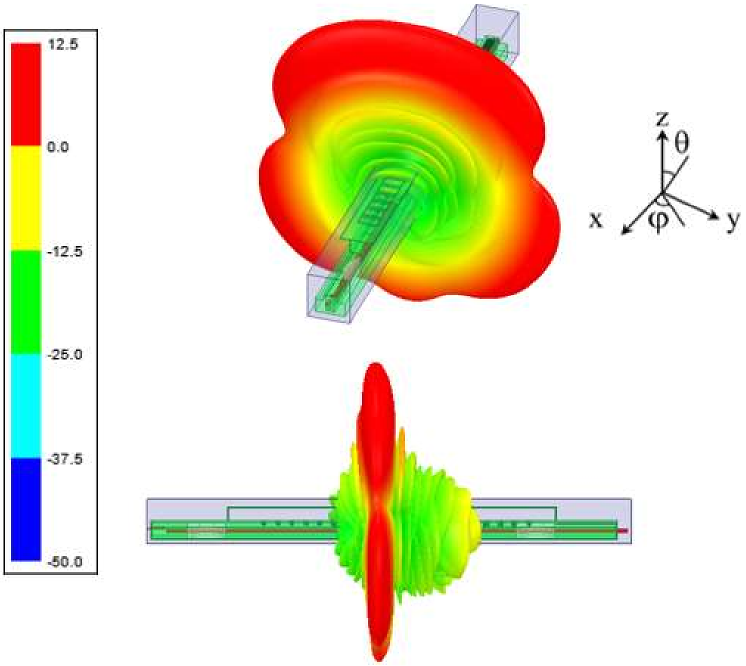

(a)

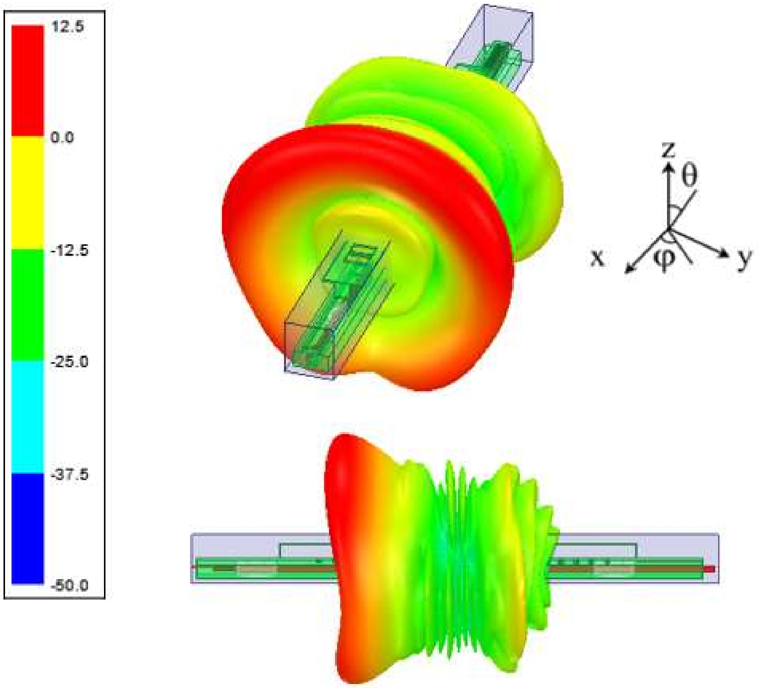

(b)

Figure C.7: 3D radiation patterns of the narrow wall slotted waveguide at 9.35 GHz (Chapter 6). The beam is steered at θ = 6° and θ = 42° for horizontal (a) and vertical (b) position of the dielectric slab respectively.